Assessing and Improving the Resilience of Highway and Railway Tunnels to Fire and Blast

FINAL PROJECT REPORT

By
Spencer Quiel
Email: seq213@lehigh.edu
Lehigh University

Clay Naito, Kyle Root, Qi Guo, Fengtao Bai, Aerik Carlton, Ziyan Ouyang

Lehigh University

Sponsorship
UTC-UTI
U.S. Department of Transportation
Lehigh University Cost Share Support

For

University Transportation Center for
Underground Transportation Infrastructure
(UTC-UTI)

July 2020

Disclaimer

The contents of this report reflect the views of the authors, who are responsible for the facts and the accuracy of the information presented herein. This document is disseminated in the interest of information exchange. The report is funded, partially or entirely, by a grant from the U.S. Department of Transportation's University Transportation Centers Program. However, the U.S. Government assumes no liability for the contents or use thereof.

1. Report No.	2. Government Accession No.	3. Recipient's Catalog No.

4. Title and Subtitle:
Assessing and Improving the Resilience of Highway and Railway Tunnels to Blast and Fire

5. Report Date
June 2020

6. Performing Organization Code

7. Author(s):
Spencer Quiel https://orcid.org/0000-0002-1316-7059, Clay Naito https://orcid.org/0000-0003-3835-8131, Kyle Root, Qi Guo https://orcid.org/0000-0003-2713-9478, Fengtao Bai https://orcid.org/0000-0003-1453-3417, Aerik Carlton https://orcid.org/0000-0002-7806-6099, Ziyan Ouyang https://orcid.org/0000-0003-0629-687X

8. Performing Organization Report No.

9. Performing Organization Name and Address
University Transportation Center for Underground Transportation Infrastructure (UTC-UTI)
Tier 1 University Transportation Center
Colorado School of Mines
Coolbaugh 308, 1012 14th St., Golden, CO 80401

10. Work Unit No. (TRAIS)

11. Contract or Grant No.

12. Sponsoring Agency Name and Address
United States of America
Department of Transportation
Research and Innovative Technology Administration

13. Type of Report and Period Covered
Final Report (Sept. 2016 to Oct. 2018)

14. Sponsoring Agency Code

15. Supplementary Notes
Report also available at: https://zenodo.org/communities/utc-uti

16. Abstract:
Tunnels are a critical component of our transportation infrastructure, and unexpected damage to a tunnel can significantly and adversely impact the functionality of a transportation network. Tunnels are susceptible to severe fire-induced heat flux due to the constant presence of vehicular traffic combined with the likelihood of accidents and subsequent combustion. They are also vulnerable to potential threats of intentional and accidental blast that can lead to local damage (spalling and breach) and progressive collapse. This report outlines approaches for assessing fire-induced thermal demands and blast-induced damage to the concrete tunnel liner. First, a rapid assessment approach is developed to evaluate thermal demands using models that are calibrated using computationally intensive numerical assessment, experimental data, and semi-empirical relationships. These fast-running approaches are useful for calculating appropriate design limit states and to better understand risk potential in a multitude of underground environments. Utilizing Rhino and Grasshopper, the discretized solid flame model is adapted to account for confinement within tunnel structures and development of a convective zone under the tunnel ceiling. The confined discretized solid flame model (CDSF) accurately captures the spatial distribution of heat flux in circular tunnels as compared to experimentally-validated, high fidelity numerical solutions. Potential for cracking, spalling, breach, and other adverse structural consequences can be evaluated based on contour maps of total heat flux over the tunnel liner. Second, an approach is presented to predict and map the damage to the reinforced concrete liner of a roadway tunnel for various explosive threat sizes and tunnel geometries. The proposed fast-running approach is an alternative to either high-fidelity computational models that require massive computational effort or simplified design expressions that cannot accurately capture spatial distributions of damage. A literature review of existing evaluation methods is conducted, and potential blast event scenarios are examined with varying charge position and size. Rectangular, horseshoe, and circular tunnel geometries, each with the same traffic throughput, are evaluated. The proposed approach shows good agreement with high-fidelity numerical models analyzed in LS-DYNA and is then used to examine the relationship between increasing blast hazard intensity and the extent of spall and breach damage. Inflection points in this relationship can be used to identify hazard levels at which a progressive collapse evaluation would be warranted.

17. Key Words:
Concrete; tunnel; fire; explosion; blast; CFD analysis; progressive collapse; breach; spalling

18. Distribution Statement
No restrictions.

19. Security Classification (of this report)	20. Security Classification (of this page)	21. No of Pages	22. Price
Unclassified	Unclassified	111	NA

Table of Contents

Table of Figures

List of Tables

List of Abbreviations

CAD: Computer-Aided Design

CDSF: Confined Discretized Solid Flame

CFD: Computational Fluid Dynamics

DoD: Department of Defense

FDS: Fluid Dynamics Simulator

FE: Finite Element

FEMA: Federal Emergency Management Agency

HGV: Heavy Goods Vehicle

HRR: Heat Release Rate

MDSF: Modified Discretized Solid Flame

NFPA: National Fire Protection Association

RWS: Rijkswaterstaat

TNT: Trinitrotoluene

VBIED: Vehicle-Borne Improvised Explosive Device

Executive Summary

Tunnels are a critical component of our transportation infrastructure, and unexpected damage to a tunnel can significantly and adversely impact the functionality of a transportation network. Tunnels are susceptible to severe fire-induced heat flux due to the constant presence of vehicular traffic combined with the likelihood of accidents and subsequent combustion. They are also vulnerable to potential threats of intentional and accidental blast that can lead to local damage (spalling and breach) and progressive collapse. This report outlines approaches for assessing fire-induced thermal demands and blast-induced damage to the concrete tunnel liner.

First, a rapid assessment approach is developed to evaluate thermal demands using models that are calibrated using computationally intensive numerical assessment, experimental data, and semi-empirical relationships based on first principles. These fast-running approaches are useful to calculate appropriate design limit states and to better understand risk potential in a multitude of underground environments. Utilizing Rhino and Grasshopper, the discretized solid flame model is adapted to account for the confinement within tunnel structures and development of a convective zone under the tunnel ceiling. The confined discretized solid flame model (CDSF) accurately captures the spatial distribution of heat flux in circular tunnels as compared to experimentally-validated, high fidelity numerical solutions. Potential for cracking, spalling, breach, and other adverse structural consequences can be evaluated based on contour maps of total heat flux over the tunnel liner.

Second, an effective approach is presented to predict and map the damage to the reinforced concrete liner of a roadway tunnel for various explosive threat sizes and tunnel geometries. The proposed fast-running approach is an alternative to either high-fidelity computational models that require massive computational effort or simplified design expressions that cannot accurately capture spatial distributions of damage. A literature review of existing evaluation methods is conducted, and potential blast event scenarios are examined with varying charge position and size. Rectangular, horseshoe, and circular tunnel geometries, each with the same traffic throughput, are evaluated. The proposed approach shows good agreement with high-fidelity numerical models analyzed in LS-DYNA and is then used to examine the relationship between increasing blast hazard intensity and the extent of spall and breach damage. Inflection points in this relationship can be used to identify hazard levels at which a progressive collapse evaluation would be warranted.

Findings

Both fast-running models are capable of providing conservatively accurate damage predictions versus experimental data and high fidelity computational solutions. These models are well suited for rapid or stochastic evaluation of reinforced concrete tunnel liners for fire and blast vulnerability assessment. The proposed approaches provide a platform for further development, which will expand the range of applicable hazard sizes and tunnel configurations.

Chapter 1: Project Scope and Background

This report summarizes the University Transportation Center on Underground Transportation Infrastructure effort focused on assessing and improving the resilience of highway and railway tunnels to fire and blast. The study develops new frameworks for evaluating the vulnerability of tunnel infrastructure to blast and fire hazards. The resulting assessment tools can be used to prioritize and tailor mitigation strategies, systems, and placement to maximize risk reduction with available resources. The project team has previously developed several fast running analysis techniques for analyzing the effects of blast and fire on large structural systems – these methodologies will be leveraged to evaluate the effects of blast and fire on large tunnels or inventories of tunnels via large batches of simulations using randomly selected inputs. Blast and fire are evaluated as separate hazards in this report –cascading hazards (e.g. a fire following an intentional explosive detonation, or the deflagration of a fuel tanker due to an initial small fire) should be considered where appropriate in future work. The results presented in this report could be reasonably leveraged and extended to consider cascading hazards.

Extreme threats such as blast, fire, and vehicle accidents pose challenges to the safety of transportation infrastructure. The threats themselves can result in direct loss of life and can lead to localized damage and catastrophic outcomes such as progressive collapse. Tunnels are typically considered critical to our national infrastructure since the incapacity or damage of such structures would jeopardize regional security as well as economic functionality. A recent Presidential Policy Directive (The White House Office of the Press Secretary 2013) has specifically stipulated the need to strengthen the security and resilience of our nation's critical infrastructure. Furthermore, an NCHRP study of transportation tunnel security recently highlighted the threats posed by intentional and accidental blast (Transportation Research Board 2006).

Fire-Induced Thermal Demands

Recent tunnel fires have highlighted the need for enhanced understanding of the structural response of reinforced concrete liners to fire events. The St. Gotthard Tunnel fire of 2001 claimed the lives of 11 people and resulted in over 250 m of collapsed concrete lining within the tunnel. In 1999, the Mont Blanc Tunnel fire resulted in 39 casualties and over 900 m of damaged tunnel lining, with the blaze continuing for over 50 hours (Carvel 2004). As space above ground becomes limited, there is a concerted effort to move transportation infrastructure underground. A major example of this momentum is the 2016 establishment of the Boring Company in California, which aims to significantly increase the presence of underground transportation ("The Boring Company" 2020).

Accurate and rapid assessment methods for tunnel systems would facilitate risk evaluation, retrofit design, suppression system deployment, and the potential development of new tunnel configurations. The array and inherent variability of inputs for modeling a fire event can be incorporated into a modified discretized solid flame (MDSF) model, which represents the flames and smoke as discretized solid objects with varying radiative power. The MDSF model was previously proposed for bridges exposed to open-air hydrocarbon fires (Quiel et al. 2015) and requires an "intermediate" level of computational effort between analytical calculations, semi-empirical models, and high-fidelity computational fluid dynamics (CFD) solutions. Adapted from the MDSF, a confined discretized solid flame model (CDSF) which geometrically redefines the solid flame shape according to tunnel confinement and fire size while also including convective effects, is presented here.

To appropriately model a severe fire in a tunnel environment, the zone model and solid flame concepts are merged into a single approach that appropriately accounts for flame radiation, smoke effects, and convection from gaseous combustion byproducts. The CDSF is capable of providing rapid yet reliable predictions of the total heat flux received by tunnel liners from a range of typical vehicle design fires (NFPA 2017). Calibration of the CDSF model is performed via comparison to experimentally validated CFD solutions developed in NIST's publicly available Fire Dynamics Simulator (FDS) (McGrattan et al. 2013). The computational efficiency of the CDSF model versus its CFD counterpart enables stochastic assessment of numerous input parameters over an inventory of tunnels. A commercial 3D computer-aided design software, Rhinoceros 3D (Robert McNeel & Associates 2017), and accompanied visual programming language, Grasshopper (Robert McNeel & Associates 2014), are utilized to implement the CDSF model for their extended capabilities in complex, parametric geometric analysis and visualization.

Blast-Induced Damage

Tunnels are particularly vulnerable to terrorist attack since most have uncontrolled public access to vehicles ranging from motorbikes and passenger cars to large cargo-hauling trucks. Though the risk of terrorist attack is generally low, consideration of these threats is amplified since (1) they typically carry high consequence; (2) they are attracted to high-impact, high-visibility targets, particularly those with lower levels of perceived security; and (3) public fear or dread of these events contributes to "probability neglect," which is the goal of most terrorist activities (Stewart et al. 2006). Between 1970 and 2015, the United States alone has seen 89 terrorist attacks targeting the transportation sector, 64% of which were carried out through bombings (Miller 2016). Tunnels specifically may pose an even greater concern because their enclosed space provides additional confinement (and thus amplification) of an explosion's effects and also presents challenges for rescue and repair efforts. Though many recent incidents around the world have involved hand-carried threats in subway tunnels (CNN 2017), US government agencies have also been focusing their mitigation efforts more on the threat posed by vehicle-borne improvised explosive devices (VBIEDs) (Transportation Research Board 2006).

The aforementioned NCHRP effort has highlighted a need for improved assessment of transportation tunnel vulnerability to blast (Transportation Research Board 2006). In particular, few available approaches can provide reasonably conservative, computationally efficient evaluations of the spatial distribution and structural consequences of blast-induced damage. Numerous research studies have examined the propagation of blast-induced pressure loads in tunnels and other confined structures via experiments (Edri et al. 2011; Stolz and Ruiz-Ripoll 2016) and high-fidelity computational fluid dynamic analysis (Feldgun et al. 2008; Pennetier et al. 2015; Uystepruyst and Monnoyer 2014). The results of these studies have made strides in establishing the temporal and spatial distribution of blast pressure on tunnel liners. Some studies have used finite element (FE) analyses to model the spalling and/or breach effects of these blast loads on the tunnel liners, which are typically constructed of reinforced concrete (Buonsanti and Leonardi 2013; Choi et al. 2006; Stolz and Ruiz-Ripoll 2016). Previous studies have collectively demonstrated that shock-induced cracking, spalling, and breach are the dominant failure modes of tunnel liners in response to blast pressure, as opposed to the flexural response that is more typical of building or bridge structures.

The most significant contributions made by previous researchers in this field have typically pertained to the use of high-fidelity modeling tools, which are computationally demanding and are not conducive to parametric assessment of tunnels subjected to blast loads. This report addresses the need for assessment tools of “intermediate” complexity, which can deliver accurate, conservative assessments of blast-induced damage at a fraction of the computational effort of high-fidelity models. A similar approach to intermediate models has been developed previously by one of the authors for the vulnerability of bridges to unconfined hydrocarbon fires (Quiel et al. 2015). This report will focus on the levels of spall and breach damage induced by VBIED hazards in typical roadway tunnels. Three tunnel prototypes with varying geometry but identical vehicle throughput are evaluated for a range of blast hazards. Spatial contours of damage are developed using the proposed approach and are compared to results obtained from high-fidelity computational analysis.

The proposed approach can be used to efficiently establish the relationship between blast hazard intensity and the extent of damage for a range of tunnel design parameters or conditions. The extent of tunnel damage can then be used as the initial condition for progressive collapse assessment of the tunnel liner. A similar approach for mapping blast-induced damage as a prelude to progressive collapse evaluation was used previously by the authors for building frame structures (Gombeda et al. 2017). The proposed approach is used to develop threat vs. damage curves that indicate appropriate hazard levels at which the potential for progressive collapse may increase. Increases in tunnel wall thickness as a function of tunnel geometry are also calculated to illustrate the relative amount of concrete needed to prevent blast-induced breach of the tunnel liner.

Chapter 2: Development and Verification of CDSF Model for Rapid Fire Evaluation

This chapter provides an overview of a confined discretized solid flame model for examining fire effects on tunnel surfaces. This information has also been provided in the Lehigh University Master of Science Thesis titled "Development and verification of CDSF for calculating heat flux on concrete tunnel liners," by Kyle Root in August 2018.

Methodologies of Evaluating Resilience

To evaluate the resilience of tunnel liners to damage resulting from fire events, engineers must first calculate the fire-induced heat exposure and then determine the structural effects due to heat transfer. There are generally three types of fire models for thermal exposure evaluation: simplified (i.e. parametric or standard) fire curves, computational fluid dynamic (CFD) models, and semi-empirical models with varying complexity. In practice, a standard fire curve is often used for its simplicity. A great deal of experimental work has been done to obtain time-temperature curves for potential types and sizes of fire in tunnels, among which the Rijkswaterstaat (RWS) time-temperature curve is one of the most widely adopted standards worldwide. In the US, the National Fire Protection Association (NFPA) defines failure criteria and fire protection performance criteria for tunnels based on the RWS curve. The fire event is represented as an upper-bound temperature time history caused by combustion of a 50m^3 fuel tanker with a heat release rate (HRR) of 300MW and duration of 120 min. The temperature rapidly increases to 1200°C in 10 minutes from ignition and remains above 1200°C for 2 hours (NFPA 2017). While the standard fire curve is easy to apply to the tunnel liner as an upper bound, it does not consider spatial distribution of heat exposure, which results in overly conservative and inefficient designs. The use of a specified temperature time history circumvents the calculation of realistic heat transfer from the fire to the liner via flame radiation and convection from smoke and hot gases resulting from combustion.

CFD analyses provide high-resolution, data-rich calculations of fire demands within enclosures. However, these models require extensive computing time and a large amount of input, most of which must be assumed if experimental data or design guidance are not available. Such an approach is not feasible for rapid assessment of an inventory of tunnels and/or for a wide range of fire scenarios, nor is it practical for a stochastic assessment of structural resilience with realistically varying material and geotechnical characteristics of the tunnel. A model of intermediate complexity is therefore necessary for evaluation of numerous tunnel fire scenarios.

CDSF Model Description

The CDSF is a radiative and convective hybrid model for calculating incident heat flux on the surface of a tunnel liner. The flame is modelled as a discretized solid object with varied emissive power. Each target surface on the tunnel liner receives straight line radiation from each discretized solid flame element. An approximate convective region, informed through computational modelling, is defined under the tunnel ceiling to account for additional thermal demands on the structure from developed ceiling jets. The summation of radiative and convective effects at each target surface is calculated and stored as shown in Figure 1. Calculated, spatial distribution of heat fluxes on the tunnel liner can then be visualized directly on the tunnel structure and used for subsequent structural evaluation.

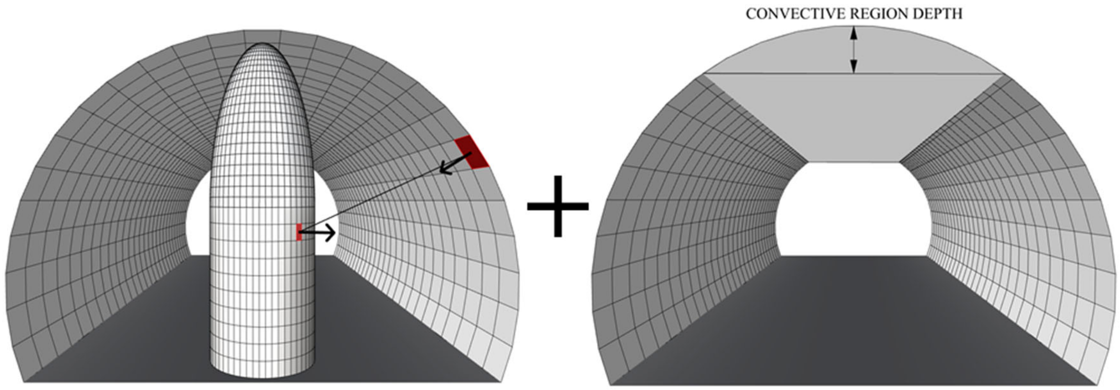

Figure 1 – Schematic of radiative and convective heat flux summation

FDS has been utilized to develop numerous aspects of the CDSF. The applicability of FDS in large-scale tunnel fires has been previously established by members of the group (Root et al. 2018) through comparisons of temperature distribution obtained through FDS and full-scale, experimental data. While the use of FDS has been integral in the development of the model presented, it is not within the scope of this thesis and will be referenced without detailed description. Full description of the FDS model parameters used throughout the development can again be found in other work by the group (Root et al. 2018).

All geometric modelling and calculation is performed using Rhino and Grasshopper, thus allowing for continuous, analytical flame shapes and rapid visualization of thermal demands. While previous model iterations only addressed horseshoe-shaped cross sections (Root et al. 2018), the CDSF has been further refined to extend the range of capability to circular tunnels. Continuing work will expand upon model parameters to accommodate an even wider array of tunnel shapes and sizes.

The input parameters to the CDSF first require a fire size, defined through peak HRR and geometric footprint. The model is generalized to accept footprints and HRR of varying size and shapes, however an approach for streamlining the input parameters has been developed. In recognition of the variability in vehicle material composition and contents, an equivalent diesel footprint is defined as a function of the HRR and initial vehicle footprint. The equivalent diesel footprint is calculated to achieve the same HRR as that specified for the vehicle type/size, while applying geometric constraints to ensure the footprint obeys a limiting aspect ratio. The aspect ratio is limited to 2.0 for the equivalent diesel footprint, where A_f *(m^2)* represents the area contained inside the rectangle. Because the applicable semi-empirical relationships are based on circular pools, previous research has indicated that using an effective diameter, $D_{f,eff}$ (Equation 1) for aspect ratios greater than 2.5 may lead to inaccuracies (McGrattan et al. 2000).

$$D_{f,eff} = \sqrt{\frac{4A_f}{\pi}} \tag{1}$$

Equation 2 shows the relationship between peak HRR, $\dot{Q}_{f,max}$ and the equivalent footprint of the pool fire (Babrauskas 2016) , where $D_{f,eff}$ is calculated from Equation 1. Remaining equation parameters are fuel specific and are obtained from previous experimental work for diesel

(Siddapureddy 2013); where $\dot{m}''$, $\Delta H_{c,eff}$ and $k\beta$ are mass loss rate in *(kg/m^2)*, effective heat of combustion in *(kJ/kg)* and an empirical constant in *(m^{-1})*, respectively.

$$\dot{Q}_{f,max} = \dot{m}''\Delta H_{c,eff} A_f (1 - e^{-k\beta * D_{f,eff}}) \tag{2}$$

Using Equations 1-2 for diesel specific combustion parameters, the rectangular, equivalent diesel footprint is solved iteratively as equal to the specified HRR as shown in Figure 2 where the dashed and solid line represent the vehicle footprint and equivalent diesel footprint, respectively.

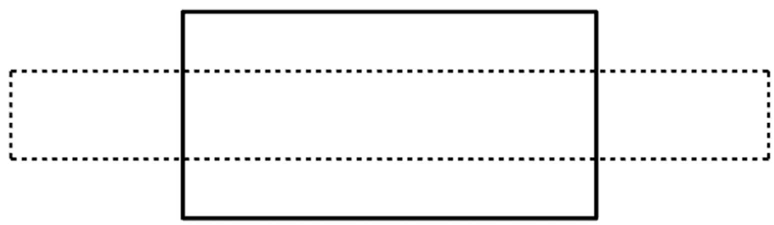

Figure 2 – Equivalent diesel footprint representation

The rectangular, equivalent diesel footprint is converted to an equivalent analytical elliptical footprint, to remove any sharp corners when the solid flame shape is extruded. An initial ellipse is inscribed in the rectangular footprint, then uniformly scaled in size to equate the perimeters of the rectangular and analytical shapes as shown below in Figure 3 (since the CDSF radiation is predicated on *surface* emissive power).

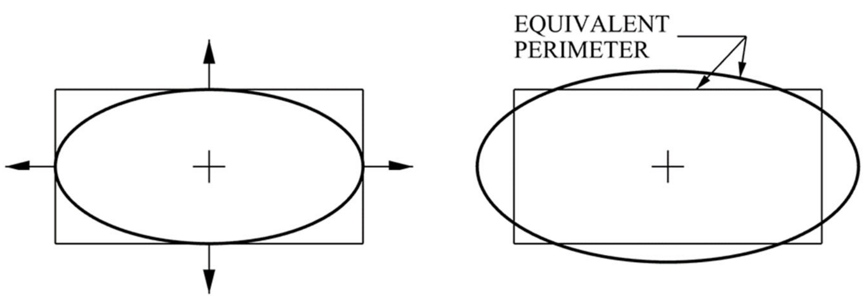

Figure 3 – Analytical elliptical footprint development

The full progression of footprints, from vehicle to analytical elliptical, is illustrated in Figure 4.

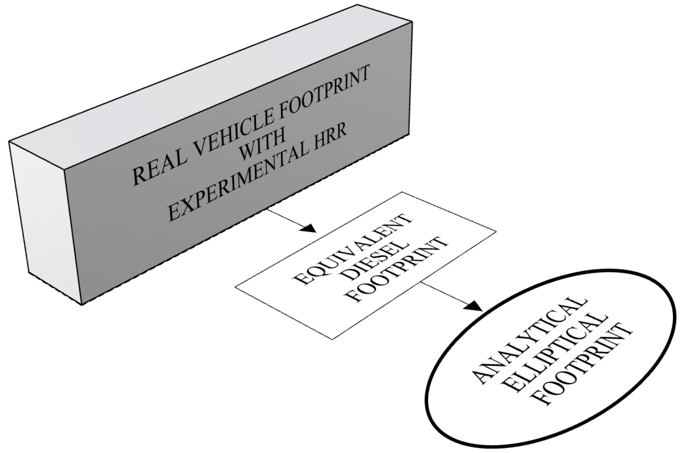

Figure 4 – Footprint development workflow

The solid flame shape generated without consideration of tunnel confinement is first calculated as the "free" flame. If the free flame height extends beyond the confines of the tunnel geometry and specified ceiling offset, the shape is compressed and becomes confined to the tunnel, called the "confined" flame shape. The flame shape, either confined or free, is then appropriately discretized for analysis and denoted as the analytical flame, for which varied emissive power is assigned to each discretized surface.

The height of the free flame H_f *(m)* is calculated as a function of the peak heat release rate, $\dot{Q}_{f,max}$ *(kW)* and effective diameter, $D_{f,eff}$, as specified in Heskestad's correlation (Hurley et al. 2016) per Equation 3.

$$H_f = 0.235\dot{Q}_{f,max}^{0.4} - 1.02D_{f,eff} \quad (3)$$

The free flame is proportioned in accordance with work done by Zhou et al., in which the solid flame is bifurcated into an extruded ellipse body and cone at $0.4H_f$ from the base of the flame (Zhou et al. 2014). To again avoid discontinuities in the solid flame shape, the pointed cone shape is replaced with a truncated ellipsoid dome, as shown in the illustrative graphic in Figure 5.

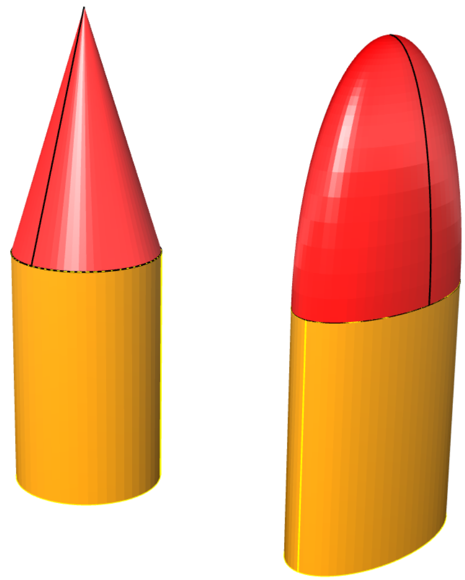

Figure 5 – Conical and elliptical flame shape comparison

This avoidance of sharp edges in the solid flame radiation calculation has been shown to produce more accurate accounting of heat flux received on the tunnel liner, especially at the tunnel ceiling in close proximity to the flame. The surface area of the free flame body and dome are represented as A_b *(m^2)* and A_d *(m^2)*, respectively. The flame emissive power in *(kW/m^2)* is assumed to be uniform across the surface of the free flame, and calculated as a function of the radiative fraction, χ_r, peak heat release rate, and total free flame surface area A in *(m^2)*, Equation 5, where radiative fraction is calculated in accordance with Equation 4 (Muñoz et al. 2007).

$$\chi_r = \begin{cases} 0.158 {D_{f,eff}}^{0.15} \; for \; D_{f,eff} \leq 5m \\ 0.436 {D_{f,eff}}^{-0.58} \; for \; D_{f,eff} > 5m \end{cases} \tag{4}$$

$$E = \frac{\chi_r \, \dot{Q}_{f,max}}{A} \tag{5}$$

As shown in Figure 6, the height of the fire's base above the road surface, H_{base} (m), approximately accounts for the bumper height of the vehicle. If the height of the free flame H_f from Equation 3, originating from H_{base} above the road surface, remains below the tunnel height minus a specified ceiling offset of $0.02H_f$, then H_f is used as the analytical flame height. However, the free flame height from Equation 3 will often exceed the height of the tunnel minus the ceiling offset for significant fires. In those cases, the analytical flame height is reduced to fit inside the tunnel enclosure, thus *confined*.

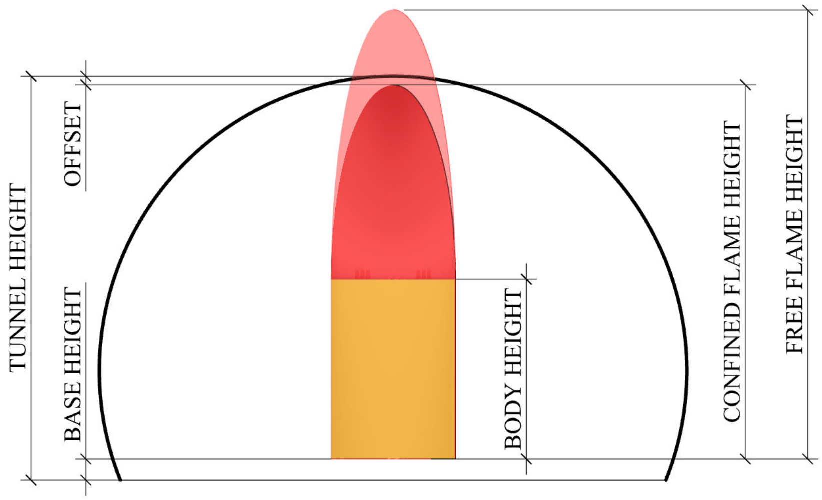

Figure 6 - Schematic comparison of the free flame and confined flame shapes

To allow the flame surfaces to have adequate view of the tunnel liner at close range and "engulf" those targets with appropriately high radiation heat flux, the top of the ellipsoid dome is restricted to an offset of $0.02H_f$ from the tunnel ceiling height. The confined flame height, H_c (m), is therefore calculated as follows.

$$H_c = H_T - 0.02H_f - H_{base} \quad (6)$$

For free flame heights that just exceed the tunnel height, the dome is simply compressed as shown in Figure 6 while the height of the extruded ellipse body remains at $0.4H_f$. As the free flame height increases for increasingly severe fires, the body height can become so large that the ellipsoid dome would be unrealistically compressed or even eliminated (resulting in poor analytical calculations of radiation heat flux on the ceiling) if no height adjustments were made to the body. To preserve the bifurcated structure of the confined solid flame, the height of the confined flame body can be no greater than 75% of H_c, and the ellipsoid dome can therefore be no less than 25% of H_c. Note that because H_c is itself a function of the free flame height, confined flame heights will actually reduce further below the tunnel ceiling with fires of increasing severity, thus accounting for the additional flame spread and pluming around the fire's center expected with increasing fire size.

Conservation of energy is preserved when free flame shapes that extend beyond the tunnel height are compressed to create the confined flame shape, which will naturally have less surface area. Since the ellipsoid dome and extruded ellipse body will experience different amounts of surface area reduction, the average emissive power over the free flame surface area, E (kW/m^2) from Equation 5 is increased by the ratios shown below in Equation 7 and Equation 8 for the body and dome of the confined flame, respectively.

$$E_b = E\left(\frac{A_b}{A_{b'}}\right) * C \quad (7)$$

$$E_d = E\left(\frac{A_d}{A_{d'}}\right) * C \quad (8)$$

A_b and A_d (both in m^2) are the areas of the free flame body and dome, and $A_b{}'$ and $A_d{}'$ (again in m^2) are the areas of the confined flame body and dome, respectively. Surface emissive power in the body, E_b (kW/m^2), and surface emissive power in the dome, E_d (kW/m^2), are applied to the analytical flame body and dome, respectively. Additionally, when the free flame height far exceeds the tunnel height and the body height is restricted to 75% of H_c, the average emissive power, E, is increased by an additional confinement factor, C, to account for increased combustion efficiency and turbulence resulting from significant confinement of the flame (Wang et al. 2017). At present, C is taken as the ratio of A_b to $A_b{}'$. Note this value equals unity for free flame body heights not exceeding 75% of H_c. As will be demonstrated, this approach to energy conservation between the free and confined solid flame models can capture the magnitude and distribution of radiation heat fluxes expected with increasing fire size as compared to the FDS solutions. Preliminary study has indicated that a maximum edge distance of 85 cm in the analytical flame mesh provides an acceptable level of resolution and convergence. Future model development will further investigate the trade-off between analysis time and slight variation in the calculated heat flux from radiation.

With analytical flame shape and surface emissive powers defined, the radiative heat flux contribution can be calculated. Radiative contribution from each emitting surface, *i,* is summed at each target surface, j. Incident heat flux at each discretized surface, q''_j is calculated as a function of the emissive power and view factor, $F_{i\to j}$ between receiving and emitting surfaces as shown below in Equation 9.

$$q''_j = \sum_{i=1}^{n} E_i F_{i\to j} = \sum_{i=1}^{n} E_i \frac{A_i \cos\theta_i \cos\theta_j}{\pi r_{i\to j}^2} \qquad (9)$$

The addition of a convective field at the tunnel ceiling is provided in the CDSF to conservatively capture ceiling jet effects. Through FDS-informed calibration, additional convective heat flux is applied to target elements within the defined convective zone, having a depth denoted as D_{CZ} in *(m)*.

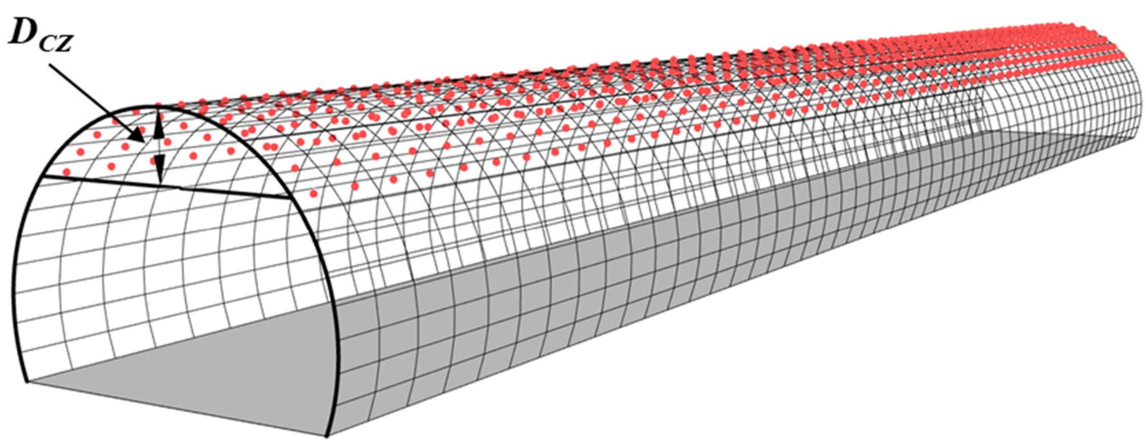

Figure 7 – Depth of convective zone under tunnel ceiling

The depth of the convective zone below the tunnel ceiling is calculated as a percentage of H_T, where D_{CZ}/H_T has been found to have the following correlation illustrated below in Figure 8 and detailed in Equation 10. Note this correlation has only been made for fire sizes between 30MW and 200MW. Additional analysis and comparisons should be performed before extending the application of the convective depth calibration to fire sizes outside of this range.

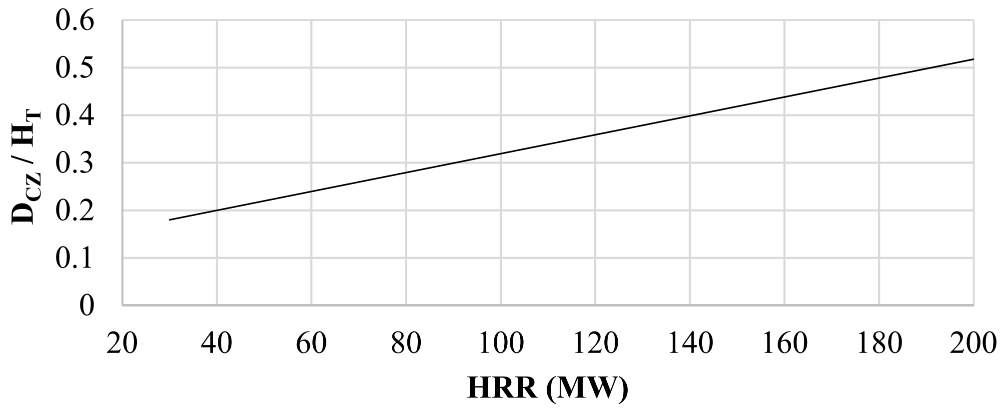

Figure 8 – Depth of convective zone calibration

$$\frac{D_{CZ}}{H_T} = 0.002\,(HRR) + 0.1204 \tag{10}$$

Kurioka et al. determined a power scaling fit for longitudinal temperature decay in the smoke filled region accumulating under a tunnel ceiling (Kurioka et al. 2003). Using an FDS-informed fit correlated to peak heat release rate and tunnel size, a similar model has been developed for the longitudinal decay of convective heat flux under the tunnel ceiling. A maximum convective heat flux is first defined with the fit determined below in Figure 9 and detailed in Equation 11.

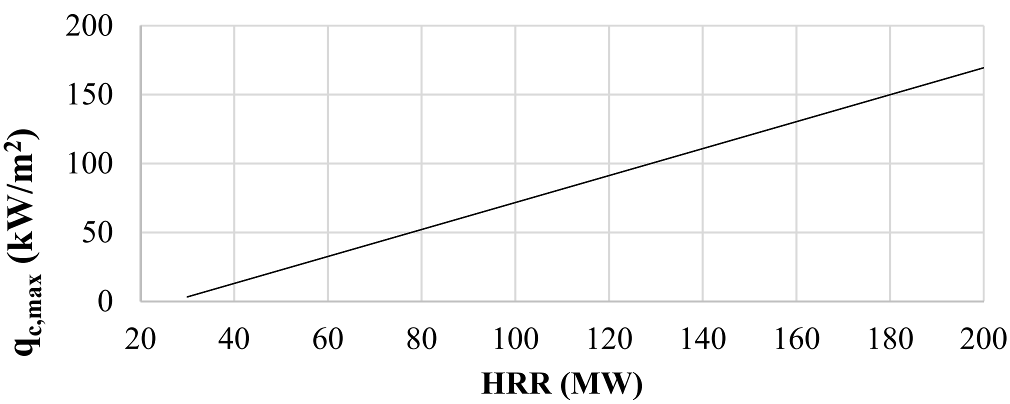

Figure 9 – Maximum convective heat flux calibration

$$q_{c,max} = 0.9788\,(HRR) - 26.118 \tag{11}$$

The longitudinal scaling from $q_{c,max}$ is detailed in Equations 12-14 below, where x in *(m)*, represents the longitudinal distance from the fire center.

$$\frac{q_c}{q_{c,max}} = \alpha\left(\frac{x}{H_T}\right)^{\beta} \tag{12}$$

$$x_0 = 0.26\dot{Q}_{f,max}{}^{0.2} \tag{13}$$

$$\frac{x}{H_T} \leq x_0,\ \alpha = 1,\ \beta = 0 \tag{14}$$
$$\frac{x}{H_T} > x_0,\ \alpha = 0.09\dot{Q}_{f,max}^{\ 0.4},\ \beta = -2.8\dot{Q}_{f,max}^{\ -0.2}$$

This longitudinal scaling from maximum convective heat flux is illustrated below for a range of HRR – note that the horizontal axis denotes the value x *(m)*, and the vertical axis represents maximum convective heat flux at that longitudinal distance, q_c *(kW/m²)*. The correlated scaling has proven to accurately capture the longitudinal spread and magnitude of large-scale fires ranging from 30MW to 200MW.

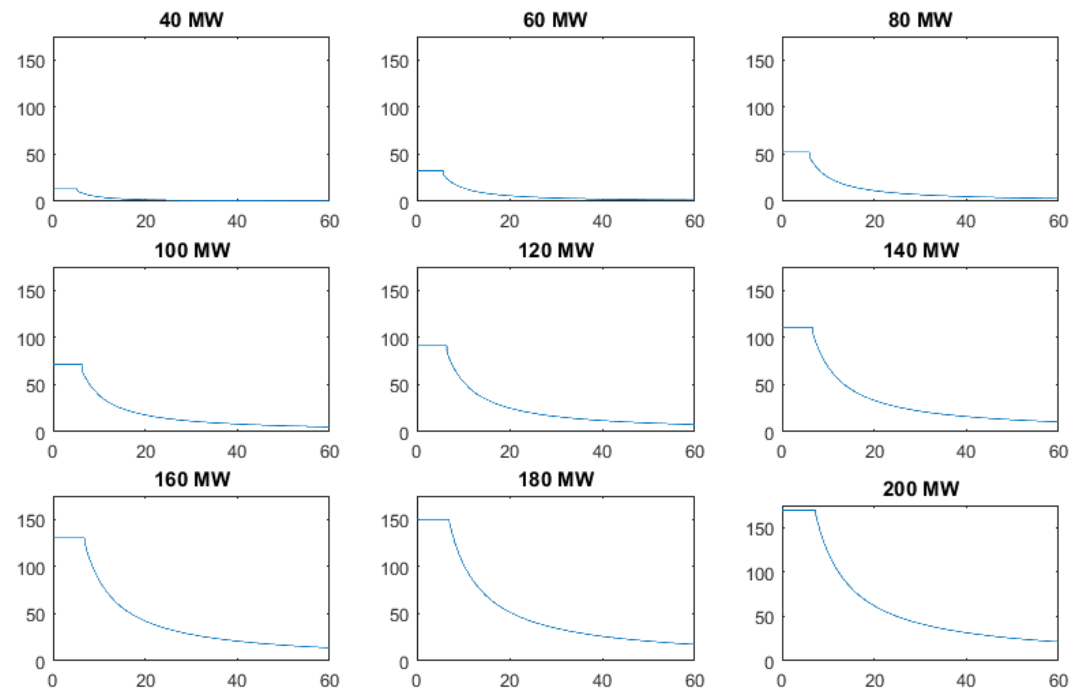

Figure 10 – Longitudinal scaling of maximum applied convective heat flux

The convective heat flux is scaled linearly through the depth of the convective zone, as informed by Hu (Hu et al. 2004), who noted a strong correlation between smoke temperature and distance below tunnel ceiling. A sample convective zone illustrating the applied q_c in *(kW/m²)* is shown below for a 70MW fire in Figure 11.

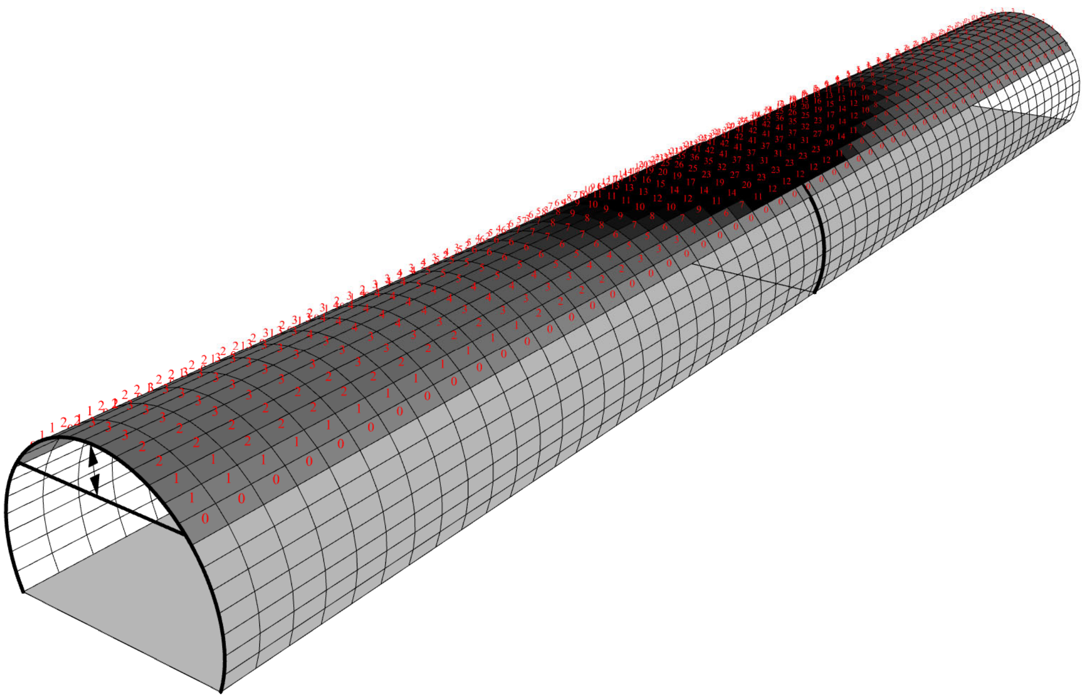

Figure 11 – 70 MW convective heat flux distribution

The correlations presented for additional heat flux applied within the convective zone have been determined for fire sizes ranging from 30MW to 200MW in a circular tunnel. Work done by others notes the dependency on tunnel ceiling shape to the heat accumulation under the ceiling, even with equal cross-sectional area (Kurioka et al. 2003). Preliminary analysis suggests the applicability of these correlations to horseshoe-shaped cross sections, however future work will consider generalizing the approach to accurately capture differing heat accumulation under tunnels with flat ceilings. Combining radiative and convective effects at each tunnel element yields a total mapping of incident heat flux (in kW/m^2) on the tunnel liner, as shown below in Figure 12. The full workflow in Grasshopper can be seen illustrated in Appendix B.

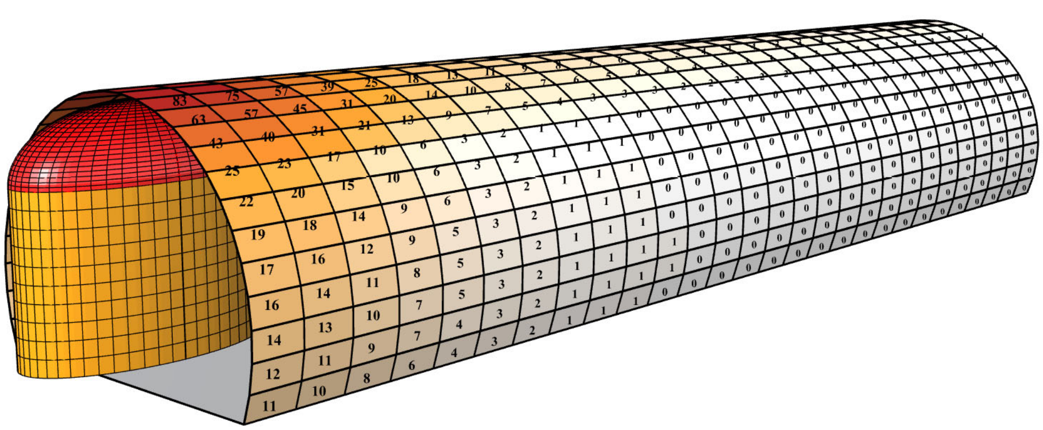

Figure 12 – Example symmetric heat flux distribution at the fire location

Illustrative Example and Model Verification

To demonstrate the application of the CDSF in a manner which allows for complete visualization of the process, an illustrative example is carried out below. A tunnel cross section must first be selected. The circular tunnel chosen here is representative of a real tunnel in service, dimensions shown below in Figure 13.

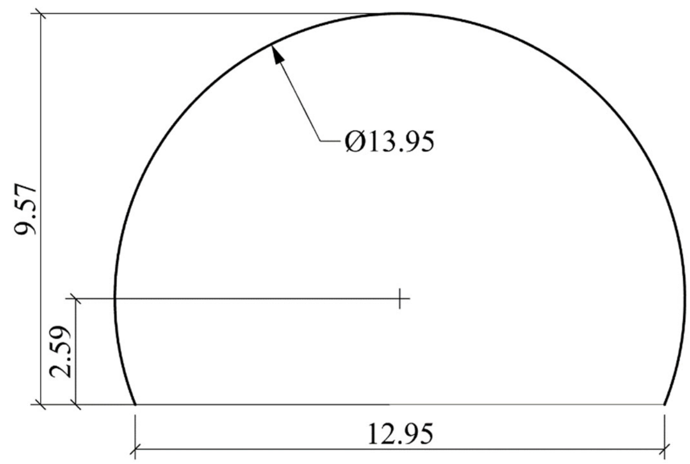

Figure 13 – Circular tunnel dimensions

The tunnel cross section is extruded in the longitudinal direction to the desired analysis length and meshed. A total analysis length of 110 meters is selected here. For illustrative purposes, the tunnel walls have been crudely discretized for simplification during the verification process, with 10 elements along both the longitudinal and circumferential axes. The tunnel analysis mesh with 100 total faces is shown below in Figure 14.

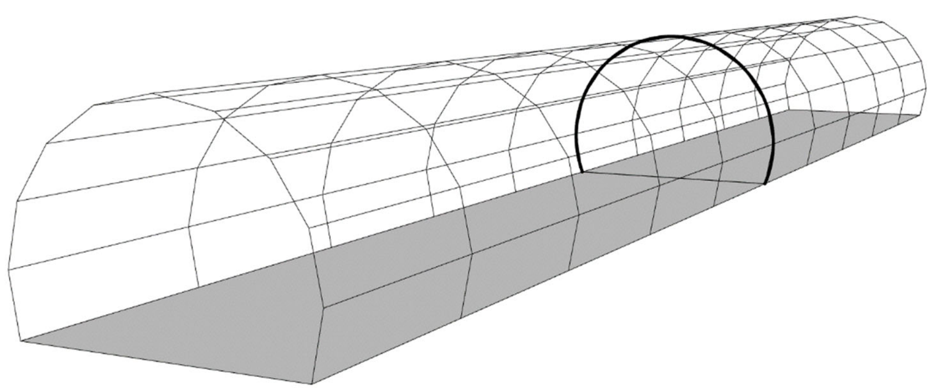

Figure 14 – Tunnel mesh coarse discretization

With the tunnel analysis mesh defined, the fire must next be defined. A 70 MW fire is selected here as representative of a light heavy goods vehicle (HGV) (Association 2011). Dimensions of the HGV as illustrated in Figure 15, are taken from vehicle WB-12 in AASHTO design guidance (American Association of State Highway and Transportation Officials 2001).

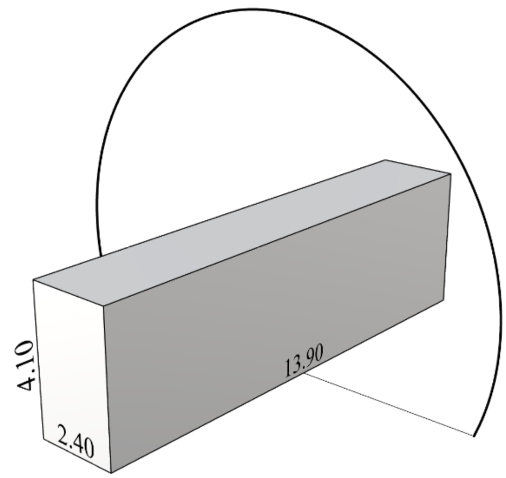

Figure 15 – Light HGV vehicle dimensions in tunnel cross section

First, the aspect ratio, A_r of the vehicle footprint is calculated as the ratio of the long edge, L_f *(m)* to the short edge, W_f *(m)*.

$$A_r = \frac{L_f}{W_f} = \frac{13.90\ m}{2.40\ m} = 5.79$$

Limiting the aspect ratio to 2.0 to remain within the acceptable range of the semi-empirical formula for flame height (Equation 3), the equivalent rectangular diesel footprint is iteratively calculated to satisfy the relationship between effective diameter $D_{f,eff}$ (Equation 1) and peak HRR, $\dot{Q}_{f,max}$. Combustion parameters are obtained from previous experimental work for diesel (Siddapureddy 2013); where mass loss rate, $\dot{m}''$is 0.057 *kg/m²-s*, heat of combustion, $\Delta H_{c,eff}$ is 47,000 *kJ/kg* and $k\beta$ is an empirical constant equaled to 1.16 m^{-1}. Results of the iterative calculation are shown satisfied for the conditions below, yielding the equivalent rectangular footprint with dimensions 7.23 *m* by 3.62 *m*.

$$\dot{Q}_{f,max} = \dot{m}''\Delta H_{c,eff} A_f \left(1 - e^{-k\beta * D_{f,eff}}\right)$$

$$0.057\frac{kg}{m^2 s} * 47{,}000\frac{kJ}{kg} * 26.2m^2\left(1 - e^{-1.16m^{-1}*5.77\text{m}}\right) = 70MW$$

Comparison between vehicle footprint, dashed, and the calculated, equivalent diesel footprint, solid, is shown below in Figure 16.

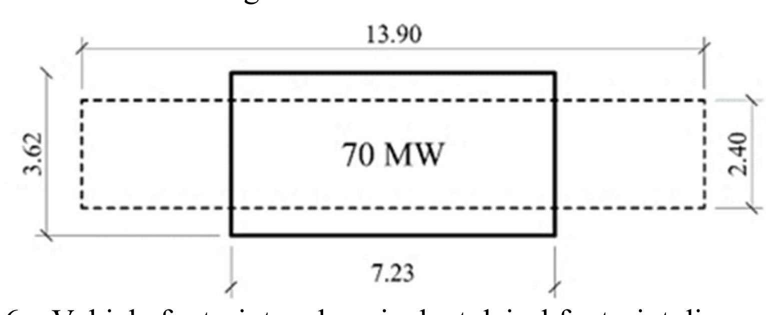

Figure 16 – Vehicle footprint and equivalent deisel footprint dimensioned (*m*)

Radiative fraction is calculated in accordance with Equation 4, for the case in which diameter is larger than 5 m as $D_{f,eff}$ has been calculated as 5.77 m. Important to note, is that $D_{f,eff}$ is used in the calculation of radiative fraction.

$$\chi_r = 0.436D^{-0.58} = 0.158$$

Discontinuities in the subsequent solid flame shape are now removed by converting the equivalent diesel footprint into the analytical, elliptical footprint. An initial ellipse is first inscribed in the equivalent diesel footprint. However, because the solid flame model is predicated on surface emissive power, the ellipse is uniformly scaled to achieve the same perimeter as that of the equivalent diesel footprint. Final dimensions of the elliptical footprint are shown in Figure 17.

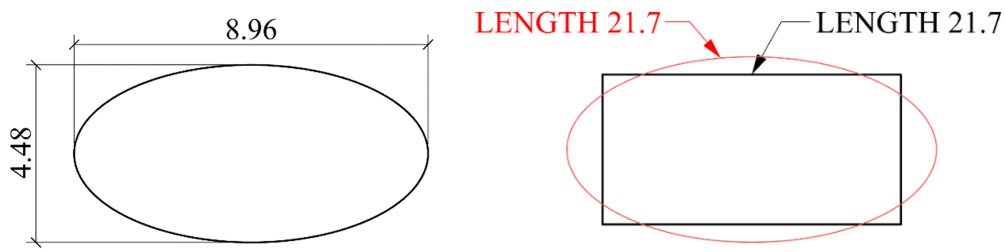

Figure 17 – Analytical elliptical footprint (m)

Free flame height in *(m)*, independent of tunnel confinement, can then be determined through Heskestad's semi-empirical correlation (Equation 3).

$$H_f = 0.235 * (70MW)^{0.4} - 1.02 * (5.77m) = 14.49m$$

The free flame is portioned into the body and dome at a height of $0.4H_f$.

$$0.4H_f = 0.4(14.49m) = 5.80m$$

The flame is assumed to act 1 m above the road surface to account for vehicle height, H_{base} equalled to 1 m, illustrated below in Figure 18.

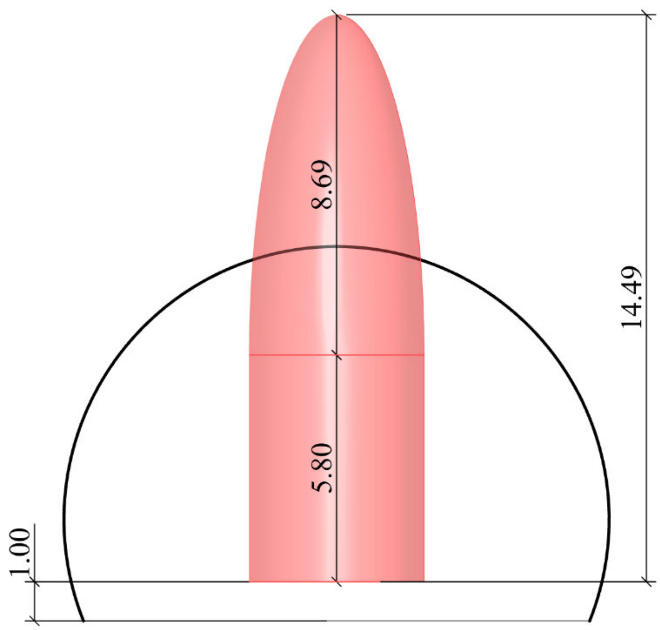

Figure 18 – Dimesioned free flame in tunnel cross section (m)

The surface areas of the free flame body, A_b and dome, A_d are geometrically calculated in the workflow as 125.8 *m*² and 154.9 *m*², for a total free flame area, A of 280.7 *m*². Average surface emissive power can be determined through Equation 5 as shown below.

$$E = \frac{0.158*70E3kW}{280.7m^2} = 39.34\frac{kW}{m^2}$$

Because the calculated free flame clearly extends above the limiting elevation, tunnel confinement is now taken into account by reducing the flame height and thus generating the new, confined flame. As stated in Equation 6, the confined flame height is calculated as follows, where the height of the tunnel, H_T can be seen in the dimensioned cross section in Figure 13 as 9.57 *m*. The confined flame dome extends up to the specified offset from the tunnel ceiling, calculated as 2% of the free flame height.

$$offset = 0.02(14.49\text{m}) = 0.290m$$

The height of the confined flame body is set to 75% of the confined flame height in the tunnel.

$$H_c = H_T - offset - H_{base} = 9.57\text{m} - 0.290\text{m} - 1\text{m} = 8.28\text{m}$$

$$0.75H_c = 0.75(8.28\text{m}) = 6.21\text{m}$$

Therefore, because the height of the body in the free flame, 5.80 *m*, is less than 75% of the confined flame height, the height of the body in the confined flame is maintained as the height of body in the free flame. The dimensioned confined flame can be seen below in Figure 19.

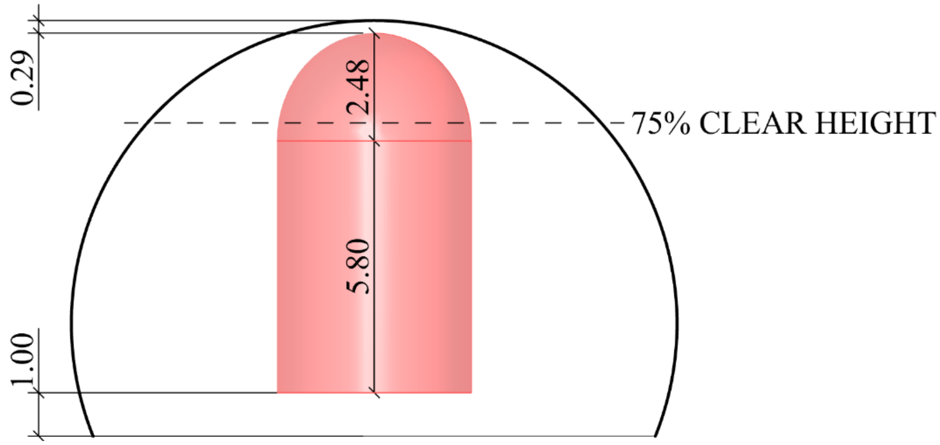

Figure 19 – Dimesnioned confined flame (m)

With the confined flame shape defined, it can now be carried through to analysis, thus becoming the analytical flame. Emissive power in the body and dome of the analytical flame are next calculated. The confining factor C is taken as unity here as A_b is equal to $A_b{}'$ when the free flame body is not geometrically reduced. Surface areas of the analytical body, $A_b{}'$ in *(m^2)* and dome, $A_d{}'$ in *(m^2)* are again built into the workflow and calculated as 125.8 m^2 and 57.24 m^2, respectively. Utilizing the expressions outlined in Equation 7 and Equation 8 to increase emissive power in the body and dome, the following values are determined.

$$E_b = 39.34\frac{kW}{m^2}\left(\frac{125.8m^2}{125.8m^2}\right) * 1.0 = 39.34\frac{kW}{m^2}$$

$$E_d = 39.34\frac{kW}{m^2}\left(\frac{154.9m^2}{57.24m^2}\right) * 1.0 = 106.4\frac{kW}{m^2}$$

With varied emissive power acting over the analytical flame, the radiative effects from each, discretized fire surface can now be calculated and summed at every target surface on the tunnel liner. The analytical flame mesh selected for this illustrative example is extremely coarse, with only 12 elements in the body and 8 elements in the dome. The discretization in the flame used is purely for demonstrative purposes, and it must be noted that a flame mesh with so few elements is not recommended for calculation. Preliminary study has indicated a maximum edge distance of 85 cm in the analytical flame mesh provides an acceptable level of resolution and convergence. Future studies will further investigate the trade-off between analysis time and slight variation in the calculated heat flux from radiation. A comparison between mesh size used for this example, 20 elements, relative to the typical mesh size used in analysis, 1890 elements, can be seen below in Figure 20.

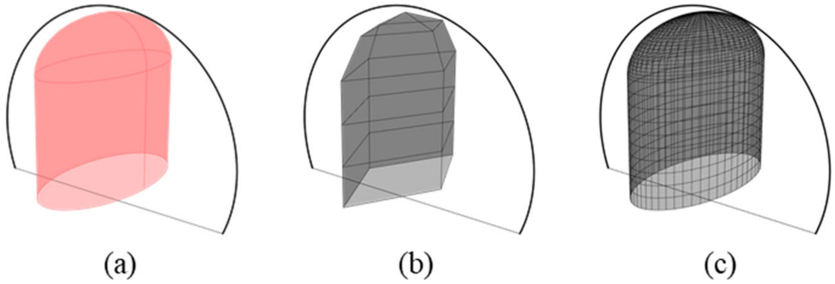

Figure 20 – Analytical solid flame (a) coarse mesh (b) and typical analytical mesh (c)

Normal vectors at each flame center and each target surface can be visualized to verify appropriate sense of the vectors before calculation of the view factors, Figure 21 and Figure 22, below. More specifically, flame normal vectors should be pointed out toward the tunnel mesh, and target normal vectors pointed in toward the flame mesh.

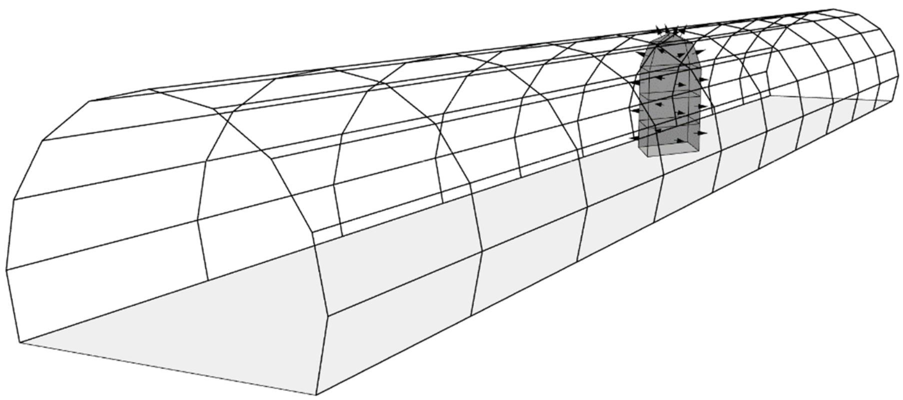

Figure 21 – Flame mesh normal vectors

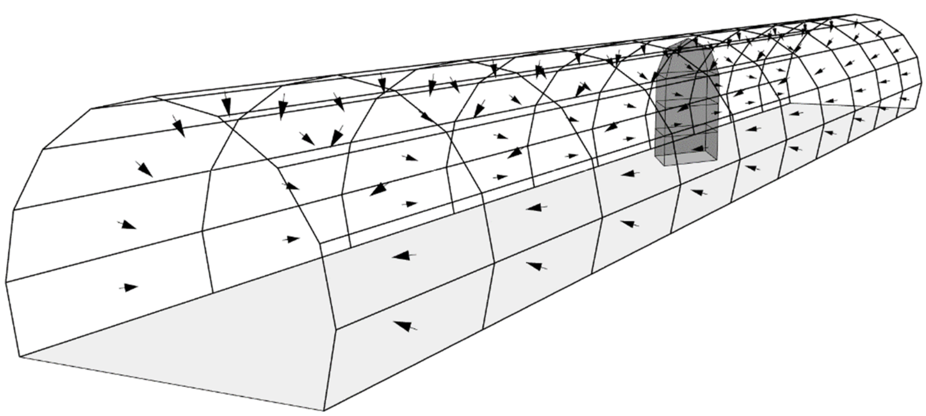

Figure 22 – Tunnel mesh normal vectors

For this example, two target surfaces are selected – one close to the road surface 16.5 *m* in the longitudinal direction from the center of fire source, tunnel mesh element number 30, and one near the tunnel ceiling 5.5 *m* in the longitudinal direction from the center of the fire source, tunnel mesh element number 54 shown below in Figure 23.

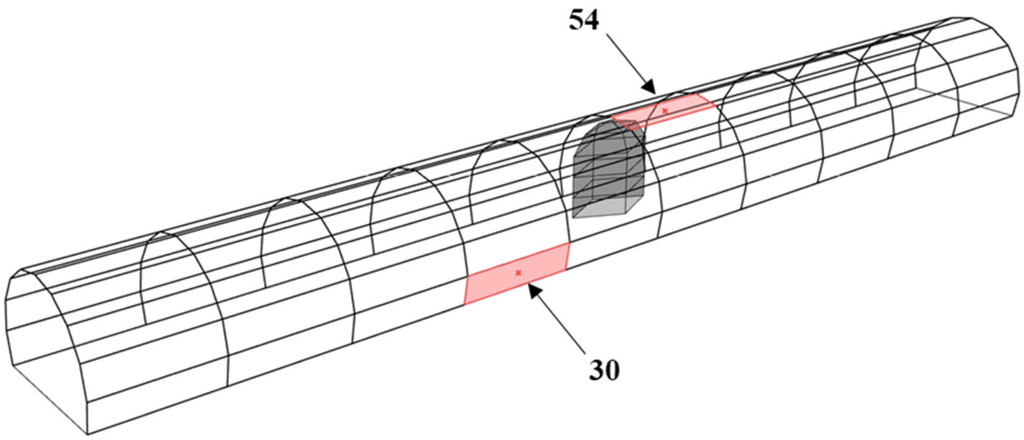

Figure 23 – Selected tunnel mesh elements

Originating from the center of each target element, j, chords are defined to the centers of each of flame mesh element, i. A total of n_i x n_j chords are defined, where n_i and n_j represent the number of elements in the flame mesh and tunnel mesh, respectively. The relative angle between the chord connecting a given target center to flame center, and normal vector at that flame element is defined as θ_i in *(degrees)*, and the relative angle between the same chord and normal vector at each target element is defined as θ_j in *(degrees)*. The length of the chord is measured as $r_{i \to j}$ in *(m)*, and the surface area of the flame mesh face is additionally calculated and stored as A_i in *(m^2)*. The summation of energy on each flame element received at tunnel mesh element number 30 can be seen below in Figure 24.

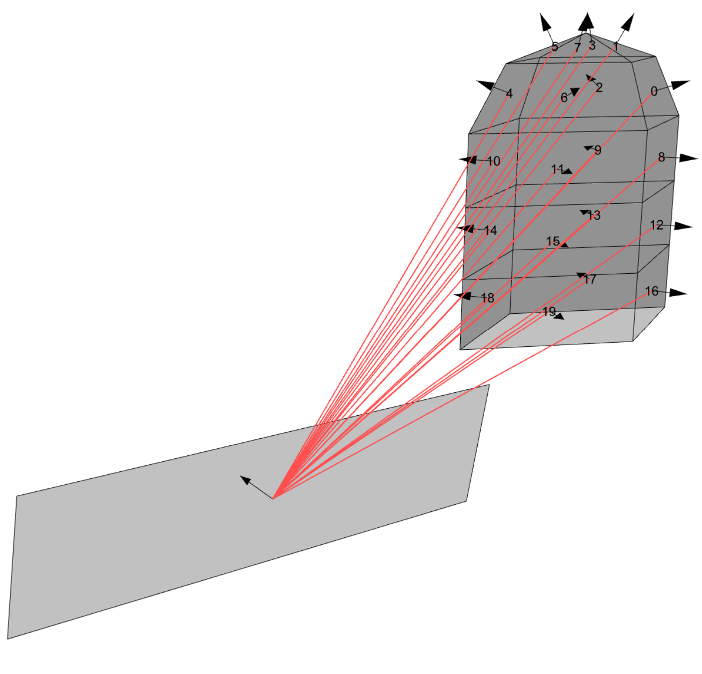

Figure 24 – Chords beween tunnel mesh element number 30 and flame mesh elements

In the given flame discretization, only a few elements have the radiation angles necessary for the selected target surface to receive radiation. More specifically, when the product of the cosines of angles θ_i and θ_j is less than or equal to 0, the view factor is set to 0, as the flame element is “unable to see” the target surface in the orientation. The summation of energy is tabulated for tunnel mesh element number 30 below in Table 1.

Table 1 – Summation of radiative energy for tunnel mesh element number 30

	INDEX	E_i $\left(\frac{kW}{m^2}\right)$	A_i (m^2)	θ_i	θ_j	$r_{i\to j}$ (m)	$F_{i\to j}$	$E_iF_{i\to j}$ $\left(\frac{kW}{m^2}\right)$
DOME	0	106.439	7.911	104.044	70.321	20.311	0.000	0.000
	1	106.439	2.821	112.728	67.506	19.915	0.000	0.000
	2	106.439	7.911	141.3	65.385	20.935	0.000	0.000
	3	106.439	2.821	130.79	65.409	20.18	0.000	0.000
	4	106.439	7.911	97.616	60.422	17.665	0.000	0.000
	5	106.439	2.821	110.017	63.53	18.841	0.000	0.000
	6	106.439	7.911	57.595	66.158	16.921	0.002	0.203
	7	106.439	2.821	92.964	65.757	18.556	0.000	0.000
BODY	8	39.337	9.678	99.661	71.59	20.072	0.000	0.000
	9	39.337	9.678	137.734	65.767	20.809	0.000	0.000
	10	39.337	9.678	92.171	59.615	16.886	0.000	0.000
	11	39.337	9.678	44.493	66.612	15.969	0.003	0.135
	12	39.337	9.678	99.831	72.347	19.729	0.000	0.000
	13	39.337	9.678	138.763	66.441	20.478	0.000	0.000
	14	39.337	9.678	92.225	60.214	16.477	0.000	0.000
	15	39.337	9.678	42.842	67.35	15.536	0.004	0.142
	16	39.337	9.678	99.911	73.292	19.571	0.000	0.000
	17	39.337	9.678	139.253	67.346	20.327	0.000	0.000
	18	39.337	9.678	92.251	61.272	16.288	0.000	0.000
	19	39.337	9.678	42.027	68.475	15.335	0.004	0.140
						∑		**0.620**

Flame elements with non-zero view factors are highlighted below in Figure 25 and can be additionally verified for corresponding indexing, angles, curve lengths, and flame surface areas as compared to those tabulated above.

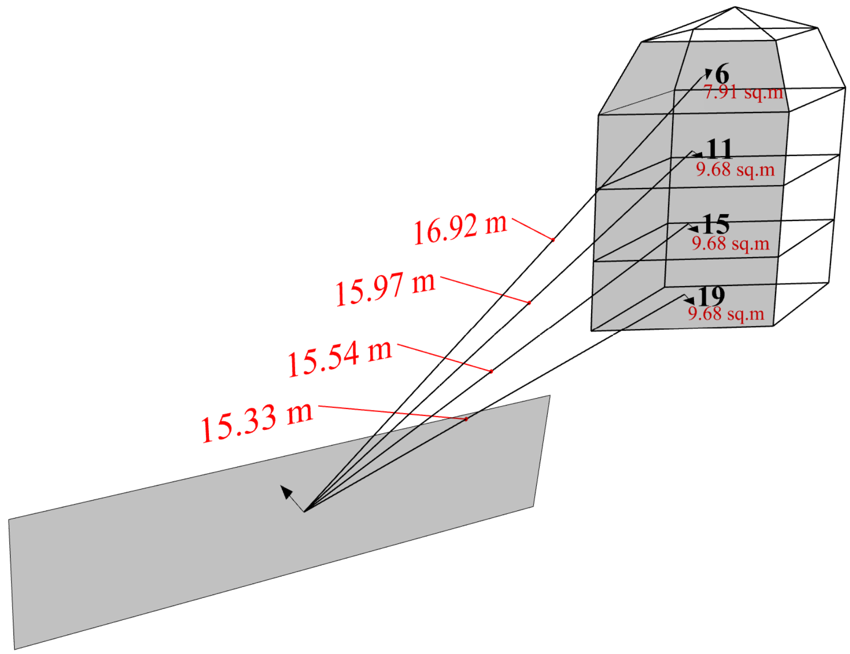

Figure 25 – Chords connecting tunnel mesh element number 30 to flame mesh elements having non-zero view factor

Additional verification is provided at tunnel mesh element 54, illustrated in Figure 23. Chords between the tunnel mesh element center and flame element centers with non-zero view factors can be seen below in Figure 26.

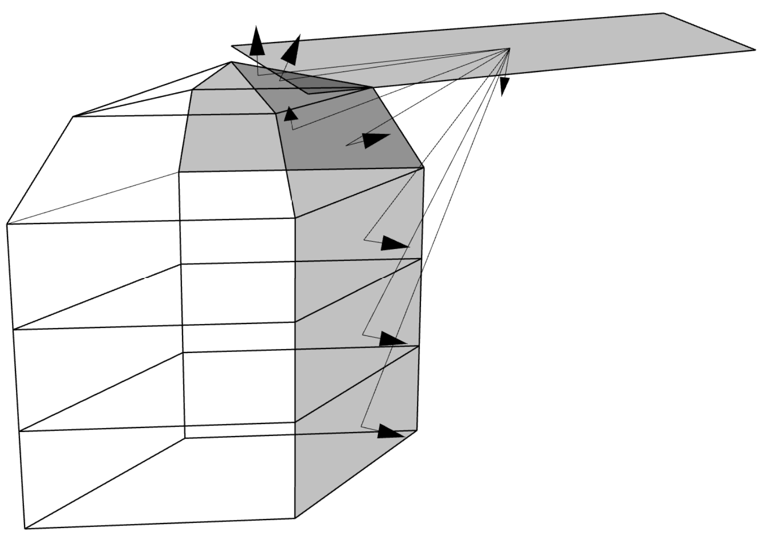

Figure 26 - Chords connecting tunnel mesh element number 54 to flame mesh elements having non-zero view factor

The corresponding tabulated summation of radiation received at tunnel mesh element number 54 can be seen below in Table 2. As is expected, the flame elements in the dome contribute significantly to the radiative energy received by the tunnel element because of the increased emissive power, comparatively small radiative angles, and short standoff distances.

Table 2 - Summation of radiative energy for tunnel mesh element number 54

	INDEX	E_i $\left(\frac{kW}{m^2}\right)$	A_i (m^2)	θ_i	θ_j	$r_{i\to j}$ (m)	$F_{i\to j}$	$E_iF_{i\to j}$ $\left(\frac{kW}{m^2}\right)$
DOME	**0**	106.439	7.911	53.518	65.012	3.959	0.040	4.295
	1	106.439	2.821	69.472	83.274	4.815	0.002	0.169
	2	106.439	7.911	88.706	63.349	4.555	0.001	0.131
	3	106.439	2.821	83.085	81.796	5.028	0.001	0.065
	4	106.439	7.911	125.149	75.062	7.926	0.000	0.000
	5	106.439	2.821	104.528	83.697	6.535	0.000	0.000
	6	106.439	7.911	107.714	77.287	7.599	0.000	0.000
	7	106.439	2.821	95.009	84.923	6.373	0.000	0.000
BODY	**8**	39.337	9.678	69.851	43.683	4.769	0.034	1.327
	9	39.337	9.678	97.843	43.532	5.356	0.000	0.000
	10	39.337	9.678	129.787	63.913	8.830	0.000	0.000
	11	39.337	9.678	112.716	66.026	8.487	0.000	0.000
	12	39.337	9.678	74.927	32.219	6.316	0.017	0.668
	13	39.337	9.678	96.197	31.415	6.771	0.000	0.000
	14	39.337	9.678	125.406	53.671	9.753	0.000	0.000
	15	39.337	9.678	110.306	55.539	9.444	0.000	0.000
	16	39.337	9.678	78.200	25.679	8.032	0.009	0.346
	17	39.337	9.678	94.995	23.917	8.394	0.000	0.000
	18	39.337	9.678	121.090	45.477	10.943	0.000	0.000
	19	39.337	9.678	107.892	47.269	10.668	0.000	0.000
							$\sum$	**7.002**

Looking at the typical CDSF output for radiation only, the values calculated above can be verified once more as shown in Figure 27, highlighting the heat flux in *(kW/m^2)* for tunnel mesh elements number 30 and number 54.

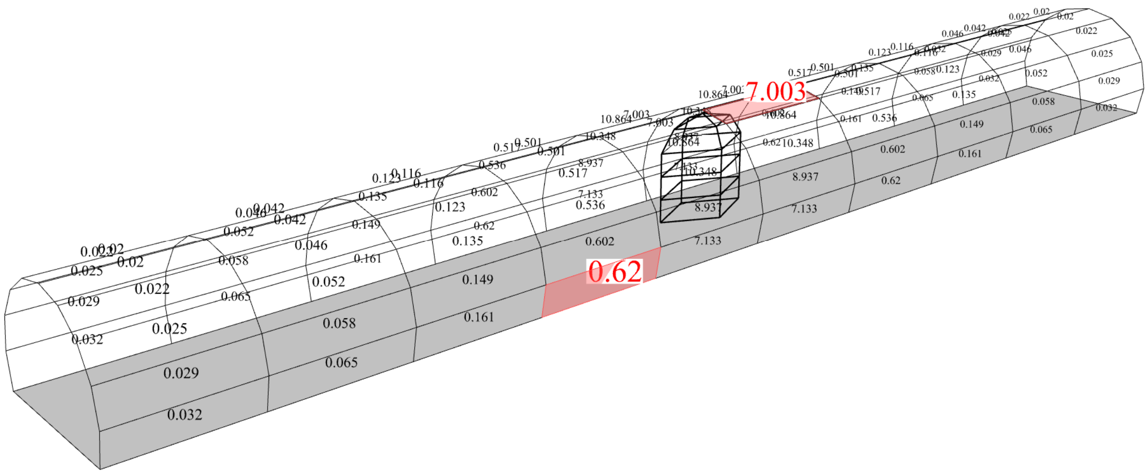

Figure 27 – Radiative heat flux output highlighting selected tunnel mesh elements

With the radiative component of the CDSF verified, the illustrative example will be extended to include the additional convective heat flux imparted on the target elements within the defined convective zone. The depth of the convective zone is first determined per the empirical correlation provided in Figure 8 and Equation 10.

$$\frac{D_{CZ}}{H_T} = 0.002(70MW) + 0.1204 = 0.260$$

For the tunnel height, H_T of 9.57 m, the depth of the convective zone is calculated as 2.49 m. Target elements with an elevation greater than or equal to $H_T - D_{CZ}$ are shown below in Figure 28.

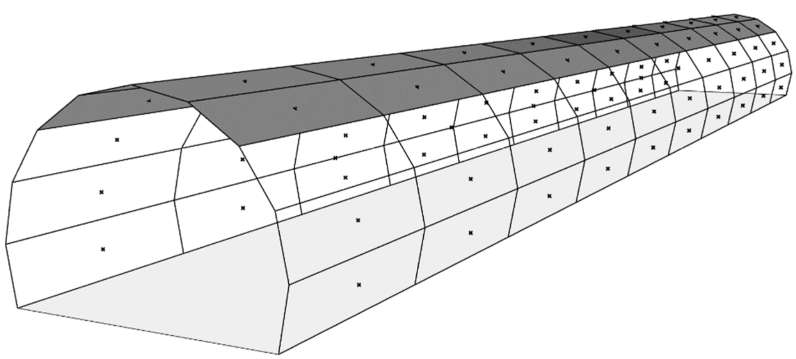

Figure 28 – Target elements within convective zone

Maximum convective heat flux is determined through the empirical correlation shown in Figure 9 and Equation 11.

$$q_{c,max} = 0.9778(70MW) - 26.118 = 42.3\ \frac{kW}{m^2}$$

Applying the longitudinal scaling correlations detailed in Equations 12-14 to $q_{c,max}$, and again scaling linearly through the depth of the convective zone, the following spatial distribution of applied convective heat flux in *(kW/m^2)* rounded to the nearest integer, on the tunnel is determined. The convective, radiation only, and sum total incident heat flux in *(kW/m^2)* are shown below in Figure 29.

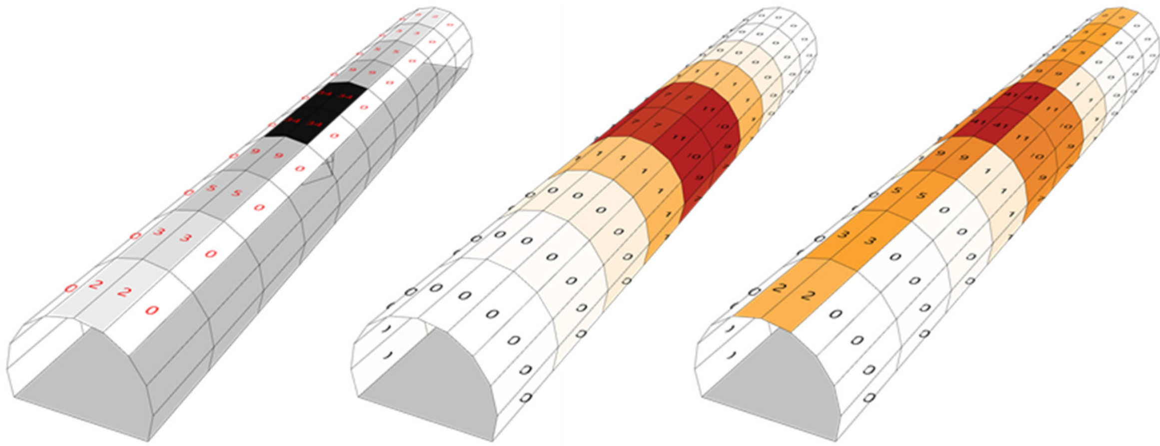

Figure 29 – Convective, radiative, and total incident heat flux (left to right)

2.4 Comparison to FDS

To show accuracy of the current iteration of the CDSF, three fire sizes have been analyzed and compared against experimentally validated FDS solutions. The same tunnel cross section shown previously in Figure 13 is used for comparison. Tunnel wall thickness is taken as 630 *mm* per previous work done by the author in the case of tunnel blast damage utilizing the same cross section (Bai et al. 2018). The selected scenarios represent three types of vehicular fires: bus, light HGV and heavy HGV with HRR of 30MW, 70MW and 200MW, respectively (Association 2011). Vehicle dimensions are selected in accordance with available design guidance AASHTO (American Association of State Highway and Transportation Officials 2001), shown in the analyzed tunnel cross section for scale, Figure 30.

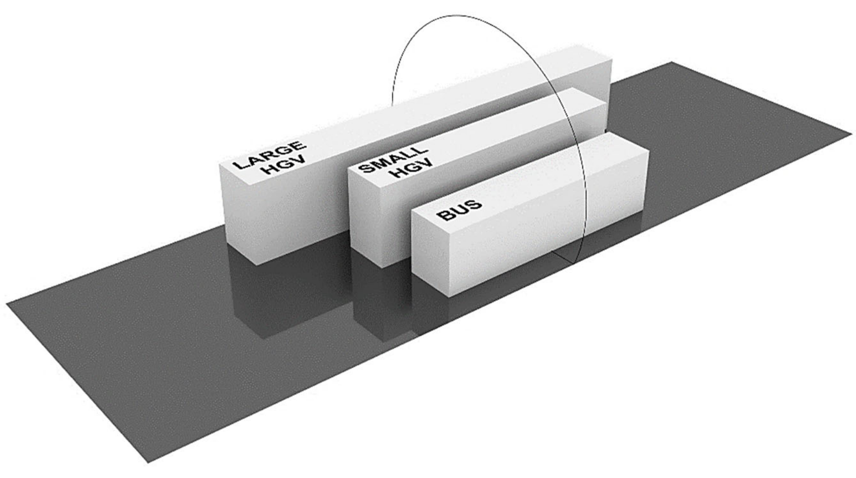

Figure 30 – Vehicle scenarios in tunnel cross section

Equivalent diesel footprints (solid) and vehicle footprints (dashed) are additionally shown below in Figure 31.

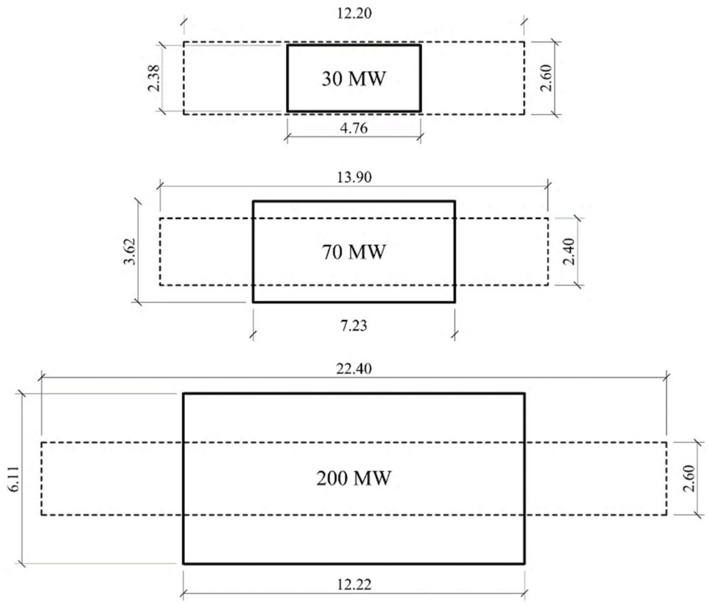

Figure 31 – Dimensioned equivalent diesel footprints (*m*)

Analysis carried out with the CDSF is presented at select locations along the ceiling, sidewall and cross section of the tunnel for FDS comparison, shown in Figure 32 below.

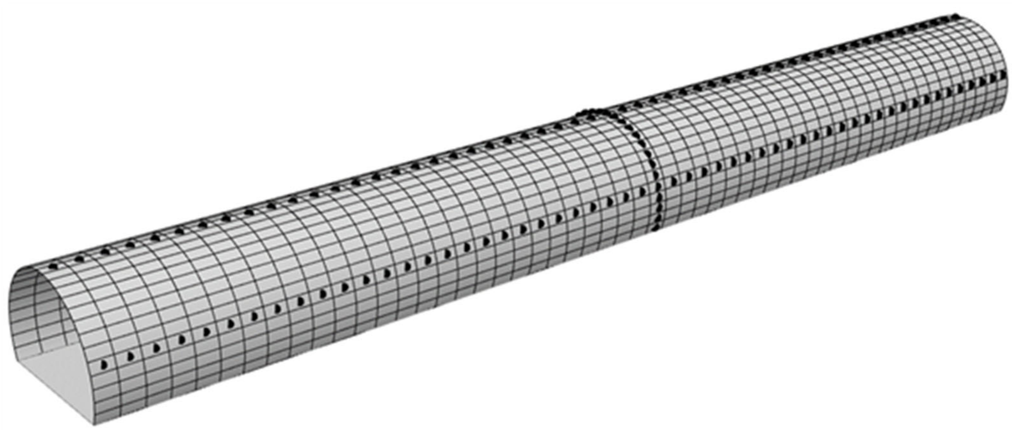

Figure 32- Measurements locations along ceiling, sidewall and cross section

While the CDSF output provides a single heat flux value at each target location, FDS provides a heat flux time history at selected measurement points. To represent the time histories generated from FDS, comparable to those from the CDSF, an upper and lower bound are determined statistically. The time history of heat fluxes (solid) shown below in Figure 33 are those directly measured at one location in the tunnel for the three selected fire sizes in FDS. The mean +/- one standard deviation is included with the time histories for the heat fluxes measured after the user-specified 30-second ramp-up threshold as the upper and lower bounds (dashed).

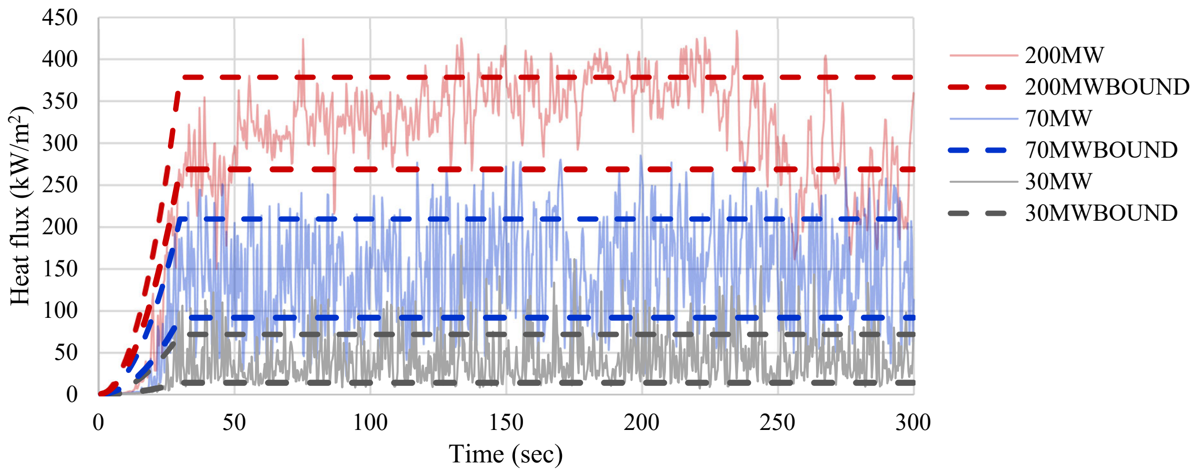

Figure 33 - Heat flux time history with upper and lower bounds

When considering thermal effects on humans in the event of a tunnel fire, it is appropriate to consider only peak values of thermal demands, however the case is different when evaluating thermal demands to be considered for resulting structural consequence. Through thickness temperature gradients are important in characterizing the structural response of concrete in fire for resulting damage, spalling or cracking (Le et al. 2016). Therefore, a representative analysis of thermal gradients developed from different magnitudes of heat flux is presented. Utilizing SAFIR (Franssen and Gernay 2017), a time-dependent heat flux is applied on one face of the concrete panel and temporal temperature gradients are calculated. The tunnel liner is discretized into 100 layers through its thickness to be used in the 1-D heat transfer analysis.

Ambient temperature is applied as a thermal boundary condition using the SAFIR defined F20 function. The concrete is defined as SILCONC_EN (i.e. siliceous concrete) in SAFIR, and the thermal properties are assumed according to Eurocode 2 (CEN 2008). Input parameters are summarized below in Table 3.

Table 3 – SILICON properties used in SAFIR

Specific mass of concrete (including moisture content)	2300 kg/m^3
Water content	45 kg/m^3
Coefficient of convection on heated surfaces	25 W/m^{2}K
Coefficient of convection on unheated surfaces	4 W/m^{2}K
Emissivity	0.8
Conductivity tuning parameter	0.5

Upper and lower bound time histories start with a 30-second t^2 ramp up to a constant heat flux are applied and remain at the constant value for the duration of analysis, illustrated above in Figure 33. The upper and lower bounds, along with FDS heat flux time history, are applied to the concrete surface for 300 seconds with a time step of one second. Comparisons of the temperature variation into the concrete liner are determined at two representative ceiling locations, (1) above fire and (2) 20 meters from fire are shown below in Figure 34, where dashed lines represent upper and lower bound flux histories and the solid lines represent the more complex FDS heat flux time history. The results are presented for the three fire cases and presented at three points in time, 50, 150 and 250 seconds.

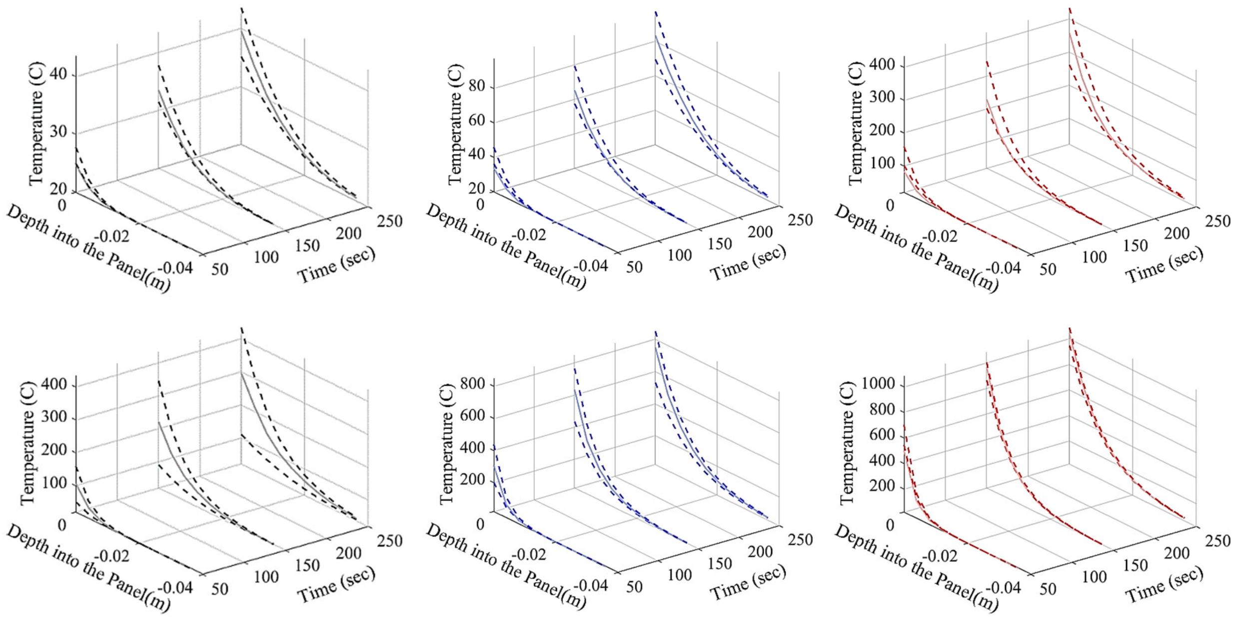

Figure 34 - Through-thickness temperature gradients above fire (top) and 20 meters from fire (bottom) for 30MW (left), 70MW (center) and 200MW (right) fires

The upper and lower bounds bracket the FDS solution of thermal gradients through the concrete section for the duration of the analysis. Subsequent FDS solutions will be presented utilizing these bounds, as they represent a holistic capture of the numerical solution. Results for the 30MW, 70MW, and 200MW with FDS upper and lower bounds, as well as the mean values from FDS after the 30 second ramp up time, are presented below in Figure 35, Figure 36, and Figure 37, respectively.

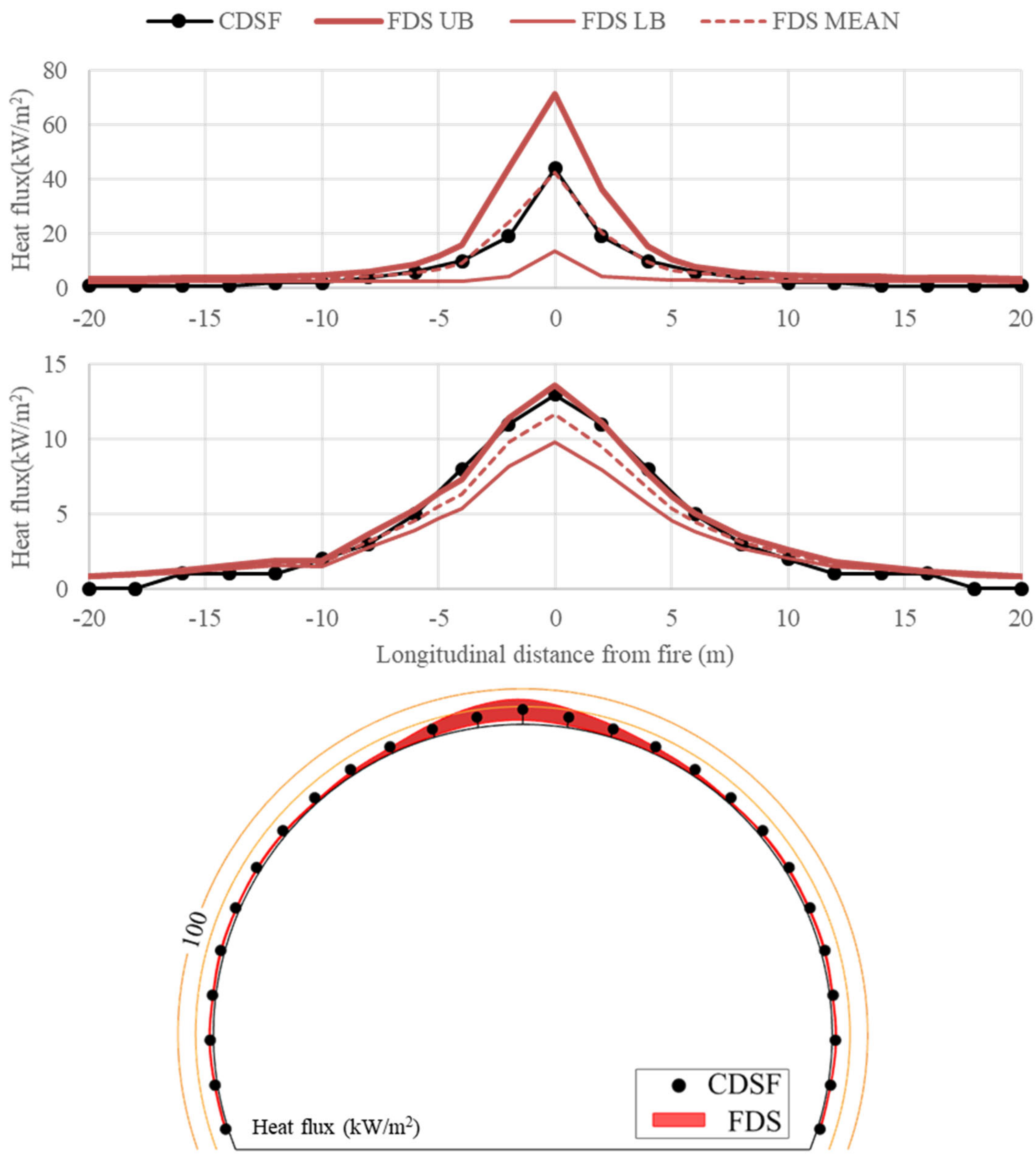

Figure 35 - Longitudinal (top) sidewall (center) and cross section (bottom) distribution of incident heat flux for 30MW fire

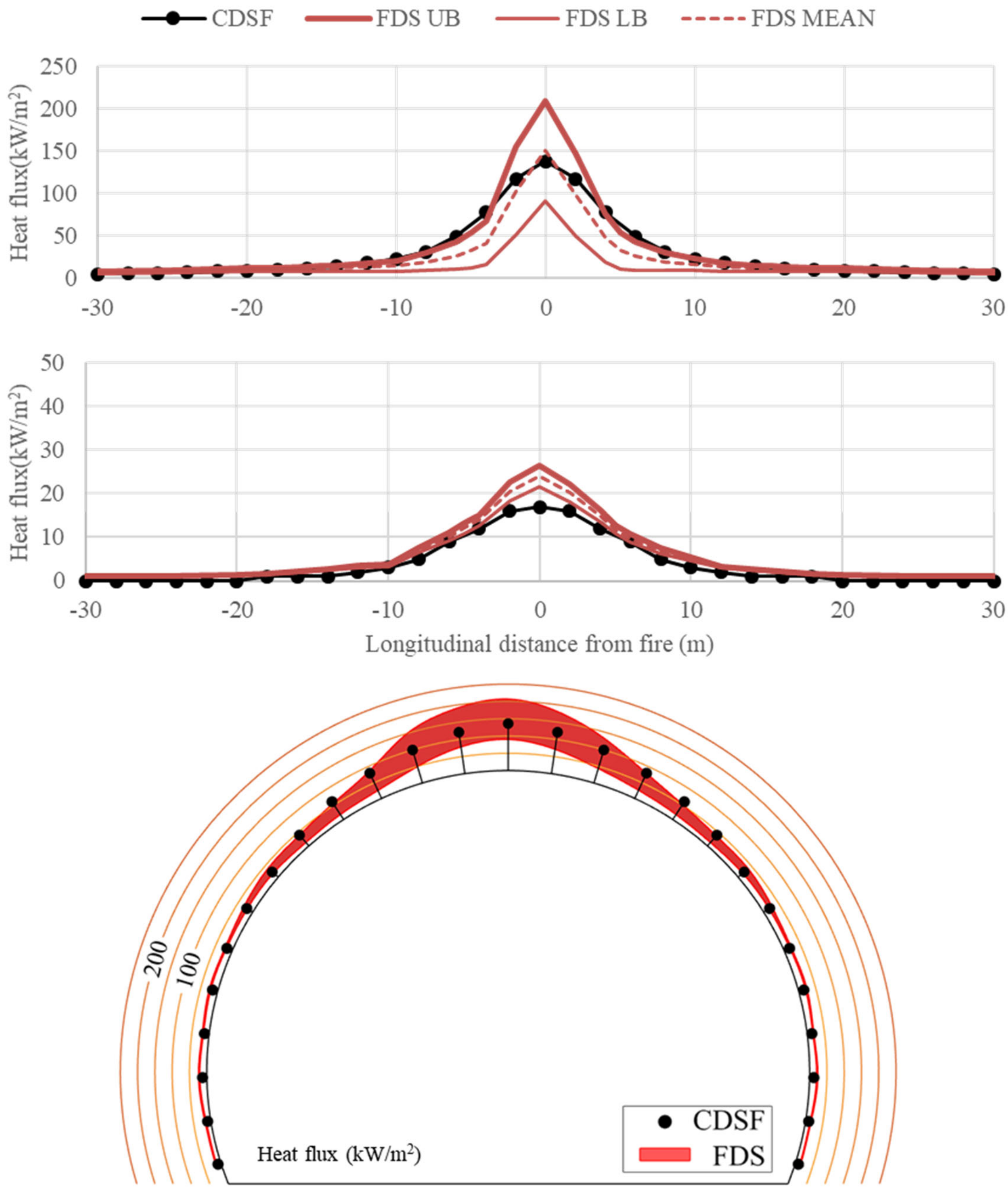

Figure 36 - Longitudinal (top) sidewall (center) and cross section (bottom) distribution of incident heat flux for 70MW fire

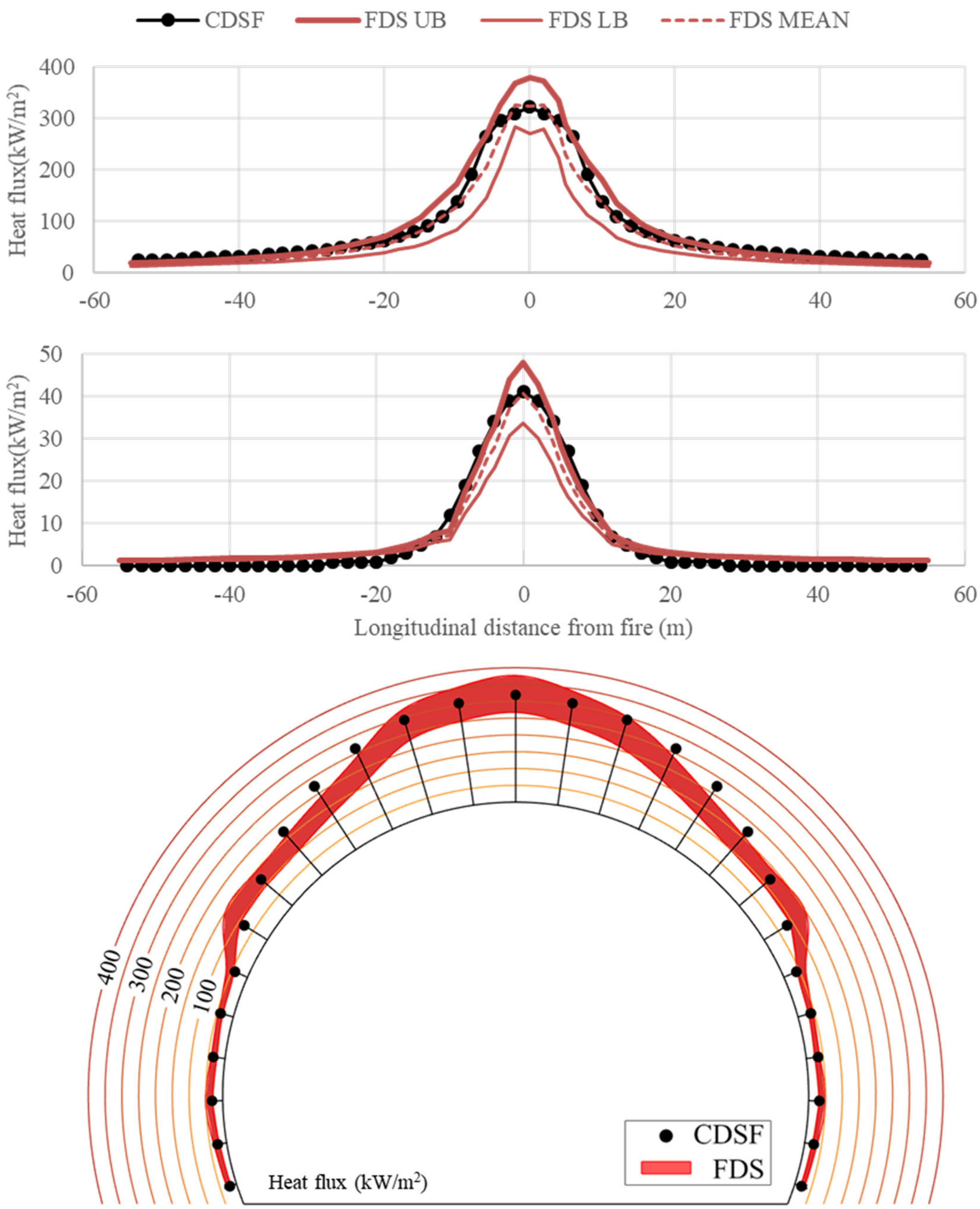

Figure 37 - Longitudinal (top) sidewall (center) and cross section (bottom) distribution of incident heat flux for 200MW fire

The FDS and CDSF solutions show excellent agreement across the three fire sizes through a broad range of incident heat fluxes. FDS solutions suggest the presence of a strong ceiling jet for both the 70MW and 200MW fire, where the heat flux distribution has a discontinuity in increase through the height of the cross section. This has been accurately captured with the CDSF. Analysis time for each CDSF solution is just under 4 minutes with the current mesh discretization having a maximum edge length of no more than 85 *cm*. The computational effort required for FDS to run the 200MW fire on an equivalent desktop workstation is around 15 hours, further proving the necessity of a model which is efficient and conservatively accurate.

Chapter 3: Blast Evaluation of Tunnels

This chapter provides an overview of a confined discretized solid flame model for examining blast effects on tunnel surfaces. This information has also been provided in paper published in the Transportation Research Record.

Bai, F., Guo, Q., Root, K.*, Naito, C., Quiel, S., "Blast Vulnerability Assessment of Road Tunnels with Reinforced Concrete Liners," Journal of the Transportation Research Board, Vol. 2672, No. 41, pp. 156-164, Sept. 2018, https://doi.org/10.1177/0361198118798458.*

Blast Evaluation of Tunnels

For blast evaluation, this report will focus on VBIED blast hazards and the associated spall and breach damage to the liner of common reinforced concrete tunnels. Detonation of explosive materials generate a rapidly expanding pressure wave that radiates spherically from the charge. These shock waves can generate a significant pressure impulse when they impact structural components in their path. This fast-moving load is termed reflected pressure and varies in magnitude and duration depending on the size of explosive, standoff distance, and the spatial orientation of the loaded component to the shock wave front. Blast demands are generally divided into contact, close-in, and far-field events. Far field events are generally assumed to occur at a scaled distance of greater than 5.0 ft/lb$^{1/3}$, where scaled distance is the standoff distance (in feet) divided by the cube root of the charge size (in lbs of TNT). Contact and close-in events occur at smaller scaled distances. The response of a reinforced concrete structural component under a far field blast demand is typically governed by flexural and shear response, while the response to a close-in event is controlled by shockwave propagation through the thickness of the component, thereby resulting in spalling, cracking, and breach. The pressure demand generates a compression wave through the concrete element that can spall the surface as the compression wave reflects off the back and/or front surfaces, causing the stress to exceed the tensile capacity. If the depth of spall approaches the wall thickness, a breached opening can be generated through the component. Tunnel liners are backed by the surrounding media and may experience an even more pronounced response to blast via shockwave propagation through liner thickness. Tunnel enclosures limit the available standoff and can result in reflection of the blast front such that each surface can experience multiple pressure impulses. Therefore, the primary concern for tunnel liners subject to blast loads is breach and spall damage.

To date, evaluations of the damage resulting from blast events have been conducted via either experimental studies or complex numerical modelling. Full scale blast events are very expensive to reproduce, and alternative means (such as scaled tests via small charges, shock tubes, or impact hammers) are often used to study their effects. (Colombo et al. 2016) Colombo et al. are often more focused on the development of new tunnel liner technologies rather than the evaluation of existing inventories.

Proposed Framework for Blast Damage Assessment

As mentioned previously, the damage typically associated with close-in blast in reinforced concrete tunnels are spall and breach. UFC 3-340-02 (Department of Defense (DoD) 2014) contains an empirical approach for estimating spall and breach in concrete based on comprehensive test data to predict damage of concrete slabs exposed to blast loads, as shown in Figure 38. The empirical equations below are valid for a wide range of data as shown in UFC 3-340-02 (Department of Defense (DoD) 2014):

$$\text{Spall Threshold: } \frac{h}{R} = \frac{1}{a + b\psi^{2.5} + c\psi^{0.5}} \tag{15}$$

$$\text{Breach Threshold: } \frac{h}{R} = \frac{1}{a + b\psi + c\psi^{2}} \tag{16}$$

where h = concrete thickness (ft); R = standoff from slab face to charge center of gravity (ft); and Ψ = spall parameter. In Equation 15, a = -0.02511; b = 0.01004; c = 0.13613; in Equation 16, a = 0.028205; b = 0.144308; c = 0.049265. For the non-contact and contact charges, the spall parameter Ψ are calculated from the following equations:

$$\text{Non-Contact Charges: } \psi = R^{0.926} f_c^{'0.266} W_{adj}^{-0.353} (W_{adj} / (W_{adj} + W_c))^{0.333} \tag{17}$$

$$\text{Contact Charges: } \psi = 0.527 R^{0.972} f_c^{'0.308} W_{adj}^{-0.341} \tag{18}$$

where f_c' = concrete compressive strength (psi); W_{adj} = adjusted charge weight (lb) = $B_f\, C_f\, W$; W_c = steel casing weight (lb); W = equivalent TNT charge weight (lb); B_f = burst configuration factor (1.0 for surface bursts, 0.5 for free air bursts); C_f = cylindrical charge factor, calculated as follows:

$$\text{For } L > D \text{ and } R/W^{0.333} < 2.0,\ C_f = 1.0 \tag{19}$$

$$\text{Else: } C_f = 1 + 2\left(LD / \left(\pi\left(3LD^2/16\right)^{0.667}\right) - 1\right)\left(1 - R / \left(2W^{0.333}\right)\right) \tag{20}$$

where L = charge length; D = charge diameter. Dynamic strength increase due to strain rate effect was included in the expression of Ψ (Department of Defense (DoD) 2014), which enhanced the model's applicability to full-scale explosion. The applicability of the model is limited to the range of test data used as summarized in Table 4. In these equations, W_{adj} is the weight of a hemispherical surface charge that applies an explosive impulse at the target equal to that of the actual charge.

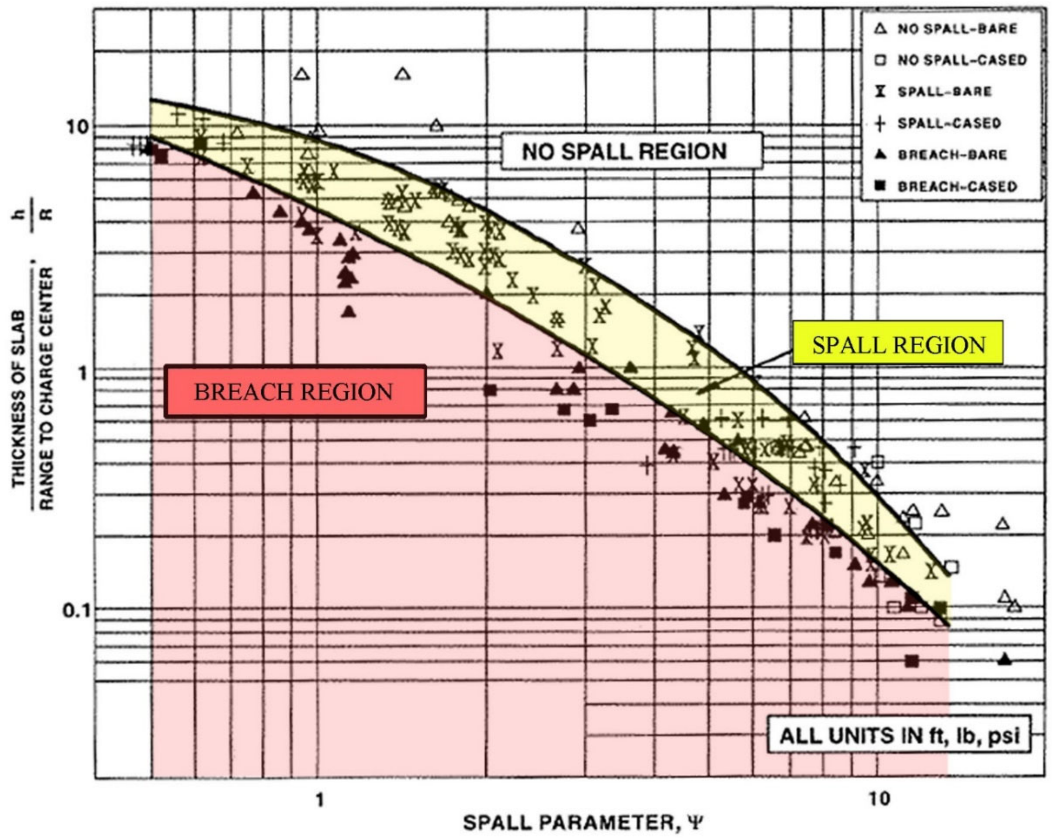

Figure 38 - Spall and breach curves and supporting test data from Fig. 4-65a, UFC 3-340-02 (Department of Defense (DoD) 2014)

Table 4 – Parametric ranges for spall prediction from Tab. 4-15a, UFC 3-340-02

Parameter	Max.	Min.	Avg.
R, in	360	0.1	21.0
Charge weight, W, lb	2299	0.03	24.4
Case length, in	60.0	0.80	8.8
Case diameter, in	18.0	0.80	4.0
Case thickness, in	0.62	0.00	0.05
$R/W^{1/3}$, $in/lb^{1/3}$	12.1	0.008	0.70
Concrete thickness, T, in	84.0	2.00	9.23
f_c', psi	13815	1535	5067

Breach and spall thresholds are applied to a tunnel geometry as spheres with radii explicitly solved from Equation 15. The intersection of these spheres with the tunnel denote the extent of breach and spall damage. For this study, a parametric CAD environment (Robert McNeel & Associates 2017) (Robert McNeel & Associates 2014) is used to generate an extruded cross section of the representative tunnel geometry and analyze its intersection with the blast-induced damage spheres (yellow for breach and red for spall), as demonstrated in Figure 39. This approach has also been implemented via Matlab (The Mathworks Inc. 2016), which is more conducive to a parametric study of a range of threats or tunnel geometries.

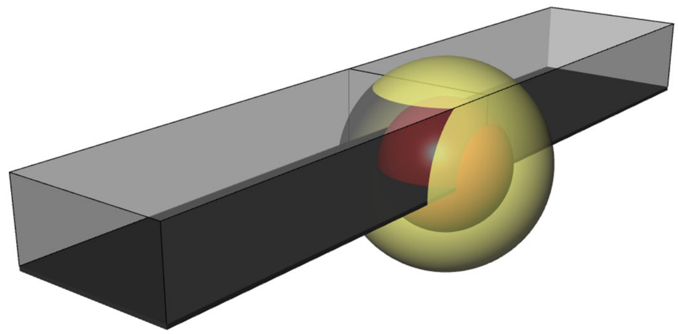

Figure 39 - Spherical damage mapping due to blast in a rectangular tunnel

Tunnel Prototypes

To demonstrate the proposed approach, three tunnel geometries are considered as representative examples in the current US tunnel inventory: rectangular, horseshoe, and circular. Each tunnel is designed for two lanes of traffic moving in the same direction. Lane width and shoulder size vary in all three tunnels. Cross-sectional details and typical threat locations are shown in Figure 40. The cross-sectional openings and wall thicknesses are typical of these tunnel types in practice. The horseshoe and circular liner thicknesses are scaled to approximately 22 times the effective diameter of the tunnel opening (based on the cross-sectional area). The rectangular tunnel liner thickness is also based on the effective diameter-opening approach but is further increased to account for the additional bending action. These systems are examined for detonation of an explosive charge within the tunnel at the center of the right lane, as shown in Figure 40. Reduction in pressure demands at the entry/exit and damage to the end portals are not considered.

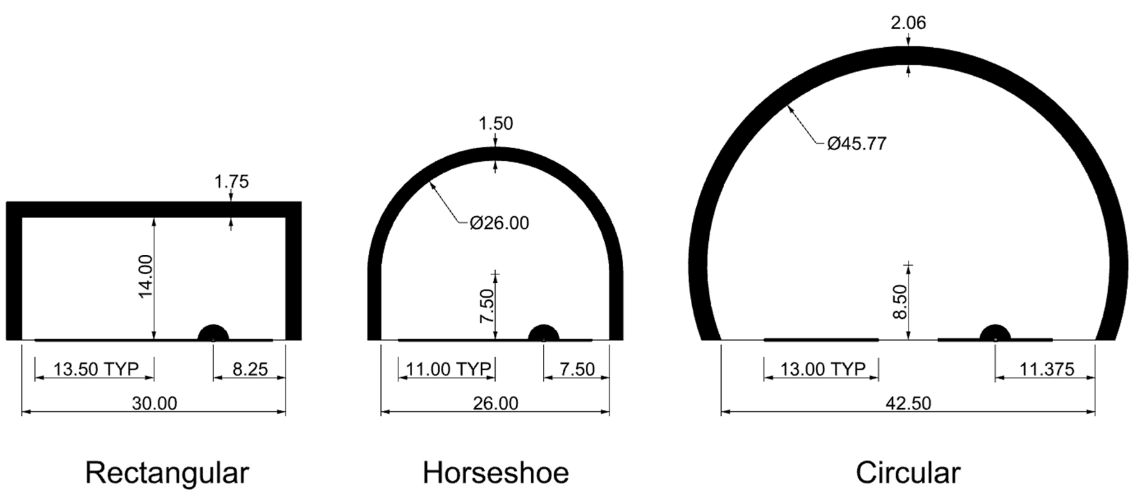

Figure 40 - Tunnel geometries and details (all dimensions in feet = 0.3048 m)

FEMA 426 (Federal Emergency Management Agency (FEMA) 2003) specifies a range of design values for vehicle threats (ranging from sedans to vans and light cargo trucks) from 500 to

4000 lbs of TNT. Three charge weights of 500, 1000 and 2000 lbs of TNT (labeled A, B and C, respectively) were chosen to conform both to the FEMA hazard scale as well as the charge sizes within the parametric range of damage predictions shown in Table 4 from UFC 3-340-02. These threat sizes are also similar to those selected in previous studies of blast effects in tunnels (Choi et al. 2006).

Because of the uncertainty of the vehicle size and to avoid the implications associated with air burst (such as Mach stem and complex reflection), it is conservatively assumed for this study that the charges will be located on the road surface ($B_f = 1.0$). The yellow hemispheres in Figure 41 indicate the charge location in the center of the right lane as shown in Figure 40. Future analyses will capture varying threat elevations to account for different vehicle heights and delivery methods. Breached areas are removed from the tunnel geometry, while areas outside the breach radius yet still affected by spalling are represented in red. Road surfaces are shown strictly for clarity – only damage to the tunnel walls are considered within this visualization. Crater formation at the road surface and blast effects on tunnel lining below the road surface will be investigated in future work.

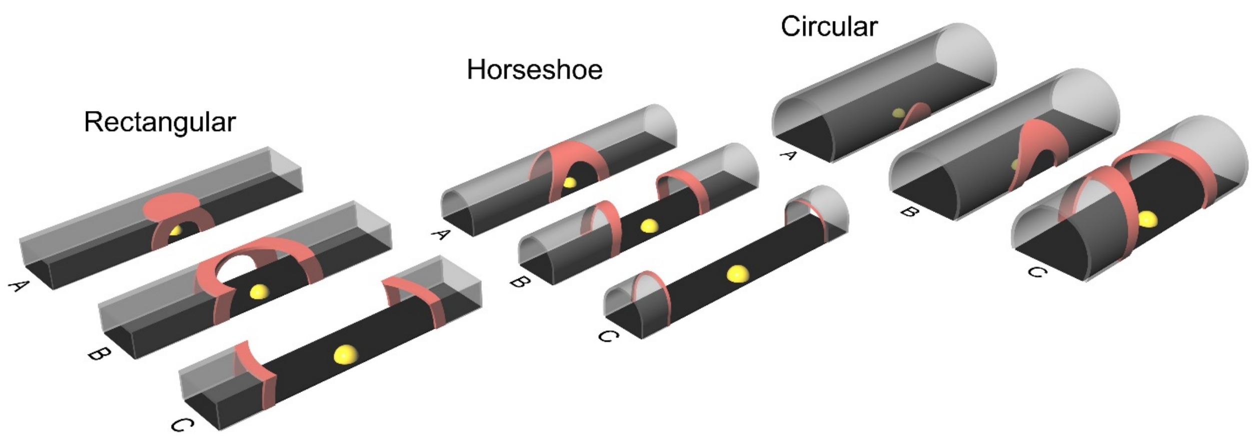

Figure 41 - Tunnel spall and breach damage for threats A, B and C

As shown from Figure 41, the circular tunnel exhibits the least damage among the three when exposed to threats A and B, while the rectangular and horseshoe tunnel experienced significant breach of their liner when exposed to the same threat levels. A summary of affected areas and threat size for each tunnel is tabulated in Figure 42. Both the rectangular and horseshoe tunnels experience breach at all threat levels as well as a total loss of cross-section at the larger threats – in these cases, a cave-in of the surrounding media would be highly likely. Damage cases in which up to half of the cross-section is lost would be candidates for progressive collapse evaluation to prevent a chain reaction toward total loss of cross-section. Though all three tunnels have the same throughput, the circular tunnel suffered significantly less damage due to a larger standoff distance from the charge as shown in Figure 40.

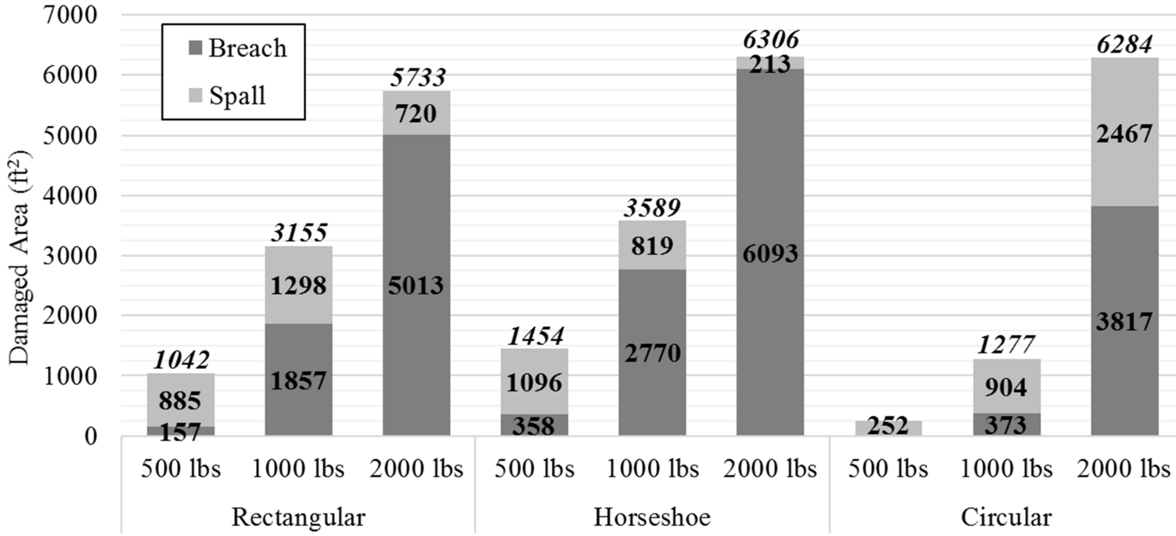

Figure 42 - Summary of spall and breach experienced by each tunnel type for each blast threat

Comparison to Computational Models

As verification, high-fidelity analysis results from LS-DYNA (LSTC 2018) are compared with the rectangular tunnel performance in Figure 40. The explosive threats are assumed to be located on the ground (i.e. as a surface charge) to eliminate the influence of partial reflection (Mach Stem) if the charge were elevated in a vehicle. The blast effects resulting from the surface charge assumption are conservative and produce an upper bound of response. The Multi-Material Arbitrary Lagrangian Eulerian method is chosen in LS-DYNA to simulate the blast event. Concrete is modeled with Lagrangian solid elements with an approximate discretization dimension of 4 inches. The tunnel liner is modeled with 5 solid elements through its thickness, and about one million total solid elements are used to model a 50-foot length of the tunnel. The outside of the tunnel is approximated as a rigid boundary. This assumption provides a conservative evaluation of damage by ensuring maximum energy reflected back into the liner and therefore providing an upper bound for blast damage. In reality, the surrounding media will absorb some of the pressure shock depending on its stiffness – this energy dissipation is neglected in this analysis but will be explored in future work. A real tunnel system will interact with its backfill substrates, potential groundwater, and unstable sediment and/or rock formations. Variation in the surrounding media can affect the response of the liner to blast depending on the longitudinal location of the threat – critical locations could then be identified and prioritized for hardening.

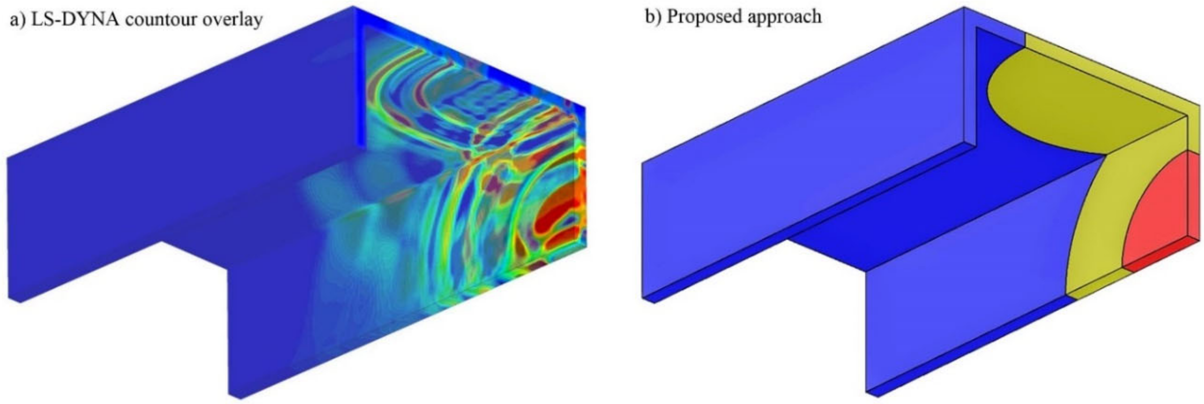

Figure 43-Comparison of spall and breach damage contours from (a) computational (LS-DYNA) analysis and (b) the proposed approach for the rectangular tunnel subjected to the 500-lb threat

The concrete material behavior is approximated as linear elastic with an elastic modulus of 3600 ksi (approximately corresponding to a compressive strength of 4000 psi). Since the damage response is governed by shock wave propagation and associated tensile concrete failure through the liner thickness, the steel reinforcement is neglected in the current analyses. Future research will explore the effect of concrete material nonlinearity and the placement of steel reinforcement. Symmetry about the charge location is used to decrease the computational expense. The explosive charge is modeled with material type 8 in LS-DYNA, namely, *MAT_HIGH_EXPLOSIVE_BURN. The JWL equation of state is used to link the explosive reaction to the air volume elements. Both the charge and air domains are constructed with solid elements.

The 500-lb charge is used here as a demonstration to compare the proposed approach with the computational analysis. The analysis in LS-DYNA takes approximately 4 hours to analyze 3 milliseconds of the close-in blast (which captures the peak exposure) when performed on a modern desktop computer with i7 quad core processor, 16GB of RAM, and solid state hard drive. Using the same hardware, the proposed approach takes approximately 10 seconds to analyze the same tunnel segment. Figure 43 compares the results of the computational model and the proposed approach. The contour in Figure 43(a) represents an overlay of maximum principle tensile stresses on the interior face of the tunnel liner – red shaded areas indicate that the tensile stresses have reached the concrete’s tensile capacity (taken as 316 psi). Breach is indicated at regions where the tensile capacity has been reached through the liner thickness during the analysis. Spalled regions have reached the tensile capacity only on the interior face due to thru-thickness shock propagation.

Figure 43 shows good agreement of the spatial distribution of damage between the LS-DYNA analysis and the proposed approach. The overall areas of spall and breach damage are within 10% of each other, with the computational model indicating slightly more breach and the proposed approach slightly more spall. This variation will be investigated in future work and is most likely caused by the pressure variability in the computational model due to confinement and reflection of the shock wave. The proposed approach will be modified to incorporate these effects in future studies.

Parametric Study

Due to its computational efficiency, the proposed approach readily allows for parametric variation of the tunnel geometry and rapid determination of damaged regions for a given threat. In this way, tunnels with non-uniform cross sections and/or cross passageways could be quickly assessed with the same framework. This approach provides two important tools to the designer. First, the area contour of damage can be quantified for a given threat. The damaged zone can then be used as the input to a progressive collapse assessment of the tunnel liner. Second, the approach can be used to examine a range of threats and assess the correlation of damage increase with increases in blast intensity.

Typical relationships between damage and demand (i.e., breach/spall area versus charge size) are illustrated in Figure 44. In scenario 1, damage increases very quickly at low threat levels but slows down considerably at point A. For this scenario, the system should be designed for the damage level and threat intensity at A as a minimum. Scenarios 2 and 3 are similar, and both have a critical point B, in which the gradient decreases and damage starts to increase with small changes in threat size. Then at point C and D, the rate of damage decreases. Thus, for the range B-C and B-D for scenarios 2 and 3, the ending points C and D could be considered as the optimal level to achieve a conservative and effective design.

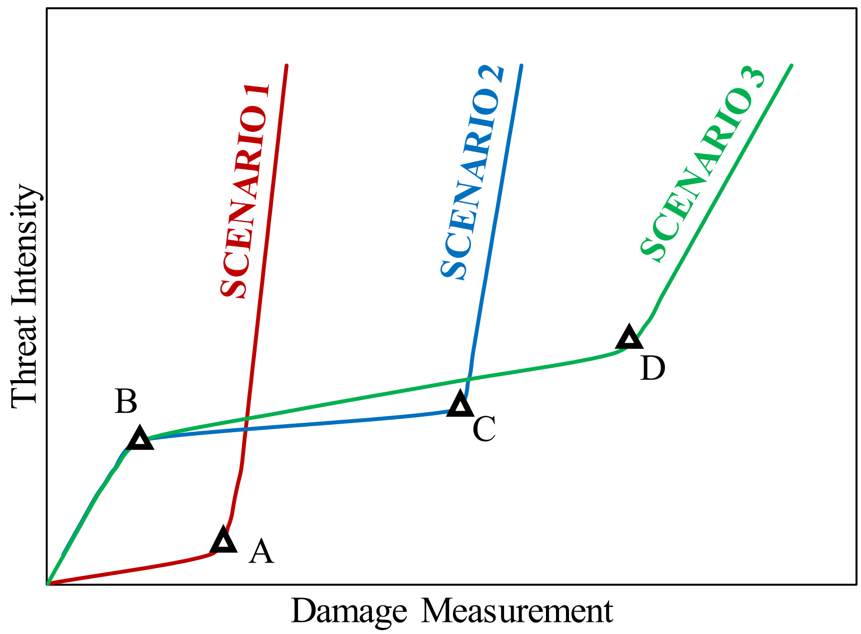

Figure 44 - Typical damage vs charge relation

This design recommendation is implemented in Figure 45 for the three tunnels. The solid curves in Figure 45 show the relationship between charge weight and damaged area for rectangular, horseshoe and circular tunnels. The dotted line in each plot represents the gradient or slope of the threat-to-damage relationship. For all the three tunnels, the TNT weight was progressively increased from 200 lbs to 2300 lbs of TNT, which is the maximum value in the valid range of the empirical model in UFC 3-340-02 (see Table 4).

Table 5 – Tunnel performance and retrofit requirements for the 1000-lb threat

Tunnel type	Design/Retrofit	Wall Thickness (ft)*	Total Damaged Area (ft^2)*	Breaching Area (ft^2)

Rectangular Tunnel	Design	1.75	3155	1857
	Retrofit	3.47	837	0
Horseshoe Tunnel	Design	1.50	3689	2770
	Retrofit	3.64	467	0
Circular Tunnel	Design	2.06	1277	373
	Retrofit	2.90	534	0
* 1 ft = 0.3048 m, 1ft^2 = 0.092 m^2				

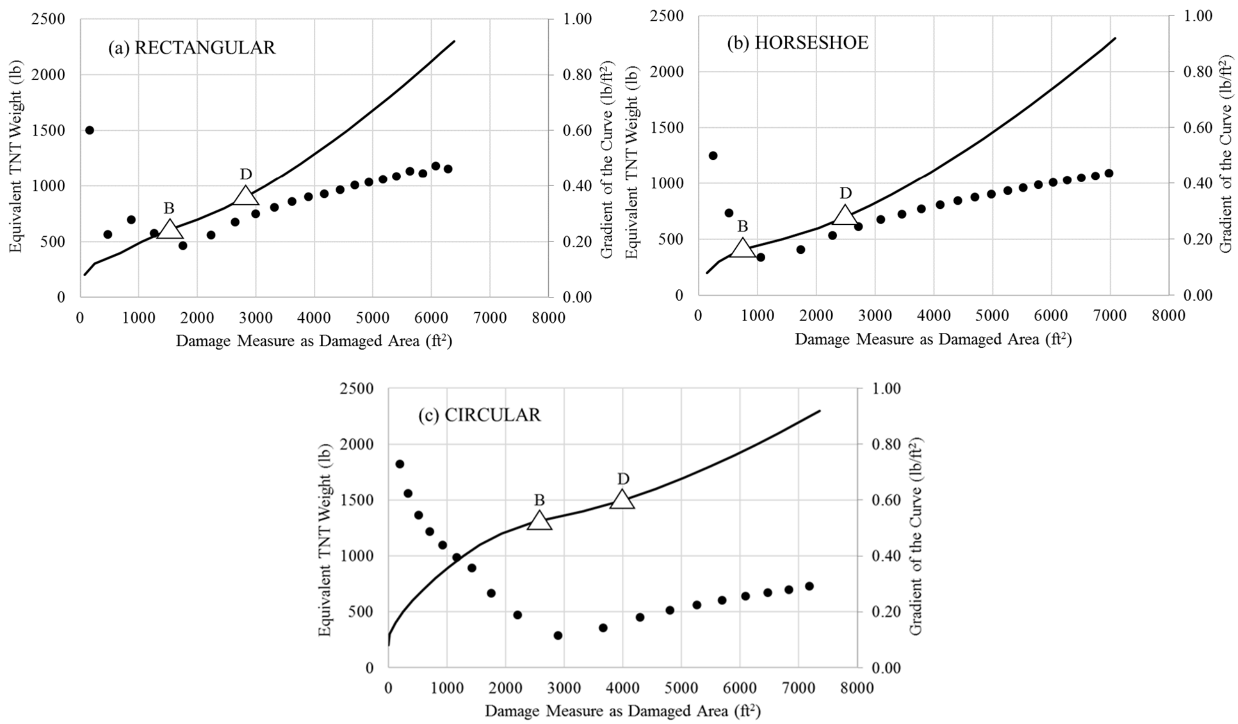

Figure 45 - Damage area (spall + breach) versus charge weight for each tunnel

According to the dotted line for the rectangular tunnel in Figure 45(a), the gradient initially reduces with increasing blast load, reaching the minimum at approximately 500 lbs and then increasing again at about 900 lbs. According to the schematic plot in Figure 7, the damage vs charge relation resembles scenario 3. Point B corresponds to the gradient value just before its minimum. Point D corresponds to the subsequent gradient value after which the tangential slope of the gradient line demonstrably decreases. For the rectangular tunnel, Point D at 900 lbs could be an optimal value for design because the damage increases more significantly for a modest increase in threat size up to this point. This is consistent with the results shown in Figures 4 and 5, which indicated significant increases in breach area as the threat is increased from 500 to 1000 lbs. The horseshoe and circular tunnels show similar behavior to that of the rectangular tunnel, with a more pronounced change of gradient beyond point D. The critical TNT weight range at which most of the cross-section breaches is approximately 400 - 700 lbs for the horseshoe tunnel and 1300 - 1500 lbs for the circular tunnel, which are marked in Figure 45(b) and (c) between points B and D. The hazard level at point D could be used to establish the initial conditions for progressive collapse evaluation of the tunnel. Up to this point, enough of the cross-section remains such that an evaluation of the damaged liner to resist subsequent progressive collapse could be warranted and effective. Threat sizes beyond this point will rapidly increase the damage as the cross-section circumference becomes completely breached and a subsequent cave-in becomes likely.

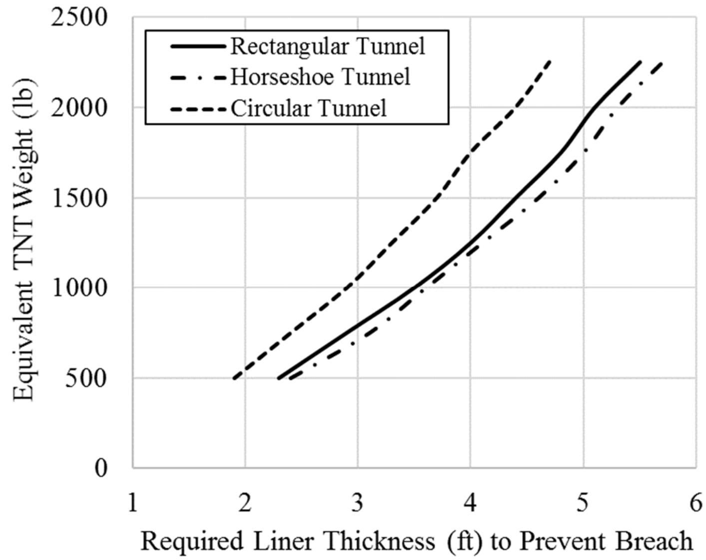

Figure 46 - Tunnel liner thicknesses needed to prevent breach

To avoid breach, the wall thickness can be modified through various means, including but not limited to shotcrete or precast concrete panels. As a simple illustration in Table 5, the horseshoe and rectangular systems wall thickness can be increased to 3.63 ft and 3.47 ft, respectively, to eliminate the occurrence of breach under the 1000 lbs VBIED, though spalling will still occur. This approach can be extended to any charge size and tunnel geometry to provide the owner with a means to estimate a target level of design performance. As an example, the liner thickness needed to eliminate breaching is plotted for each tunnel geometry for increasing charge size in Figure 9. The results show that for standard VBIED sizes, it is possible to mitigate breach damage via increases in wall thickness.

Chapter 4: Summary and Conclusions

Summary

To assess fire demands, the development and verification of a confined discretized solid flame model (CDSF) has been presented. Demonstrative verification of the model with a coarse discretization has proven the architecture of the CDSF to be reliable. An evaluation of three fire sizes in a circular tunnel has demonstrated the accuracy of the model amongst a range of large-scale fires.

A simplified analysis approach for predicting blast-induced damage is presented, with high-fidelity numerical modeling used as verification. The numerical model is developed to conservatively evaluate the maximum blast damage. The backfill/substrate properties are assumed "rigid" so that the shock wave propagation energy is conserved and reflected back into the concrete lining. The explosive threats are assumed to be located on the ground (i.e. as a surface charge) to eliminate the influence of partial reflection if the charge were elevated in a vehicle. The blast effects resulting from the surface charge assumption are conservative and produce an upper bound of response. An examination of tunnel vulnerability to blast was conducted for three prototype tunnel systems subjected to a range of blast load intensities.

Conclusions

The CDSF allows for total mapping and visualization of the incident heat flux distribution on a tunnel structure at a fraction of the analysis time required by computational fluid dynamics solutions. The application of the CDSF presented here is currently limited to one tunnel shape and size; however, the framework of the model can be subsequently adapted to capture a broader range of tunnel geometries and fire sizes. In the Grasshopper-Rhino environment, the framework is visually represented and the geometric evolution of flame shape and tunnel-flame interaction can be seen firsthand. This level of control and visual feedback allows for the development of complex geometry which would be difficult with conventional programming solutions.

Empirical equations in UFC 3-340-02 can reasonably predict the upper bound of concrete liner breach and spall results under blast loads. This approach is highly efficient, and the results are comparable to numerical models; however, the approach relies on several conservative assumptions and should be considered as an upper bound for damage prediction. Three existing tunnels and three charge weights are analyzed. As expected, the results show that the spall and breach damage is correlated to standoff distance for a specific charge weight. The results also indicate that a moderately sized VBIED can produce a significant amount of breaching in a tunnel system. The approach can be readily implemented to estimate the amount of retrofit needed to mitigate damage under a specific threat, and it can also be used to determine the minimum recommended design threats based on the gradient of the threat-to-damage relationship. Inflection points in this relationship can be used to identify hazard levels at which a progressive collapse evaluation would be warranted.

Future work

Future work will focus on extending the range of applicability of the CDSF to not only curved tunnels but to rectangular tunnel cross-sections as well. It should also be noted that while the CDSF has been developed with tunnel applications in mind, the principles and architecture of the model can be adapted to an array of confined spaces.

Tunnel damage under blast is a developing topic, and a reliable, efficient methodology is needed for engineering design and analysis. Future efforts will include developing improved analytical approaches for increasingly accurate and efficient predictions. Also, the coupled effect between blast and fire requires attention and should be addressed in a future study.

References

American Association of State Highway and Transportation Officials (Ed.). (2001). *A policy on geometric design of highways and streets, 2001*. American Association of State Highway and Transportation Officials, Washington, D.C.

Association, N. F. P. (2011). *NFPA 502, Standard for road tunnels, bridges, and other limited access highways*. NFPA.

Babrauskas, V. (2016). "Heat Release Rates." *SFPE handbook of fire protection engineering*, Springer, 799–904.

Bai, F., Guo, Q., Root, K., Naito, C., and Quiel, S. (2018). "Blast Vulnerability Assessment of Road Tunnels with Reinforced Concrete Liners." *Transportation Research Record*, 2672(41), 156–164.

Buonsanti, M., and Leonardi, G. (2013). "3-D simulation of tunnel structures under blast loading." *Archives of Civil and Mechanical Engineering*, Elsevier, 13(1), 128–134.

Carvel, R. (2004). "Fire Size in Tunnels." Heriot-Watt University, School of the Built Environment Division of Civil Engineering.

CEN. (2008). *EN 1992-1-2: Eurocode 2: Design of concrete structures - Part 1-2: General rules - Structural fire design*. European Commission for Standardization, Brussels, Belgium.

Choi, S., Wang, J., Munfakh, G., and Dwyre, E. (2006). "3D Nonlinear Blast Model Analysis for Underground Structures." *GeoCongress 2006*, 1–6.

CNN. (2017). "St. Petersburg metro explosion: At least 11 dead in Russia blast." *CNN*, <https://www.cnn.com/2017/04/03/europe/st-petersburg-russia-explosion/index.html> (Feb. 25, 2020).

Colombo, M., Martinelli, P., and di Prisco, M. (2016). "On the blast resistance of high performance tunnel segments." *Materials and Structures*, 49(1), 117–131.

Department of Defense (DoD). (2014). *UFC 3-340-02 Unified Facilities Criteria: Structures to Resist the Effects of Accidental Explosions*. Washington, D.C.

Edri, I., Savir, Z., Feldgun, V., Karinski, Y., and Yankelevsky, D. (2011). "On Blast Pressure Analysis Due to a Partially Confined Explosion: I. Experimental Studies." *International Journal of Protective Structures*, 2(1), 1–20.

Federal Emergency Management Agency (FEMA). (2003). *FEMA 426 - Reference Manual to Mitigate Potential Terrorist Attacks Against Buildings*.

Feldgun, V. R., Kochetkov, A. V., Karinski, Y. S., and Yankelevsky, D. Z. (2008). "Internal blast loading in a buried lined tunnel." *International Journal of Impact Engineering*, 35(3), 172–183.

Franssen, J.-M., and Gernay, T. (2017). "Modeling structures in fire with SAFIR®: Theoretical background and capabilities." *Journal of Structural Fire Engineering*, 8(3), 300–323.

Gombeda, M. J., Naito, C. J., Quiel, S. E., and Fallon, C. T. (2017). "Blast-Induced Damage Mapping Framework for Use in Threat-Dependent Progressive Collapse Assessment of Building Frames." *Journal of Performance of Constructed Facilities*, 31(2), 04016089.

Hu, L. H., Huo, R., Chow, W. K., Wang, H. B., and Yang, R. X. (2004). "DECAY OF BUOYANT SMOKE LAYER TEMPERATURE ALONG THE LONGITUDINAL DIRECTION IN TUNNEL FIRES." *Journal of Applied Fire Science*, 13(1), 53–77.

Hurley, M. J., Gottuk, D., Hall, J. R., Harada, K., Kuligowski, E., Puchovsky, M., Torero, J., Watts, J. M., and Wieczorek, C. (Eds.). (2016). *SFPE Handbook of Fire Protection Engineering*. Springer New York, New York, NY.

Kurioka, H., Oka, Y., Satoh, H., and Sugawa, O. (2003). “Fire properties in near field of square fire source with longitudinal ventilation in tunnels.” *Fire Safety Journal*, 38(4), 319–340.
Le, Q. X., Dao, V. T. N., Maluk, C., Torero, J., and Bisby, L. (2016). “An investigation into temperature gradient effects on concrete performance at elevated temperatures.” *The 24th Australasian Conference on the Mechanics of Structures and Materials (ACMSM24)*.
LSTC. (2018). *LS-DYNA*. Livermore Software Technology Corporation (LSTC), Livermore, CA.
McGrattan, K. B., Baum, H. R., and Hamins, A. (2000). *Thermal radiation from large pool fires*. National Institute of Standards and Technology, Gaithersburg, MD.
McGrattan, K. B., McDermott, R. J., Weinschenk, C. G., and Forney, G. P. (2013). “Fire Dynamics Simulator, Technical Reference Guide, Sixth Edition.” *Special Publication (NIST SP) - 1018*.
Miller, E. (2016). *Terrorist Attacks Targeting Critical Infrastructure in the United States, 1970-2015*. National Consortium for the Study of Terrorism and Responses to Terrorism.
Muñoz, M., Planas, E., Ferrero, F., and Casal, J. (2007). “Predicting the emissive power of hydrocarbon pool fires.” *Journal of Hazardous Materials*, 144(3), 725–729.
NFPA. (2017). *NFPA 502: Standard for road tunnels, bridges, and other limited access highways*. National Fire Protection Association, Quincy, MA.
Pennetier, O., William-Louis, M., and Langlet, A. (2015). “Numerical and reduced-scale experimental investigation of blast wave shape in underground transportation infrastructure.” *Process Safety and Environmental Protection*, Institution of Chemical Engineers, 94(C), 96–104.
Quiel, S. E., Yokoyama, T., Bregman, L. S., Mueller, K. A., and Marjanishvili, S. M. (2015). “A streamlined framework for calculating the response of steel-supported bridges to open-air tanker truck fires.” *Fire Safety Journal*, 73, 63–75.
Robert McNeel & Associates. (2014). *Grasshopper*.
Robert McNeel & Associates. (2017). *Rhinoceros*.
Root, K., Guo, Q., Quiel, S., and Naito, C. J. (2018). “Calculating Fire-Induced Heat Flux Contours on Concrete Tunnel Liners to Evaluate Structural Consequences.” *10th International Conference on Structures in Fire: Structures in Fire*, Ulster University, Belfast, UK, 17–24.
Siddapureddy, S. (2013). “Characterization of Open Pool Fires and Study of Heat Transfer in Bodies Engulfed in Pool Fires.” Indian Institute of Technology Dharwad.
Stewart, M. G., Netherton, M. D., and Rosowsky, D. V. (2006). “Terrorism risks and blast damage to built infrastructure.” *Natural Hazards Review*, 7(3), 114–122.
Stolz, A., and Ruiz-Ripoll, M. L. (2016). “Experimental and Computational Characterization of Dynamic Loading and Structural Resistance of Tunnels in Blast Scenarios.” *Fire Technology*, Springer US, 52(5), 1595–1618.
“The Boring Company.” (2020). *The Boring Company*, <https://www.boringcompany.com> (Apr. 24, 2020).
The Mathworks Inc. (2016). “MATLAB - MathWorks.” *www.mathworks.com/products/matlab*, <http://www.mathworks.com/products/matlab/>.
The White House Office of the Press Secretary. (2013). *Presidential Policy Directive -- Critical Infrastructure Security and Resilience*.
Transportation Research Board. (2006). *TCRP Report 86/NVHRP Report 525: Public transportation security*. Transportation Research Board og the National Academics, Washington, D.C.

Uystepruyst, D., and Monnoyer, F. (2014). “A numerical study of the evolution of the blast wave shape in rectangular tunnels.” *Journal of Loss Prevention in the Process Industries*, Elsevier Ltd, 34, 225–231.

Wang, Y., Vouros, A., Zhang, J., and Delichatsios, M. A. (2017). “Numerical and experimental validation study of flame extent of a pool fire under the ceiling.” *Journal of Loss Prevention in the Process Industries*, 49, 652–659.

Zhou, K., Liu, N., Zhang, L., and Satoh, K. (2014). “Thermal Radiation from Fire Whirls: Revised Solid Flame Model.” *Fire Technology*, 50(6), 1573–1587.

Appendix A: Technology Transfer Activities

1 Accomplishments

1.1 What was done? What was learned?

- The development and verification of a confined discretized solid flame model (CDSF) has been presented for fire demands.
- An evaluation of three fire sizes in a circular tunnel has proven accuracy of the model amongst a range of large-scale fires.
- Demonstrative verification of the model with a coarse discretization has proven the architecture of the CDSF to be reliable.
- A simplified analysis approach for predicting blast-induced damage is presented, and numerical modeling is used as verification. An examination of tunnel vulnerability to blast was conducted for three prototype tunnel systems subjected to three blast load intensities.
- A moderately sized VBIED can produce a significant amount of breaching in a tunnel system.
- Empirical equations in UFC 3-340-02 can reasonably predict the upper bound of concrete liner breach and spall damage under blast loads, but they rely on several conservative assumptions and should be considered as an upper bound for damage prediction.
- The approach for blast-induced damage assessment can be readily implemented to estimate the amount of retrofit needed to mitigate damage under a specific threat, and it can also be used to determine the minimum recommended design threats based on the gradient of the threat-to-damage relationship.

1.2 How have the results been disseminated?

- The results were presented multiple times at different meetings and workshops from 2017 to 2019, including TRB Annual Meeting twice, UTC-UTI Workshop once, UTC-UTI Meeting twice, AFF60 Meeting once, NRC-CNRC International Workshop once, and other occasions multiple times.
- Two journal papers and one conference paper have been published based on the result, which include Fire Safety Journal, Transportation Research Record, and conference paper of 10th International Conference on Structures in Fire: Structures in Fire.

2 Participants and Collaborating Organizations

Name: Lehigh University

Location: Bethlehem, PA

Contribution: 1) A proposed approach is developed which allows for rapid assessment of thermal demands using models that are validated and informed through computationally intensive numerical assessment, experimental data, and semi-empirical relationships based on first principles. 2) A literature review of existing studies is conducted, and potential scenarios of blast events are examined with varying charge position and size. 3) An efficient analytical approach to determine the spatial distribution of blast-induced spall and breach damage is presented.

3 Outputs

Publications

- Root, K., Guo, Q., Quiel, S., and Naito, C. J. (2018). “Calculating Fire-Induced Heat Flux Contours on Concrete Tunnel Liners to Evaluate Structural Consequences.” 10th International Conference on Structures in Fire: Structures in Fire, Ulster University, Belfast, UK, 17–24.
- Guo, Q., Root, K. J., Carlton, A., Quiel, S. E., and Naito, C. J. (2019). “Framework for rapid prediction of fire-induced heat flux on concrete tunnel liners with curved ceilings.” Fire Safety Journal, 109, 102866.
- Bai, F., Guo, Q., Root, K., Naito, C., and Quiel, S. (2018). “Blast Vulnerability Assessment of Road Tunnels with Reinforced Concrete Liners.” Transportation Research Record, SAGE Publications Inc., 2672(41), 156–164.

Presentations

- TRB 97th Annual Meeting, Blast Vulnerability Assessment of Road Tunnels with Reinforced Concrete Liners, Washington, D.C., January 10, 2018.
- First UTC-UTI Workshop, Tunnel Blast Evaluation and Damage Mapping, Colorado School of Mines, Golden, CO, February 19, 2017.
- First UTC-UTI Workshop, Experimental and Numerical Evaluation for Fire Damage Mapping in Concrete Tunnel Liners, Colorado School of Mines, Golden, CO, February 19, 2017.
- PennDOT Pitt Visit 2018, Streamlined Calculation of Fire-Induced Heat Flux and Resulting Spalling Damage for Concrete Tunnel Liners, August 7, 2018.
- Master Thesis Presentation, A Confined Discretized Solid Flame Model for Calculating Incident Heat Flux on Concrete Tunnel Liners, Lehigh University, Bethlehem, PA, August 23, 2018.
- AFF60 Meeting, Tunnel Liner Damage due to Fire and Blast: Fast-Running Predictions & Upcoming Test Programs, October 11, 2018.
- UTC-UTI Meeting, Tunnel Liner Damage due to Blast and Fire: Fast-Running Predictions and Upcoming Test Programs, Colorado School of Mines, Golden, CO, October 18, 2018.
- TRB 98th Annual Meeting, Assessing and Improving the Resilience of Highway and Rail Tunnels to Fire and Blast, Washington, D.C., January 13, 2019.
- NRC-CNRC International Workshop on Protection of Critical Infrastructure against Close-By and Attached Explosions, Performance of Transportation Tunnels Subject to Close-in Detonations, Ottawa, Canada, March 28-29, 2019.

Workshops

- Kyle Root, Qi Guo, Spencer Quiel, Clay Naito, First UTC-UTI Workshop, Colorado School of Mines, Golden, CO, February 19, 2017.
- Kyle Root, Qi Guo, UTC-UTI Meeting, Colorado School of Mines, Golden, CO, October 18, 2018.
- Clay Naito, NRC-CNRC International Workshop on Protection of Critical Infrastructure against Close-By and Attached Explosions, Canada, March 28-29, 2019.

4 Outcomes

- The allows for rapid assessment of thermal demands using models that are validated and informed through computationally intensive numerical assessment, experimental data, and semi-empirical relationships based on first principles.

- Presenting an effective approach to predict and map the damage to a reinforced concrete liner of a roadway tunnel from various explosive threat sizes and tunnel geometries.

5 Impacts

- With rapid assessment of thermal demands for calculating appropriate design limit states and understanding risk potential in a multitude of underground environment, potential for cracking, spalling, breach, and other adverse structural consequences can be evaluated based on contour maps of total heat flux over the tunnel liner.
- The proposed approach for assessing blast-induced damage can be used to examine the relationship between increasing blast hazard intensity and the extent of spall and breach damage.

Appendix B: Data from the Project

Figure 33 Heat flux time history at fire location with upper and lower bounds										
Time (sec)	Heat Flux from FDS (kW/m^2)			Time (sec)	Heat Flux Bounds (kW/m^2)					
	30MW	70MW	200MW		30MW LB	30MW UB	70MW LB	70MW UB	200MW LB	200MW UB
0.0	0	0	0	1	0	0	0	0	0	0
0.4	0	0	0	2	0	0	1	0	2	1
0.7	0	0	0	3	1	0	2	1	4	3
1.0	0	0	0	4	1	0	4	2	7	5
1.3	0	0	0	5	2	0	6	3	11	7
1.5	0	0	0	6	3	1	8	4	15	11
1.9	0	0	0	7	4	1	11	5	21	15
2.1	0	0	0	8	5	1	15	7	27	19
2.5	0	0	0	9	6	1	19	8	34	24
2.7	0	1	1	10	8	2	23	10	42	30
3.1	0	1	1	11	10	2	28	12	51	36
3.3	0	1	1	12	11	2	33	15	61	43
3.6	0	1	1	13	13	3	39	17	71	50
3.9	1	1	1	14	16	3	46	20	82	58
4.2	1	1	1	15	18	3	52	23	95	67
4.5	1	1	1	16	20	4	60	26	108	76
4.8	1	1	1	17	23	4	67	29	122	86
5.1	1	1	1	18	26	5	75	33	136	97
5.4	1	1	1	19	29	6	84	37	152	108
5.7	1	1	1	20	32	6	93	41	168	119
6.0	1	1	1	21	35	7	103	45	185	132
6.3	1	1	1	22	38	7	113	49	204	144
6.6	1	1	1	23	42	8	123	54	222	158
6.9	1	1	1	24	46	9	134	59	242	172
7.2	1	1	1	25	50	10	145	64	263	187
7.5	1	1	1	26	54	10	157	69	284	202
7.8	1	1	1	27	58	11	170	74	307	218
8.1	1	1	1	28	62	12	182	80	330	234
8.4	1	1	1	29	67	13	196	86	354	251
8.7	1	1	1	30	71	14	209	92	379	269
9.0	1	1	2	31	71	14	209	92	379	269
9.3	1	1	2	32	71	14	209	92	379	269
9.6	1	1	2	33	71	14	209	92	379	269
9.9	1	1	2	34	71	14	209	92	379	269
10.2	1	1	2	35	71	14	209	92	379	269

10.5	1	1	3	36	71	14	209	92	379	269
10.8	1	2	3	37	71	14	209	92	379	269
11.1	1	2	3	38	71	14	209	92	379	269
11.4	1	2	4	39	71	14	209	92	379	269
11.7	1	2	4	40	71	14	209	92	379	269
12.0	1	2	3	41	71	14	209	92	379	269
12.3	1	2	3	42	71	14	209	92	379	269
12.6	1	3	4	43	71	14	209	92	379	269
12.9	1	3	5	44	71	14	209	92	379	269
13.2	1	3	6	45	71	14	209	92	379	269
13.5	1	3	8	46	71	14	209	92	379	269
13.8	1	3	12	47	71	14	209	92	379	269
14.1	1	3	7	48	71	14	209	92	379	269
14.4	1	3	7	49	71	14	209	92	379	269
14.7	1	3	10	50	71	14	209	92	379	269
15.0	1	3	13	51	71	14	209	92	379	269
15.3	2	3	16	52	71	14	209	92	379	269
15.6	2	4	16	53	71	14	209	92	379	269
15.9	1	8	15	54	71	14	209	92	379	269
16.2	2	7	15	55	71	14	209	92	379	269
16.5	2	5	16	56	71	14	209	92	379	269
16.8	2	5	19	57	71	14	209	92	379	269
17.1	2	6	34	58	71	14	209	92	379	269
17.4	2	6	39	59	71	14	209	92	379	269
17.7	2	7	28	60	71	14	209	92	379	269
18.0	3	5	20	61	71	14	209	92	379	269
18.3	4	5	25	62	71	14	209	92	379	269
18.6	3	12	30	63	71	14	209	92	379	269
18.9	3	38	34	64	71	14	209	92	379	269
19.2	4	42	39	65	71	14	209	92	379	269
19.5	3	12	66	66	71	14	209	92	379	269
19.8	2	9	111	67	71	14	209	92	379	269
20.1	3	11	120	68	71	14	209	92	379	269
20.4	3	21	51	69	71	14	209	92	379	269
20.7	6	22	29	70	71	14	209	92	379	269
21.0	8	8	28	71	71	14	209	92	379	269
21.3	5	10	29	72	71	14	209	92	379	269
21.6	3	20	56	73	71	14	209	92	379	269
21.9	4	82	94	74	71	14	209	92	379	269
22.2	12	75	58	75	71	14	209	92	379	269
22.5	9	13	67	76	71	14	209	92	379	269

22.8	6	14	100	77	71	14	209	92	379	269
23.1	7	22	77	78	71	14	209	92	379	269
23.4	6	58	48	79	71	14	209	92	379	269
23.7	6	84	77	80	71	14	209	92	379	269
24.0	10	51	134	81	71	14	209	92	379	269
24.3	6	26	136	82	71	14	209	92	379	269
24.6	6	61	166	83	71	14	209	92	379	269
24.9	13	93	154	84	71	14	209	92	379	269
25.2	45	56	175	85	71	14	209	92	379	269
25.5	35	150	207	86	71	14	209	92	379	269
25.8	4	169	219	87	71	14	209	92	379	269
26.1	5	103	202	88	71	14	209	92	379	269
26.4	16	50	210	89	71	14	209	92	379	269
26.7	20	108	215	90	71	14	209	92	379	269
27.0	9	93	222	91	71	14	209	92	379	269
27.3	9	67	190	92	71	14	209	92	379	269
27.6	31	117	200	93	71	14	209	92	379	269
27.9	60	168	212	94	71	14	209	92	379	269
28.2	79	192	169	95	71	14	209	92	379	269
28.5	33	97	151	96	71	14	209	92	379	269
28.8	15	49	193	97	71	14	209	92	379	269
29.1	22	73	243	98	71	14	209	92	379	269
29.4	95	129	256	99	71	14	209	92	379	269
29.7	99	185	268	100	71	14	209	92	379	269
30.0	20	124	249	101	71	14	209	92	379	269
30.3	13	159	263	102	71	14	209	92	379	269
30.6	71	187	251	103	71	14	209	92	379	269
30.9	106	156	247	104	71	14	209	92	379	269
31.2	34	147	257	105	71	14	209	92	379	269
31.5	29	125	275	106	71	14	209	92	379	269
31.8	13	130	273	107	71	14	209	92	379	269
32.1	9	139	288	108	71	14	209	92	379	269
32.4	27	100	261	109	71	14	209	92	379	269
32.7	54	157	268	110	71	14	209	92	379	269
33.0	32	229	286	111	71	14	209	92	379	269
33.3	25	156	322	112	71	14	209	92	379	269
33.6	67	100	301	113	71	14	209	92	379	269
33.9	103	153	276	114	71	14	209	92	379	269
34.2	35	194	248	115	71	14	209	92	379	269
34.5	17	158	260	116	71	14	209	92	379	269
34.8	34	129	280	117	71	14	209	92	379	269

35.1	68	174	309	118	71	14	209	92	379	269
35.4	17	154	315	119	71	14	209	92	379	269
35.7	16	44	279	120	71	14	209	92	379	269
36.0	34	63	234	121	71	14	209	92	379	269
36.3	35	81	213	122	71	14	209	92	379	269
36.6	22	176	235	123	71	14	209	92	379	269
36.9	14	225	267	124	71	14	209	92	379	269
37.2	13	244	342	125	71	14	209	92	379	269
37.5	16	244	302	126	71	14	209	92	379	269
37.8	26	185	258	127	71	14	209	92	379	269
38.1	53	145	237	128	71	14	209	92	379	269
38.4	57	116	257	129	71	14	209	92	379	269
38.7	12	141	295	130	71	14	209	92	379	269
39.0	54	123	354	131	71	14	209	92	379	269
39.3	112	165	304	132	71	14	209	92	379	269
39.6	88	237	283	133	71	14	209	92	379	269
39.9	102	212	268	134	71	14	209	92	379	269
40.2	19	187	275	135	71	14	209	92	379	269
40.5	30	140	259	136	71	14	209	92	379	269
40.8	44	123	257	137	71	14	209	92	379	269
41.1	24	161	260	138	71	14	209	92	379	269
41.4	14	124	247	139	71	14	209	92	379	269
41.7	40	60	239	140	71	14	209	92	379	269
42.0	104	96	236	141	71	14	209	92	379	269
42.3	122	137	268	142	71	14	209	92	379	269
42.6	53	229	299	143	71	14	209	92	379	269
42.9	19	205	299	144	71	14	209	92	379	269
43.2	54	95	190	145	71	14	209	92	379	269
43.5	88	70	150	146	71	14	209	92	379	269
43.8	42	105	215	147	71	14	209	92	379	269
44.1	17	157	249	148	71	14	209	92	379	269
44.4	19	43	279	149	71	14	209	92	379	269
44.7	21	45	285	150	71	14	209	92	379	269
45.0	22	140	249	151	71	14	209	92	379	269
45.3	40	207	237	152	71	14	209	92	379	269
45.6	110	251	241	153	71	14	209	92	379	269
45.9	40	248	261	154	71	14	209	92	379	269
46.2	15	154	283	155	71	14	209	92	379	269
46.5	23	120	274	156	71	14	209	92	379	269
46.8	92	145	226	157	71	14	209	92	379	269
47.1	78	194	177	158	71	14	209	92	379	269

47.4	22	145	211	159	71	14	209	92	379	269
47.7	37	64	228	160	71	14	209	92	379	269
48.0	65	130	258	161	71	14	209	92	379	269
48.3	62	120	273	162	71	14	209	92	379	269
48.6	36	153	257	163	71	14	209	92	379	269
48.9	32	185	252	164	71	14	209	92	379	269
49.2	21	81	268	165	71	14	209	92	379	269
49.5	25	105	285	166	71	14	209	92	379	269
49.8	41	146	289	167	71	14	209	92	379	269
50.1	31	205	296	168	71	14	209	92	379	269
50.4	19	95	294	169	71	14	209	92	379	269
50.7	24	65	272	170	71	14	209	92	379	269
51.0	14	189	274	171	71	14	209	92	379	269
51.3	14	189	328	172	71	14	209	92	379	269
51.6	33	115	363	173	71	14	209	92	379	269
51.9	64	150	333	174	71	14	209	92	379	269
52.2	43	123	325	175	71	14	209	92	379	269
52.5	27	180	316	176	71	14	209	92	379	269
52.8	36	159	318	177	71	14	209	92	379	269
53.1	22	29	306	178	71	14	209	92	379	269
53.4	20	31	303	179	71	14	209	92	379	269
53.7	26	76	327	180	71	14	209	92	379	269
54.0	20	174	324	181	71	14	209	92	379	269
54.3	19	64	295	182	71	14	209	92	379	269
54.6	15	82	293	183	71	14	209	92	379	269
54.9	15	171	331	184	71	14	209	92	379	269
55.2	29	221	362	185	71	14	209	92	379	269
55.5	37	259	380	186	71	14	209	92	379	269
55.8	34	241	365	187	71	14	209	92	379	269
56.1	18	177	341	188	71	14	209	92	379	269
56.4	45	208	325	189	71	14	209	92	379	269
56.7	21	251	325	190	71	14	209	92	379	269
57.0	12	215	326	191	71	14	209	92	379	269
57.3	15	103	314	192	71	14	209	92	379	269
57.6	11	40	308	193	71	14	209	92	379	269
57.9	18	51	314	194	71	14	209	92	379	269
58.2	69	171	323	195	71	14	209	92	379	269
58.5	67	179	345	196	71	14	209	92	379	269
58.8	14	70	312	197	71	14	209	92	379	269
59.1	11	48	302	198	71	14	209	92	379	269
59.4	22	68	314	199	71	14	209	92	379	269

59.7	25	165	317	200	71	14	209	92	379	269
60.0	13	214	312	201	71	14	209	92	379	269
60.3	13	88	303	202	71	14	209	92	379	269
60.6	18	65	294	203	71	14	209	92	379	269
60.9	28	80	300	204	71	14	209	92	379	269
61.2	36	91	309	205	71	14	209	92	379	269
61.5	19	123	333	206	71	14	209	92	379	269
61.8	21	48	332	207	71	14	209	92	379	269
62.1	91	44	288	208	71	14	209	92	379	269
62.4	42	74	294	209	71	14	209	92	379	269
62.7	12	147	339	210	71	14	209	92	379	269
63.0	15	225	327	211	71	14	209	92	379	269
63.3	44	161	314	212	71	14	209	92	379	269
63.6	64	49	291	213	71	14	209	92	379	269
63.9	33	42	280	214	71	14	209	92	379	269
64.2	13	73	293	215	71	14	209	92	379	269
64.5	21	114	310	216	71	14	209	92	379	269
64.8	28	90	283	217	71	14	209	92	379	269
65.1	23	84	293	218	71	14	209	92	379	269
65.4	38	118	315	219	71	14	209	92	379	269
65.7	49	63	309	220	71	14	209	92	379	269
66.0	53	147	308	221	71	14	209	92	379	269
66.3	36	227	303	222	71	14	209	92	379	269
66.6	40	202	308	223	71	14	209	92	379	269
66.9	27	115	292	224	71	14	209	92	379	269
67.2	35	96	290	225	71	14	209	92	379	269
67.5	40	178	308	226	71	14	209	92	379	269
67.8	25	137	307	227	71	14	209	92	379	269
68.1	36	151	309	228	71	14	209	92	379	269
68.4	101	124	304	229	71	14	209	92	379	269
68.7	78	109	305	230	71	14	209	92	379	269
69.0	18	165	310	231	71	14	209	92	379	269
69.3	15	196	320	232	71	14	209	92	379	269
69.6	28	177	305	233	71	14	209	92	379	269
69.9	18	121	310	234	71	14	209	92	379	269
70.2	27	155	313	235	71	14	209	92	379	269
70.5	56	222	310	236	71	14	209	92	379	269
70.8	63	133	296	237	71	14	209	92	379	269
71.1	58	99	275	238	71	14	209	92	379	269
71.4	50	105	276	239	71	14	209	92	379	269
71.7	21	102	302	240	71	14	209	92	379	269

72.0	20	68	349	241	71	14	209	92	379	269
72.3	39	79	342	242	71	14	209	92	379	269
72.6	15	142	331	243	71	14	209	92	379	269
72.9	15	204	337	244	71	14	209	92	379	269
73.2	29	216	340	245	71	14	209	92	379	269
73.5	27	129	356	246	71	14	209	92	379	269
73.8	16	87	386	247	71	14	209	92	379	269
74.1	21	148	378	248	71	14	209	92	379	269
74.4	24	204	372	249	71	14	209	92	379	269
74.7	30	240	343	250	71	14	209	92	379	269
75.0	27	145	353	251	71	14	209	92	379	269
75.3	17	48	424	252	71	14	209	92	379	269
75.6	18	46	393	253	71	14	209	92	379	269
75.9	40	105	343	254	71	14	209	92	379	269
76.2	29	208	339	255	71	14	209	92	379	269
76.5	12	174	338	256	71	14	209	92	379	269
76.8	24	151	320	257	71	14	209	92	379	269
77.1	94	201	298	258	71	14	209	92	379	269
77.4	66	203	298	259	71	14	209	92	379	269
77.7	32	107	311	260	71	14	209	92	379	269
78.0	26	34	332	261	71	14	209	92	379	269
78.3	67	37	324	262	71	14	209	92	379	269
78.6	116	128	320	263	71	14	209	92	379	269
78.9	99	192	334	264	71	14	209	92	379	269
79.2	54	177	304	265	71	14	209	92	379	269
79.5	44	156	296	266	71	14	209	92	379	269
79.8	113	210	313	267	71	14	209	92	379	269
80.1	57	112	337	268	71	14	209	92	379	269
80.4	14	43	371	269	71	14	209	92	379	269
80.7	13	69	369	270	71	14	209	92	379	269
81.0	24	126	349	271	71	14	209	92	379	269
81.3	52	201	330	272	71	14	209	92	379	269
81.6	51	163	325	273	71	14	209	92	379	269
81.9	107	103	345	274	71	14	209	92	379	269
82.2	52	64	354	275	71	14	209	92	379	269
82.5	35	131	360	276	71	14	209	92	379	269
82.8	14	141	355	277	71	14	209	92	379	269
83.1	29	99	324	278	71	14	209	92	379	269
83.4	65	70	310	279	71	14	209	92	379	269
83.7	35	91	331	280	71	14	209	92	379	269
84.0	24	159	341	281	71	14	209	92	379	269

84.3	44	239	301	282	71	14	209	92	379	269
84.6	113	238	287	283	71	14	209	92	379	269
84.9	33	105	315	284	71	14	209	92	379	269
85.2	12	141	331	285	71	14	209	92	379	269
85.5	25	178	346	286	71	14	209	92	379	269
85.8	39	167	350	287	71	14	209	92	379	269
86.1	42	215	360	288	71	14	209	92	379	269
86.4	47	159	305	289	71	14	209	92	379	269
86.7	63	70	216	290	71	14	209	92	379	269
87.0	72	92	221	291	71	14	209	92	379	269
87.3	14	156	286	292	71	14	209	92	379	269
87.6	14	112	295	293	71	14	209	92	379	269
87.9	25	179	325	294	71	14	209	92	379	269
88.2	70	175	332	295	71	14	209	92	379	269
88.5	29	188	319	296	71	14	209	92	379	269
88.8	33	187	321	297	71	14	209	92	379	269
89.1	67	131	331	298	71	14	209	92	379	269
89.4	28	157	319	299	71	14	209	92	379	269
89.7	8	194	322	300	71	14	209	92	379	269
90.0	25	176	334							
90.3	61	139	328							
90.6	41	104	311							
90.9	39	42	319							
91.2	34	22	371							
91.5	18	45	356							
91.8	15	140	332							
92.1	20	84	332							
92.4	61	77	321							
92.7	39	142	328							
93.0	37	92	344							
93.3	51	145	320							
93.6	37	140	308							
93.9	17	98	288							
94.2	17	79	319							
94.5	8	104	360							
94.8	17	104	358							
95.1	58	215	366							
95.4	60	174	337							
95.7	96	94	326							
96.0	69	75	316							
96.3	79	152	316							

96.6	60	176	341
96.9	23	100	361
97.2	14	60	356
97.5	32	64	325
97.8	64	70	311
98.1	35	91	308
98.4	9	163	314
98.7	13	182	363
99.0	30	157	340
99.3	52	113	281
99.6	32	102	306
99.9	12	175	305
100.2	14	161	329
100.5	27	151	359
100.8	21	154	355
101.1	33	211	338
101.4	49	237	338
101.7	35	205	335
102.0	20	124	334
102.3	36	101	340
102.6	31	111	343
102.9	65	172	342
103.2	22	164	349
103.5	17	60	344
103.8	39	54	340
104.1	73	116	350
104.4	30	235	321
104.7	75	217	293
105.0	102	163	333
105.3	83	152	318
105.6	42	147	300
105.9	83	164	296
106.2	111	196	317
106.5	57	123	335
106.8	35	163	313
107.1	21	208	318
107.4	40	178	360
107.7	107	157	321
108.0	105	102	279
108.3	37	163	271
108.6	13	200	295

108.9	9	214	288
109.2	9	194	301
109.5	17	189	324
109.8	17	86	335
110.1	27	87	357
110.4	104	142	356
110.7	72	170	340
111.0	49	221	348
111.3	59	133	352
111.6	53	82	349
111.9	104	100	329
112.2	65	113	326
112.5	21	107	334
112.8	17	122	343
113.1	30	59	334
113.4	35	41	294
113.7	14	66	285
114.0	20	156	321
114.3	48	164	309
114.6	53	46	322
114.9	23	52	342
115.2	40	109	335
115.5	94	133	315
115.8	53	135	303
116.1	33	71	305
116.4	31	50	321
116.7	111	59	332
117.0	60	151	352
117.3	16	277	339
117.6	15	244	305
117.9	42	203	304
118.2	46	152	333
118.5	13	169	349
118.8	14	132	361
119.1	26	98	371
119.4	34	87	378
119.7	24	60	372
120.0	16	120	356
120.3	18	158	392
120.6	32	140	380
120.9	16	200	367

121.2	29	156	369
121.5	51	69	330
121.8	25	96	307
122.1	46	212	309
122.4	43	233	310
122.7	13	223	328
123.0	9	250	312
123.3	20	159	329
123.6	48	64	349
123.9	41	82	328
124.2	28	190	335
124.5	60	234	324
124.8	80	116	313
125.1	31	77	336
125.4	13	173	335
125.7	34	219	332
126.0	103	236	332
126.3	55	168	343
126.6	17	64	368
126.9	11	54	378
127.2	49	90	354
127.5	71	117	372
127.8	23	208	361
128.1	27	268	392
128.4	39	251	363
128.7	32	207	345
129.0	22	191	357
129.3	25	235	314
129.6	90	107	271
129.9	69	78	280
130.2	36	153	303
130.5	75	164	328
130.8	70	167	336
131.1	13	94	367
131.4	9	56	375
131.7	11	63	396
132.0	21	122	416
132.3	39	228	401
132.6	47	169	402
132.9	105	58	387
133.2	108	87	367

133.5	177	181	425
133.8	97	186	419
134.1	41	132	407
134.4	65	151	374
134.7	60	115	335
135.0	27	140	299
135.3	34	226	323
135.6	38	221	323
135.9	23	84	355
136.2	17	77	383
136.5	26	129	366
136.8	68	209	352
137.1	110	168	317
137.4	32	65	267
137.7	14	112	280
138.0	23	219	321
138.3	21	250	339
138.6	61	192	333
138.9	101	97	338
139.2	53	59	360
139.5	51	165	372
139.8	48	205	405
140.1	17	165	388
140.4	8	100	378
140.7	20	162	383
141.0	43	243	368
141.3	31	217	381
141.6	9	265	365
141.9	11	131	349
142.2	19	46	359
142.5	35	79	343
142.8	138	143	348
143.1	68	161	350
143.4	42	144	375
143.7	61	132	390
144.0	22	222	378
144.3	18	190	381
144.6	10	97	396
144.9	21	168	357
145.2	75	241	335
145.5	62	213	349

145.8	14	184	354
146.1	12	154	371
146.4	14	177	388
146.7	10	125	373
147.0	12	164	339
147.3	38	179	332
147.6	141	224	369
147.9	123	210	380
148.2	20	188	404
148.5	12	109	392
148.8	12	138	391
149.1	28	183	402
149.4	52	199	406
149.7	49	234	416
150.0	45	272	385
150.3	55	128	366
150.6	24	102	366
150.9	65	180	354
151.2	41	110	362
151.5	22	100	371
151.8	25	123	354
152.1	21	208	336
152.4	29	257	336
152.7	13	277	329
153.0	11	220	341
153.3	22	144	380
153.6	39	91	376
153.9	57	181	370
154.2	32	199	353
154.5	23	214	333
154.8	21	234	354
155.1	17	274	356
155.4	13	278	324
155.7	16	245	306
156.0	23	199	297
156.3	48	103	305
156.6	94	63	332
156.9	29	85	386
157.2	15	113	410
157.5	34	173	396
157.8	101	185	396

158.1	113	195	375
158.4	39	167	362
158.7	84	86	366
159.0	117	98	387
159.3	63	136	403
159.6	43	168	392
159.9	85	166	350
160.2	24	229	343
160.5	30	214	374
160.8	30	220	370
161.1	12	221	376
161.4	20	112	373
161.7	55	42	387
162.0	62	46	368
162.3	20	112	330
162.6	23	206	331
162.9	11	186	335
163.2	21	136	314
163.5	41	106	298
163.8	21	63	284
164.1	41	70	314
164.4	30	88	326
164.7	13	152	341
165.0	14	231	321
165.3	22	231	333
165.6	48	229	328
165.9	25	241	325
166.2	38	176	344
166.5	19	177	407
166.8	14	129	401
167.1	25	219	372
167.4	83	223	356
167.7	133	218	335
168.0	21	225	336
168.3	39	225	349
168.6	106	160	358
168.9	72	189	392
169.2	67	243	382
169.5	26	258	351
169.8	31	277	325
170.1	55	280	327

170.4	45	266	328
170.7	21	241	341
171.0	18	202	364
171.3	33	115	355
171.6	29	55	363
171.9	16	104	350
172.2	23	194	332
172.5	37	186	330
172.8	34	182	363
173.1	20	149	387
173.4	22	139	385
173.7	70	161	363
174.0	39	56	373
174.3	11	37	376
174.6	18	118	380
174.9	78	145	386
175.2	161	101	363
175.5	111	127	348
175.8	91	161	349
176.1	94	120	321
176.4	46	63	292
176.7	25	104	299
177.0	61	102	308
177.3	117	134	336
177.6	47	149	332
177.9	35	191	342
178.2	80	198	360
178.5	65	187	367
178.8	18	135	380
179.1	19	147	387
179.4	18	133	372
179.7	26	97	369
180.0	29	82	382
180.3	44	98	397
180.6	56	113	389
180.9	41	110	391
181.2	27	143	388
181.5	51	120	371
181.8	22	69	391
182.1	69	115	387
182.4	73	136	401

182.7	47	133	406
183.0	23	135	394
183.3	18	75	401
183.6	28	65	400
183.9	27	145	385
184.2	22	167	395
184.5	31	206	412
184.8	74	168	402
185.1	123	182	391
185.4	41	176	384
185.7	22	199	384
186.0	32	212	390
186.3	37	88	397
186.6	31	61	390
186.9	47	122	408
187.2	34	212	402
187.5	22	160	376
187.8	21	53	371
188.1	17	73	392
188.4	12	182	390
188.7	10	149	370
189.0	20	95	363
189.3	30	97	361
189.6	30	187	353
189.9	20	180	350
190.2	17	241	351
190.5	33	236	365
190.8	34	180	362
191.1	39	175	374
191.4	49	241	375
191.7	39	265	372
192.0	21	235	385
192.3	24	136	374
192.6	47	97	372
192.9	136	140	372
193.2	93	198	366
193.5	13	137	359
193.8	15	124	374
194.1	41	202	370
194.4	65	218	378
194.7	84	151	405

195.0	27	108	396
195.3	26	136	397
195.6	50	81	378
195.9	65	70	379
196.2	17	169	374
196.5	37	127	338
196.8	57	113	313
197.1	103	174	356
197.4	64	228	362
197.7	55	158	358
198.0	25	36	364
198.3	29	36	368
198.6	96	120	401
198.9	41	214	409
199.2	22	231	387
199.5	15	285	375
199.8	40	276	361
200.1	73	262	363
200.4	25	247	362
200.7	22	106	361
201.0	55	25	373
201.3	112	26	401
201.6	45	88	381
201.9	13	212	369
202.2	17	161	370
202.5	57	61	398
202.8	104	81	375
203.1	37	128	333
203.4	13	239	328
203.7	29	249	350
204.0	37	199	347
204.3	63	185	361
204.6	103	238	379
204.9	55	248	376
205.2	29	129	395
205.5	45	138	397
205.8	83	86	330
206.1	45	107	363
206.4	57	122	344
206.7	20	183	329
207.0	21	215	333

207.3	71	181	341
207.6	49	191	328
207.9	31	197	346
208.2	18	149	361
208.5	27	176	371
208.8	69	162	369
209.1	59	203	372
209.4	65	103	361
209.7	138	68	366
210.0	100	89	363
210.3	76	169	370
210.6	13	208	372
210.9	14	277	354
211.2	34	165	344
211.5	64	196	342
211.8	59	191	351
212.1	20	179	364
212.4	19	72	375
212.7	46	57	371
213.0	38	149	350
213.3	15	221	345
213.6	14	238	354
213.9	39	251	355
214.2	69	220	401
214.5	53	162	412
214.8	18	199	385
215.1	32	143	383
215.4	37	104	412
215.7	54	142	398
216.0	21	222	394
216.3	18	265	415
216.6	24	239	393
216.9	86	160	364
217.2	58	180	341
217.5	46	136	354
217.8	89	119	384
218.1	109	186	412
218.4	35	122	406
218.7	28	53	384
219.0	68	156	373
219.3	59	209	372

219.6	39	151	367
219.9	27	109	396
220.2	33	90	424
220.5	88	163	419
220.8	31	137	399
221.1	12	72	395
221.4	7	122	404
221.7	20	168	395
222.0	44	135	369
222.3	38	215	336
222.6	38	141	352
222.9	77	109	385
223.2	105	136	425
223.5	48	140	415
223.8	37	170	395
224.1	42	153	395
224.4	71	162	397
224.7	26	173	411
225.0	9	187	406
225.3	12	193	357
225.6	30	225	362
225.9	67	256	376
226.2	32	265	361
226.5	79	220	369
226.8	46	174	377
227.1	17	138	369
227.4	18	55	369
227.7	25	60	360
228.0	30	153	362
228.3	57	197	332
228.6	128	221	315
228.9	95	148	325
229.2	41	141	325
229.5	66	203	330
229.8	118	232	331
230.1	113	189	358
230.4	42	89	363
230.7	12	52	348
231.0	28	75	351
231.3	54	146	291
231.6	9	189	323

231.9	9	202	354
232.2	15	218	361
232.5	31	237	356
232.8	95	201	362
233.1	129	141	369
233.4	64	126	391
233.7	57	70	382
234.0	102	129	382
234.3	64	211	388
234.6	39	228	391
234.9	19	94	434
235.2	37	39	423
235.5	117	86	376
235.8	118	151	316
236.1	89	144	279
236.4	71	185	298
236.7	42	187	302
237.0	40	198	299
237.3	54	252	280
237.6	28	270	273
237.9	33	277	267
238.2	58	262	265
238.5	37	191	274
238.8	12	85	277
239.1	25	120	296
239.4	55	204	314
239.7	34	202	320
240.0	30	151	350
240.3	33	225	354
240.6	71	192	373
240.9	50	147	375
241.2	32	114	361
241.5	70	97	346
241.8	105	134	342
242.1	40	190	354
242.4	24	245	374
242.7	15	246	367
243.0	62	241	327
243.3	59	207	268
243.6	133	176	276
243.9	153	241	285

244.2	69	209	281
244.5	18	167	319
244.8	13	109	363
245.1	39	99	371
245.4	63	141	343
245.7	17	243	309
246.0	12	218	262
246.3	24	122	248
246.6	17	111	297
246.9	14	119	322
247.2	27	190	326
247.5	34	150	341
247.8	28	190	336
248.1	19	164	326
248.4	11	155	322
248.7	25	212	331
249.0	22	208	346
249.3	12	234	308
249.6	17	232	265
249.9	35	151	307
250.2	45	121	297
250.5	22	76	295
250.8	11	106	268
251.1	60	155	250
251.4	134	221	251
251.7	77	158	281
252.0	89	139	306
252.3	54	206	309
252.6	39	189	278
252.9	61	86	300
253.2	44	77	299
253.5	22	112	272
253.8	31	148	263
254.1	38	211	274
254.4	47	75	263
254.7	31	75	213
255.0	14	132	211
255.3	18	204	194
255.6	28	105	193
255.9	13	50	178
256.2	27	104	161

256.5	35	197	170
256.8	51	240	172
257.1	19	162	179
257.4	30	150	185
257.7	129	115	218
258.0	95	108	244
258.3	97	190	236
258.6	28	138	259
258.9	22	125	223
259.2	24	157	194
259.5	26	166	205
259.8	16	152	242
260.1	40	125	246
260.4	73	48	241
260.7	34	46	252
261.0	20	51	275
261.3	57	145	327
261.6	39	205	323
261.9	51	195	315
262.2	67	133	332
262.5	65	214	288
262.8	45	228	264
263.1	55	198	270
263.4	143	99	264
263.7	84	142	249
264.0	58	194	246
264.3	66	215	248
264.6	21	204	262
264.9	30	125	246
265.2	41	54	225
265.5	46	130	214
265.8	56	197	214
266.1	25	237	262
266.4	61	212	305
266.7	83	78	315
267.0	33	60	328
267.3	14	147	401
267.6	23	238	404
267.9	38	109	395
268.2	34	93	362
268.5	32	121	359

268.8	79	147	362
269.1	39	137	360
269.4	24	146	364
269.7	38	152	338
270.0	36	210	304
270.3	56	181	281
270.6	57	184	265
270.9	41	127	256
271.2	32	51	251
271.5	11	111	255
271.8	29	192	260
272.1	83	184	275
272.4	40	125	258
272.7	64	107	262
273.0	51	100	280
273.3	62	149	299
273.6	67	121	336
273.9	30	178	348
274.2	24	172	333
274.5	51	139	294
274.8	48	192	257
275.1	22	271	247
275.4	35	226	225
275.7	19	101	223
276.0	37	123	218
276.3	81	188	192
276.6	33	76	173
276.9	22	121	167
277.2	20	120	180
277.5	20	61	199
277.8	26	88	207
278.1	29	111	221
278.4	75	101	241
278.7	34	102	230
279.0	17	164	203
279.3	21	235	207
279.6	54	115	219
279.9	30	139	212
280.2	19	204	203
280.5	42	209	203
280.8	31	163	233

281.1	25	170	263
281.4	39	158	234
281.7	80	185	213
282.0	19	222	213
282.3	9	193	215
282.6	16	100	209
282.9	47	134	196
283.2	133	199	210
283.5	113	230	257
283.8	48	246	268
284.1	77	187	294
284.4	57	73	291
284.7	20	65	291
285.0	36	129	265
285.3	79	70	244
285.6	94	147	219
285.9	79	205	198
286.2	41	139	180
286.5	15	101	173
286.8	50	232	183
287.1	93	150	225
287.4	21	83	254
287.7	9	70	255
288.0	10	119	256
288.3	11	202	250
288.6	21	154	266
288.9	63	167	288
289.2	32	165	302
289.5	31	208	328
289.8	41	258	327
290.1	40	145	300
290.4	13	75	253
290.7	16	61	228
291.0	30	93	220
291.3	28	80	222
291.6	20	37	244
291.9	17	62	277
292.2	20	143	307
292.5	33	235	283
292.8	80	249	275
293.1	59	229	274

293.4	19	247	286
293.7	33	238	295
294.0	34	229	296
294.3	28	176	241
294.6	62	180	193
294.9	34	235	185
295.2	36	88	231
295.5	57	36	227
295.8	19	100	212
296.1	26	133	206
296.4	37	127	198
296.7	49	157	201
297.0	77	158	212
297.3	98	152	200
297.6	54	145	198
297.9	50	204	213
298.2	27	129	244
298.5	21	59	290
298.8	28	117	310
299.1	34	207	317
299.4	25	183	339
299.7	41	63	348
300.0	73	113	359

Figure34 Through-thickness temperature gradients above fire (top) and 20 meters from fire (bottom) for 30MW (left), 70MW (center) and 200MW (right) fires

Ceiling Temperature through thickness for 30MW Fire (℃) at fire location

Depth into the panel (m)	50 sec			150 sec			250 sec		
	LB	MEAN	UB	LB	MEAN	UB	LB	MEAN	UB
0.004	50.7	106.5	159.5	90.6	221.2	345.7	109.9	296.4	435
0.008	32.9	52	71.9	68.5	143.6	219.1	88.4	216.5	308.5
0.012	24.4	29	38.1	51.9	95	138.2	71.2	150.6	216.9
0.016	21.2	21.8	25.1	40	65.9	90.2	57.3	108.4	151.4
0.020	20.2	20.2	21.1	31.9	47.2	61.8	46.4	81	107.8
0.024	20	20	20.2	26.8	35.3	43.8	38.2	61.5	79.6
0.028	20	20	20	23.6	28.1	32.9	32.2	47.6	59.8
0.032	20	20	20	21.8	24.1	26.6	27.9	37.8	45.9

0.036	20	20	20	20.9	21.9	23.1	24.9	31.1	36.4
0.04	20	20	20	20.4	20.8	21.4	23	26.7	30
0.044	20	20	20	20.2	20.3	20.6	21.8	23.9	26
0.048	20	20	20	20.1	20.1	20.2	21	22.2	23.4
0.052	20	20	20	20	20	20.1	20.5	21.2	21.9
0.056	20	20	20	20	20	20	20.3	20.6	21
0.060	20	20	20	20	20	20	20.1	20.3	20.5
0.064	20	20	20	20	20	20	20.1	20.2	20.2
0.068	20	20	20	20	20	20	20	20.1	20.1
0.072	20	20	20	20	20	20	20	20	20.1
0.076	20	20	20	20	20	20	20	20	20
0.08	20	20	20	20	20	20	20	20	20
0.084	20	20	20	20	20	20	20	20	20
0.088	20	20	20	20	20	20	20	20	20
0.092	20	20	20	20	20	20	20	20	20
0.096	20	20	20	20	20	20	20	20	20
0.100	20	20	20	20	20	20	20	20	20
0.104	20	20	20	20	20	20	20	20	20
0.108	20	20	20	20	20	20	20	20	20
0.112	20	20	20	20	20	20	20	20	20
0.116	20	20	20	20	20	20	20	20	20
0.12	20	20	20	20	20	20	20	20	20
0.124	20	20	20	20	20	20	20	20	20
0.128	20	20	20	20	20	20	20	20	20
0.132	20	20	20	20	20	20	20	20	20
0.136	20	20	20	20	20	20	20	20	20
0.140	20	20	20	20	20	20	20	20	20
0.144	20	20	20	20	20	20	20	20	20
0.148	20	20	20	20	20	20	20	20	20
0.152	20	20	20	20	20	20	20	20	20
0.156	20	20	20	20	20	20	20	20	20
0.16	20	20	20	20	20	20	20	20	20
0.164	20	20	20	20	20	20	20	20	20
0.168	20	20	20	20	20	20	20	20	20
0.172	20	20	20	20	20	20	20	20	20
0.176	20	20	20	20	20	20	20	20	20
0.180	20	20	20	20	20	20	20	20	20
0.184	20	20	20	20	20	20	20	20	20
0.188	20	20	20	20	20	20	20	20	20
0.192	20	20	20	20	20	20	20	20	20
0.196	20	20	20	20	20	20	20	20	20

0.2	20	20	20	20	20	20	20	20	20
0.204	20	20	20	20	20	20	20	20	20
0.208	20	20	20	20	20	20	20	20	20
0.212	20	20	20	20	20	20	20	20	20
0.216	20	20	20	20	20	20	20	20	20
0.220	20	20	20	20	20	20	20	20	20
0.224	20	20	20	20	20	20	20	20	20
0.228	20	20	20	20	20	20	20	20	20
0.232	20	20	20	20	20	20	20	20	20
0.236	20	20	20	20	20	20	20	20	20
0.24	20	20	20	20	20	20	20	20	20
0.244	20	20	20	20	20	20	20	20	20
0.248	20	20	20	20	20	20	20	20	20
0.252	20	20	20	20	20	20	20	20	20
0.256	20	20	20	20	20	20	20	20	20
0.260	20	20	20	20	20	20	20	20	20
0.264	20	20	20	20	20	20	20	20	20
0.268	20	20	20	20	20	20	20	20	20
0.272	20	20	20	20	20	20	20	20	20
0.276	20	20	20	20	20	20	20	20	20
0.28	20	20	20	20	20	20	20	20	20
0.284	20	20	20	20	20	20	20	20	20
0.288	20	20	20	20	20	20	20	20	20
0.292	20	20	20	20	20	20	20	20	20
0.296	20	20	20	20	20	20	20	20	20
0.300	20	20	20	20	20	20	20	20	20
0.304	20	20	20	20	20	20	20	20	20
0.308	20	20	20	20	20	20	20	20	20
0.312	20	20	20	20	20	20	20	20	20
0.316	20	20	20	20	20	20	20	20	20
0.32	20	20	20	20	20	20	20	20	20
0.324	20	20	20	20	20	20	20	20	20
0.328	20	20	20	20	20	20	20	20	20
0.332	20	20	20	20	20	20	20	20	20
0.336	20	20	20	20	20	20	20	20	20
0.340	20	20	20	20	20	20	20	20	20
0.344	20	20	20	20	20	20	20	20	20
0.348	20	20	20	20	20	20	20	20	20
0.352	20	20	20	20	20	20	20	20	20
0.356	20	20	20	20	20	20	20	20	20
0.36	20	20	20	20	20	20	20	20	20

0.364	20	20	20	20	20	20	20	20	20
0.368	20	20	20	20	20	20	20	20	20
0.372	20	20	20	20	20	20	20	20	20
0.376	20	20	20	20	20	20	20	20	20
0.380	20	20	20	20	20	20	20	20	20
0.384	20	20	20	20	20	20	20	20	20
0.388	20	20	20	20	20	20	20	20	20
0.392	20	20	20	20	20	20	20	20	20
0.396	20	20	20	20	20	20	20	20	20
0.4	20	20	20	20	20	20	20	20	20
0.404	20	20	20	20	20	20	20	20	20
0.408	20	20	20	20	20	20	20	20	20
0.412	20	20	20	20	20	20	20	20	20
0.416	20	20	20	20	20	20	20	20	20
0.420	20	20	20	20	20	20	20	20	20
0.424	20	20	20	20	20	20	20	20	20
0.428	20	20	20	20	20	20	20	20	20
0.432	20	20	20	20	20	20	20	20	20
0.436	20	20	20	20	20	20	20	20	20
0.44	20	20	20	20	20	20	20	20	20
0.444	20	20	20	20	20	20	20	20	20
0.448	20	20	20	20	20	20	20	20	20
0.452	20	20	20	20	20	20	20	20	20
0.456	20	20	20	20	20	20	20	20	20
0.460	20	20	20	20	20	20	20	20	20
0.464	20	20	20	20	20	20	20	20	20
0.468	20	20	20	20	20	20	20	20	20
0.472	20	20	20	20	20	20	20	20	20
0.476	20	20	20	20	20	20	20	20	20
0.48	20	20	20	20	20	20	20	20	20
0.484	20	20	20	20	20	20	20	20	20
0.488	20	20	20	20	20	20	20	20	20
0.492	20	20	20	20	20	20	20	20	20
0.496	20	20	20	20	20	20	20	20	20
0.500	20	20	20	20	20	20	20	20	20
0.504	20	20	20	20	20	20	20	20	20
0.508	20	20	20	20	20	20	20	20	20
0.512	20	20	20	20	20	20	20	20	20
0.516	20	20	20	20	20	20	20	20	20
0.52	20	20	20	20	20	20	20	20	20
0.524	20	20	20	20	20	20	20	20	20

0.528	20	20	20	20	20	20	20	20	20
0.532	20	20	20	20	20	20	20	20	20
0.536	20	20	20	20	20	20	20	20	20
0.540	20	20	20	20	20	20	20	20	20
0.544	20	20	20	20	20	20	20	20	20
0.548	20	20	20	20	20	20	20	20	20
0.552	20	20	20	20	20	20	20	20	20
0.556	20	20	20	20	20	20	20	20	20
0.56	20	20	20	20	20	20	20	20	20
0.564	20	20	20	20	20	20	20	20	20
0.568	20	20	20	20	20	20	20	20	20
0.572	20	20	20	20	20	20	20	20	20
0.576	20	20	20	20	20	20	20	20	20
0.580	20	20	20	20	20	20	20	20	20
0.584	20	20	20	20	20	20	20	20	20
0.588	20	20	20	20	20	20	20	20	20
0.592	20	20	20	20	20	20	20	20	20
0.596	20	20	20	20	20	20	20	20	20
0.6	20	20	20	20	20	20	20	20	20
0.604	20	20	20	20	20	20	20	20	20
0.608	20	20	20	20	20	20	20	20	20
0.612	20	20	20	20	20	20	20	20	20
0.616	20	20	20	20	20	20	20	20	20
0.620	20	20	20	20	20	20	20	20	20
0.624	20	20	20	20	20	20	20	20	20
0.628	20	20	20	20	20	20	20	20	20

Ceiling Temperature through thickness for 30MW Fire (℃) 20m from fire location

Depth into the panel (m)	50 sec			150 sec			250 sec		
	LB	MEAN	UB	LB	MEAN	UB	LB	MEAN	UB
0.004	25	24.8	27.8	31.5	33.5	37.8	35.2	39.6	43.6
0.008	22.1	21.9	23.3	28	29.1	32.4	31.6	34.7	38.1
0.012	20.7	20.6	21.1	25.3	25.7	28.2	28.7	30.6	33.5
0.016	20.2	20.2	20.3	23.3	23.5	25.2	26.4	27.5	29.8
0.020	20	20	20.1	22	22.1	23.1	24.5	25.2	27
0.024	20	20	20	21.1	21.2	21.8	23.1	23.5	24.8
0.028	20	20	20	20.6	20.6	20.9	22.1	22.3	23.2
0.032	20	20	20	20.3	20.3	20.5	21.3	21.5	22.1
0.036	20	20	20	20.1	20.1	20.2	20.8	20.9	21.3
0.04	20	20	20	20.1	20.1	20.1	20.5	20.5	20.8

0.044	20	20	20	20	20	20	20.3	20.3	20.5
0.048	20	20	20	20	20	20	20.2	20.2	20.3
0.052	20	20	20	20	20	20	20.1	20.1	20.1
0.056	20	20	20	20	20	20	20	20	20.1
0.060	20	20	20	20	20	20	20	20	20
0.064	20	20	20	20	20	20	20	20	20
0.068	20	20	20	20	20	20	20	20	20
0.072	20	20	20	20	20	20	20	20	20
0.076	20	20	20	20	20	20	20	20	20
0.08	20	20	20	20	20	20	20	20	20
0.084	20	20	20	20	20	20	20	20	20
0.088	20	20	20	20	20	20	20	20	20
0.092	20	20	20	20	20	20	20	20	20
0.096	20	20	20	20	20	20	20	20	20
0.100	20	20	20	20	20	20	20	20	20
0.104	20	20	20	20	20	20	20	20	20
0.108	20	20	20	20	20	20	20	20	20
0.112	20	20	20	20	20	20	20	20	20
0.116	20	20	20	20	20	20	20	20	20
0.12	20	20	20	20	20	20	20	20	20
0.124	20	20	20	20	20	20	20	20	20
0.128	20	20	20	20	20	20	20	20	20
0.132	20	20	20	20	20	20	20	20	20
0.136	20	20	20	20	20	20	20	20	20
0.140	20	20	20	20	20	20	20	20	20
0.144	20	20	20	20	20	20	20	20	20
0.148	20	20	20	20	20	20	20	20	20
0.152	20	20	20	20	20	20	20	20	20
0.156	20	20	20	20	20	20	20	20	20
0.16	20	20	20	20	20	20	20	20	20
0.164	20	20	20	20	20	20	20	20	20
0.168	20	20	20	20	20	20	20	20	20
0.172	20	20	20	20	20	20	20	20	20
0.176	20	20	20	20	20	20	20	20	20
0.180	20	20	20	20	20	20	20	20	20
0.184	20	20	20	20	20	20	20	20	20
0.188	20	20	20	20	20	20	20	20	20
0.192	20	20	20	20	20	20	20	20	20
0.196	20	20	20	20	20	20	20	20	20
0.2	20	20	20	20	20	20	20	20	20
0.204	20	20	20	20	20	20	20	20	20

0.208	20	20	20	20	20	20	20	20	20
0.212	20	20	20	20	20	20	20	20	20
0.216	20	20	20	20	20	20	20	20	20
0.220	20	20	20	20	20	20	20	20	20
0.224	20	20	20	20	20	20	20	20	20
0.228	20	20	20	20	20	20	20	20	20
0.232	20	20	20	20	20	20	20	20	20
0.236	20	20	20	20	20	20	20	20	20
0.24	20	20	20	20	20	20	20	20	20
0.244	20	20	20	20	20	20	20	20	20
0.248	20	20	20	20	20	20	20	20	20
0.252	20	20	20	20	20	20	20	20	20
0.256	20	20	20	20	20	20	20	20	20
0.260	20	20	20	20	20	20	20	20	20
0.264	20	20	20	20	20	20	20	20	20
0.268	20	20	20	20	20	20	20	20	20
0.272	20	20	20	20	20	20	20	20	20
0.276	20	20	20	20	20	20	20	20	20
0.28	20	20	20	20	20	20	20	20	20
0.284	20	20	20	20	20	20	20	20	20
0.288	20	20	20	20	20	20	20	20	20
0.292	20	20	20	20	20	20	20	20	20
0.296	20	20	20	20	20	20	20	20	20
0.300	20	20	20	20	20	20	20	20	20
0.304	20	20	20	20	20	20	20	20	20
0.308	20	20	20	20	20	20	20	20	20
0.312	20	20	20	20	20	20	20	20	20
0.316	20	20	20	20	20	20	20	20	20
0.32	20	20	20	20	20	20	20	20	20
0.324	20	20	20	20	20	20	20	20	20
0.328	20	20	20	20	20	20	20	20	20
0.332	20	20	20	20	20	20	20	20	20
0.336	20	20	20	20	20	20	20	20	20
0.340	20	20	20	20	20	20	20	20	20
0.344	20	20	20	20	20	20	20	20	20
0.348	20	20	20	20	20	20	20	20	20
0.352	20	20	20	20	20	20	20	20	20
0.356	20	20	20	20	20	20	20	20	20
0.36	20	20	20	20	20	20	20	20	20
0.364	20	20	20	20	20	20	20	20	20
0.368	20	20	20	20	20	20	20	20	20

0.372	20	20	20	20	20	20	20	20	20
0.376	20	20	20	20	20	20	20	20	20
0.380	20	20	20	20	20	20	20	20	20
0.384	20	20	20	20	20	20	20	20	20
0.388	20	20	20	20	20	20	20	20	20
0.392	20	20	20	20	20	20	20	20	20
0.396	20	20	20	20	20	20	20	20	20
0.4	20	20	20	20	20	20	20	20	20
0.404	20	20	20	20	20	20	20	20	20
0.408	20	20	20	20	20	20	20	20	20
0.412	20	20	20	20	20	20	20	20	20
0.416	20	20	20	20	20	20	20	20	20
0.420	20	20	20	20	20	20	20	20	20
0.424	20	20	20	20	20	20	20	20	20
0.428	20	20	20	20	20	20	20	20	20
0.432	20	20	20	20	20	20	20	20	20
0.436	20	20	20	20	20	20	20	20	20
0.44	20	20	20	20	20	20	20	20	20
0.444	20	20	20	20	20	20	20	20	20
0.448	20	20	20	20	20	20	20	20	20
0.452	20	20	20	20	20	20	20	20	20
0.456	20	20	20	20	20	20	20	20	20
0.460	20	20	20	20	20	20	20	20	20
0.464	20	20	20	20	20	20	20	20	20
0.468	20	20	20	20	20	20	20	20	20
0.472	20	20	20	20	20	20	20	20	20
0.476	20	20	20	20	20	20	20	20	20
0.48	20	20	20	20	20	20	20	20	20
0.484	20	20	20	20	20	20	20	20	20
0.488	20	20	20	20	20	20	20	20	20
0.492	20	20	20	20	20	20	20	20	20
0.496	20	20	20	20	20	20	20	20	20
0.500	20	20	20	20	20	20	20	20	20
0.504	20	20	20	20	20	20	20	20	20
0.508	20	20	20	20	20	20	20	20	20
0.512	20	20	20	20	20	20	20	20	20
0.516	20	20	20	20	20	20	20	20	20
0.52	20	20	20	20	20	20	20	20	20
0.524	20	20	20	20	20	20	20	20	20
0.528	20	20	20	20	20	20	20	20	20
0.532	20	20	20	20	20	20	20	20	20

0.536	20	20	20	20	20	20	20	20	20
0.540	20	20	20	20	20	20	20	20	20
0.544	20	20	20	20	20	20	20	20	20
0.548	20	20	20	20	20	20	20	20	20
0.552	20	20	20	20	20	20	20	20	20
0.556	20	20	20	20	20	20	20	20	20
0.56	20	20	20	20	20	20	20	20	20
0.564	20	20	20	20	20	20	20	20	20
0.568	20	20	20	20	20	20	20	20	20
0.572	20	20	20	20	20	20	20	20	20
0.576	20	20	20	20	20	20	20	20	20
0.580	20	20	20	20	20	20	20	20	20
0.584	20	20	20	20	20	20	20	20	20
0.588	20	20	20	20	20	20	20	20	20
0.592	20	20	20	20	20	20	20	20	20
0.596	20	20	20	20	20	20	20	20	20
0.6	20	20	20	20	20	20	20	20	20
0.604	20	20	20	20	20	20	20	20	20
0.608	20	20	20	20	20	20	20	20	20
0.612	20	20	20	20	20	20	20	20	20
0.616	20	20	20	20	20	20	20	20	20
0.620	20	20	20	20	20	20	20	20	20
0.624	20	20	20	20	20	20	20	20	20
0.628	20	20	20	20	20	20	20	20	20

Ceiling Temperature through thickness for 70MW Fire (℃) at fire location

Depth into the panel (m)	50 sec			150 sec			250 sec		
	LB	MEAN	UB	LB	MEAN	UB	LB	MEAN	UB
0.004	202.2	306.9	437.7	434.6	632.9	766.6	531.4	749.6	852.3
0.008	84.3	101.8	146	270	351.8	453	372	494.8	577
0.012	41.5	42	56.5	166	212.1	269.6	259.4	334.8	392.3
0.016	26.1	24.7	29.9	104.2	127.8	159.7	179.3	227.2	267.4
0.020	21.3	20.6	22.1	69.5	81.2	97.4	124.6	153.3	181.1
0.024	20.2	20	20.4	48.2	54.8	63.9	89.7	106.1	123.6
0.028	20	20	20	35.3	38.7	44	66.6	76.8	87.8
0.032	20	20	20	27.8	29.4	32.3	50.4	56.9	64.5
0.036	20	20	20	23.7	24.4	26	39.3	43.3	48.5
0.04	20	20	20	21.7	21.9	22.7	31.8	34.3	37.6
0.044	20	20	20	20.7	20.8	21.1	27	28.5	30.6
0.048	20	20	20	20.3	20.3	20.4	24	24.8	26.1
0.052	20	20	20	20.1	20.1	20.2	22.2	22.7	23.4

0.056	20	20	20	20	20	20.1	21.2	21.4	21.8
0.060	20	20	20	20	20	20	20.6	20.7	20.9
0.064	20	20	20	20	20	20	20.3	20.3	20.5
0.068	20	20	20	20	20	20	20.1	20.2	20.2
0.072	20	20	20	20	20	20	20.1	20.1	20.1
0.076	20	20	20	20	20	20	20	20	20
0.08	20	20	20	20	20	20	20	20	20
0.084	20	20	20	20	20	20	20	20	20
0.088	20	20	20	20	20	20	20	20	20
0.092	20	20	20	20	20	20	20	20	20
0.096	20	20	20	20	20	20	20	20	20
0.100	20	20	20	20	20	20	20	20	20
0.104	20	20	20	20	20	20	20	20	20
0.108	20	20	20	20	20	20	20	20	20
0.112	20	20	20	20	20	20	20	20	20
0.116	20	20	20	20	20	20	20	20	20
0.12	20	20	20	20	20	20	20	20	20
0.124	20	20	20	20	20	20	20	20	20
0.128	20	20	20	20	20	20	20	20	20
0.132	20	20	20	20	20	20	20	20	20
0.136	20	20	20	20	20	20	20	20	20
0.140	20	20	20	20	20	20	20	20	20
0.144	20	20	20	20	20	20	20	20	20
0.148	20	20	20	20	20	20	20	20	20
0.152	20	20	20	20	20	20	20	20	20
0.156	20	20	20	20	20	20	20	20	20
0.16	20	20	20	20	20	20	20	20	20
0.164	20	20	20	20	20	20	20	20	20
0.168	20	20	20	20	20	20	20	20	20
0.172	20	20	20	20	20	20	20	20	20
0.176	20	20	20	20	20	20	20	20	20
0.180	20	20	20	20	20	20	20	20	20
0.184	20	20	20	20	20	20	20	20	20
0.188	20	20	20	20	20	20	20	20	20
0.192	20	20	20	20	20	20	20	20	20
0.196	20	20	20	20	20	20	20	20	20
0.2	20	20	20	20	20	20	20	20	20
0.204	20	20	20	20	20	20	20	20	20
0.208	20	20	20	20	20	20	20	20	20
0.212	20	20	20	20	20	20	20	20	20
0.216	20	20	20	20	20	20	20	20	20

0.220	20	20	20	20	20	20	20	20	20
0.224	20	20	20	20	20	20	20	20	20
0.228	20	20	20	20	20	20	20	20	20
0.232	20	20	20	20	20	20	20	20	20
0.236	20	20	20	20	20	20	20	20	20
0.24	20	20	20	20	20	20	20	20	20
0.244	20	20	20	20	20	20	20	20	20
0.248	20	20	20	20	20	20	20	20	20
0.252	20	20	20	20	20	20	20	20	20
0.256	20	20	20	20	20	20	20	20	20
0.260	20	20	20	20	20	20	20	20	20
0.264	20	20	20	20	20	20	20	20	20
0.268	20	20	20	20	20	20	20	20	20
0.272	20	20	20	20	20	20	20	20	20
0.276	20	20	20	20	20	20	20	20	20
0.28	20	20	20	20	20	20	20	20	20
0.284	20	20	20	20	20	20	20	20	20
0.288	20	20	20	20	20	20	20	20	20
0.292	20	20	20	20	20	20	20	20	20
0.296	20	20	20	20	20	20	20	20	20
0.300	20	20	20	20	20	20	20	20	20
0.304	20	20	20	20	20	20	20	20	20
0.308	20	20	20	20	20	20	20	20	20
0.312	20	20	20	20	20	20	20	20	20
0.316	20	20	20	20	20	20	20	20	20
0.32	20	20	20	20	20	20	20	20	20
0.324	20	20	20	20	20	20	20	20	20
0.328	20	20	20	20	20	20	20	20	20
0.332	20	20	20	20	20	20	20	20	20
0.336	20	20	20	20	20	20	20	20	20
0.340	20	20	20	20	20	20	20	20	20
0.344	20	20	20	20	20	20	20	20	20
0.348	20	20	20	20	20	20	20	20	20
0.352	20	20	20	20	20	20	20	20	20
0.356	20	20	20	20	20	20	20	20	20
0.36	20	20	20	20	20	20	20	20	20
0.364	20	20	20	20	20	20	20	20	20
0.368	20	20	20	20	20	20	20	20	20
0.372	20	20	20	20	20	20	20	20	20
0.376	20	20	20	20	20	20	20	20	20
0.380	20	20	20	20	20	20	20	20	20

0.384	20	20	20	20	20	20	20	20	20
0.388	20	20	20	20	20	20	20	20	20
0.392	20	20	20	20	20	20	20	20	20
0.396	20	20	20	20	20	20	20	20	20
0.4	20	20	20	20	20	20	20	20	20
0.404	20	20	20	20	20	20	20	20	20
0.408	20	20	20	20	20	20	20	20	20
0.412	20	20	20	20	20	20	20	20	20
0.416	20	20	20	20	20	20	20	20	20
0.420	20	20	20	20	20	20	20	20	20
0.424	20	20	20	20	20	20	20	20	20
0.428	20	20	20	20	20	20	20	20	20
0.432	20	20	20	20	20	20	20	20	20
0.436	20	20	20	20	20	20	20	20	20
0.44	20	20	20	20	20	20	20	20	20
0.444	20	20	20	20	20	20	20	20	20
0.448	20	20	20	20	20	20	20	20	20
0.452	20	20	20	20	20	20	20	20	20
0.456	20	20	20	20	20	20	20	20	20
0.460	20	20	20	20	20	20	20	20	20
0.464	20	20	20	20	20	20	20	20	20
0.468	20	20	20	20	20	20	20	20	20
0.472	20	20	20	20	20	20	20	20	20
0.476	20	20	20	20	20	20	20	20	20
0.48	20	20	20	20	20	20	20	20	20
0.484	20	20	20	20	20	20	20	20	20
0.488	20	20	20	20	20	20	20	20	20
0.492	20	20	20	20	20	20	20	20	20
0.496	20	20	20	20	20	20	20	20	20
0.500	20	20	20	20	20	20	20	20	20
0.504	20	20	20	20	20	20	20	20	20
0.508	20	20	20	20	20	20	20	20	20
0.512	20	20	20	20	20	20	20	20	20
0.516	20	20	20	20	20	20	20	20	20
0.52	20	20	20	20	20	20	20	20	20
0.524	20	20	20	20	20	20	20	20	20
0.528	20	20	20	20	20	20	20	20	20
0.532	20	20	20	20	20	20	20	20	20
0.536	20	20	20	20	20	20	20	20	20
0.540	20	20	20	20	20	20	20	20	20
0.544	20	20	20	20	20	20	20	20	20

0.548	20	20	20	20	20	20	20	20	20
0.552	20	20	20	20	20	20	20	20	20
0.556	20	20	20	20	20	20	20	20	20
0.56	20	20	20	20	20	20	20	20	20
0.564	20	20	20	20	20	20	20	20	20
0.568	20	20	20	20	20	20	20	20	20
0.572	20	20	20	20	20	20	20	20	20
0.576	20	20	20	20	20	20	20	20	20
0.580	20	20	20	20	20	20	20	20	20
0.584	20	20	20	20	20	20	20	20	20
0.588	20	20	20	20	20	20	20	20	20
0.592	20	20	20	20	20	20	20	20	20
0.596	20	20	20	20	20	20	20	20	20
0.6	20	20	20	20	20	20	20	20	20
0.604	20	20	20	20	20	20	20	20	20
0.608	20	20	20	20	20	20	20	20	20
0.612	20	20	20	20	20	20	20	20	20
0.616	20	20	20	20	20	20	20	20	20
0.620	20	20	20	20	20	20	20	20	20
0.624	20	20	20	20	20	20	20	20	20
0.628	20	20	20	20	20	20	20	20	20

Ceiling Temperature through thickness for 70MW Fire (℃) 20m from fire location

Depth into the panel (m)	50 sec			150 sec			250 sec		
	LB	MEAN	UB	LB	MEAN	UB	LB	MEAN	UB
0.004	36.3	33.7	45.8	57.6	65.4	79.5	69.6	83.6	97.6
0.008	26.9	25.2	30.9	45.9	49.8	60.9	57.9	67.7	79.3
0.012	22.4	21.4	23.7	37.2	38.8	46.9	48.2	55.1	64.2
0.016	20.6	20.3	21	30.8	31.4	36.9	40.5	44.9	52.1
0.020	20.1	20	20.2	26.5	26.6	30.1	34.5	37.2	42.7
0.024	20	20	20	23.7	23.6	25.7	30	31.5	35.6
0.028	20	20	20	22	21.9	23.1	26.7	27.5	30.4
0.032	20	20	20	21	20.9	21.5	24.3	24.7	26.7
0.036	20	20	20	20.5	20.4	20.7	22.7	22.9	24.2
0.04	20	20	20	20.2	20.2	20.3	21.6	21.7	22.5
0.044	20	20	20	20.1	20.1	20.1	21	21	21.5
0.048	20	20	20	20	20	20	20.5	20.5	20.8
0.052	20	20	20	20	20	20	20.3	20.3	20.5
0.056	20	20	20	20	20	20	20.2	20.1	20.2
0.060	20	20	20	20	20	20	20.1	20.1	20.1

0.064	20	20	20	20	20	20	20	20	20.1
0.068	20	20	20	20	20	20	20	20	20
0.072	20	20	20	20	20	20	20	20	20
0.076	20	20	20	20	20	20	20	20	20
0.08	20	20	20	20	20	20	20	20	20
0.084	20	20	20	20	20	20	20	20	20
0.088	20	20	20	20	20	20	20	20	20
0.092	20	20	20	20	20	20	20	20	20
0.096	20	20	20	20	20	20	20	20	20
0.100	20	20	20	20	20	20	20	20	20
0.104	20	20	20	20	20	20	20	20	20
0.108	20	20	20	20	20	20	20	20	20
0.112	20	20	20	20	20	20	20	20	20
0.116	20	20	20	20	20	20	20	20	20
0.12	20	20	20	20	20	20	20	20	20
0.124	20	20	20	20	20	20	20	20	20
0.128	20	20	20	20	20	20	20	20	20
0.132	20	20	20	20	20	20	20	20	20
0.136	20	20	20	20	20	20	20	20	20
0.140	20	20	20	20	20	20	20	20	20
0.144	20	20	20	20	20	20	20	20	20
0.148	20	20	20	20	20	20	20	20	20
0.152	20	20	20	20	20	20	20	20	20
0.156	20	20	20	20	20	20	20	20	20
0.16	20	20	20	20	20	20	20	20	20
0.164	20	20	20	20	20	20	20	20	20
0.168	20	20	20	20	20	20	20	20	20
0.172	20	20	20	20	20	20	20	20	20
0.176	20	20	20	20	20	20	20	20	20
0.180	20	20	20	20	20	20	20	20	20
0.184	20	20	20	20	20	20	20	20	20
0.188	20	20	20	20	20	20	20	20	20
0.192	20	20	20	20	20	20	20	20	20
0.196	20	20	20	20	20	20	20	20	20
0.2	20	20	20	20	20	20	20	20	20
0.204	20	20	20	20	20	20	20	20	20
0.208	20	20	20	20	20	20	20	20	20
0.212	20	20	20	20	20	20	20	20	20
0.216	20	20	20	20	20	20	20	20	20
0.220	20	20	20	20	20	20	20	20	20
0.224	20	20	20	20	20	20	20	20	20

0.228	20	20	20	20	20	20	20	20	20
0.232	20	20	20	20	20	20	20	20	20
0.236	20	20	20	20	20	20	20	20	20
0.24	20	20	20	20	20	20	20	20	20
0.244	20	20	20	20	20	20	20	20	20
0.248	20	20	20	20	20	20	20	20	20
0.252	20	20	20	20	20	20	20	20	20
0.256	20	20	20	20	20	20	20	20	20
0.260	20	20	20	20	20	20	20	20	20
0.264	20	20	20	20	20	20	20	20	20
0.268	20	20	20	20	20	20	20	20	20
0.272	20	20	20	20	20	20	20	20	20
0.276	20	20	20	20	20	20	20	20	20
0.28	20	20	20	20	20	20	20	20	20
0.284	20	20	20	20	20	20	20	20	20
0.288	20	20	20	20	20	20	20	20	20
0.292	20	20	20	20	20	20	20	20	20
0.296	20	20	20	20	20	20	20	20	20
0.300	20	20	20	20	20	20	20	20	20
0.304	20	20	20	20	20	20	20	20	20
0.308	20	20	20	20	20	20	20	20	20
0.312	20	20	20	20	20	20	20	20	20
0.316	20	20	20	20	20	20	20	20	20
0.32	20	20	20	20	20	20	20	20	20
0.324	20	20	20	20	20	20	20	20	20
0.328	20	20	20	20	20	20	20	20	20
0.332	20	20	20	20	20	20	20	20	20
0.336	20	20	20	20	20	20	20	20	20
0.340	20	20	20	20	20	20	20	20	20
0.344	20	20	20	20	20	20	20	20	20
0.348	20	20	20	20	20	20	20	20	20
0.352	20	20	20	20	20	20	20	20	20
0.356	20	20	20	20	20	20	20	20	20
0.36	20	20	20	20	20	20	20	20	20
0.364	20	20	20	20	20	20	20	20	20
0.368	20	20	20	20	20	20	20	20	20
0.372	20	20	20	20	20	20	20	20	20
0.376	20	20	20	20	20	20	20	20	20
0.380	20	20	20	20	20	20	20	20	20
0.384	20	20	20	20	20	20	20	20	20
0.388	20	20	20	20	20	20	20	20	20

0.392	20	20	20	20	20	20	20	20	20
0.396	20	20	20	20	20	20	20	20	20
0.4	20	20	20	20	20	20	20	20	20
0.404	20	20	20	20	20	20	20	20	20
0.408	20	20	20	20	20	20	20	20	20
0.412	20	20	20	20	20	20	20	20	20
0.416	20	20	20	20	20	20	20	20	20
0.420	20	20	20	20	20	20	20	20	20
0.424	20	20	20	20	20	20	20	20	20
0.428	20	20	20	20	20	20	20	20	20
0.432	20	20	20	20	20	20	20	20	20
0.436	20	20	20	20	20	20	20	20	20
0.44	20	20	20	20	20	20	20	20	20
0.444	20	20	20	20	20	20	20	20	20
0.448	20	20	20	20	20	20	20	20	20
0.452	20	20	20	20	20	20	20	20	20
0.456	20	20	20	20	20	20	20	20	20
0.460	20	20	20	20	20	20	20	20	20
0.464	20	20	20	20	20	20	20	20	20
0.468	20	20	20	20	20	20	20	20	20
0.472	20	20	20	20	20	20	20	20	20
0.476	20	20	20	20	20	20	20	20	20
0.48	20	20	20	20	20	20	20	20	20
0.484	20	20	20	20	20	20	20	20	20
0.488	20	20	20	20	20	20	20	20	20
0.492	20	20	20	20	20	20	20	20	20
0.496	20	20	20	20	20	20	20	20	20
0.500	20	20	20	20	20	20	20	20	20
0.504	20	20	20	20	20	20	20	20	20
0.508	20	20	20	20	20	20	20	20	20
0.512	20	20	20	20	20	20	20	20	20
0.516	20	20	20	20	20	20	20	20	20
0.52	20	20	20	20	20	20	20	20	20
0.524	20	20	20	20	20	20	20	20	20
0.528	20	20	20	20	20	20	20	20	20
0.532	20	20	20	20	20	20	20	20	20
0.536	20	20	20	20	20	20	20	20	20
0.540	20	20	20	20	20	20	20	20	20
0.544	20	20	20	20	20	20	20	20	20
0.548	20	20	20	20	20	20	20	20	20
0.552	20	20	20	20	20	20	20	20	20

0.556	20	20	20	20	20	20	20	20	20
0.56	20	20	20	20	20	20	20	20	20
0.564	20	20	20	20	20	20	20	20	20
0.568	20	20	20	20	20	20	20	20	20
0.572	20	20	20	20	20	20	20	20	20
0.576	20	20	20	20	20	20	20	20	20
0.580	20	20	20	20	20	20	20	20	20
0.584	20	20	20	20	20	20	20	20	20
0.588	20	20	20	20	20	20	20	20	20
0.592	20	20	20	20	20	20	20	20	20
0.596	20	20	20	20	20	20	20	20	20
0.6	20	20	20	20	20	20	20	20	20
0.604	20	20	20	20	20	20	20	20	20
0.608	20	20	20	20	20	20	20	20	20
0.612	20	20	20	20	20	20	20	20	20
0.616	20	20	20	20	20	20	20	20	20
0.620	20	20	20	20	20	20	20	20	20
0.624	20	20	20	20	20	20	20	20	20
0.628	20	20	20	20	20	20	20	20	20

Ceiling Temperature through thickness for 200MW Fire (℃) at fire location

Depth into the panel (m)	50 sec			150 sec			250 sec		
	LB	MEAN	UB	LB	MEAN	UB	LB	MEAN	UB
0.004	544.5	502	702.2	866	967.6	1003.5	949.3	1038	1088.1
0.008	170.9	149.7	208.8	506.7	534.8	581	637.4	699	725.1
0.012	61.5	52.1	69.9	299	306.5	337.6	429.1	459.4	480
0.016	31.4	26.4	33.3	176.1	176.5	197.4	290.9	304.9	322.1
0.020	22.5	20.8	22.9	106	104.4	117.4	196.5	202.8	216.4
0.024	20.4	20.1	20.5	68.4	66.6	74.4	133	135.5	145.2
0.028	20	20	20.1	46.5	45	49.8	93.4	93.9	100.4
0.032	20	20	20	33.7	32.6	35.5	68.2	68.1	72.7
0.036	20	20	20	26.7	25.9	27.6	50.9	50.5	53.9
0.04	20	20	20	23	22.6	23.4	39.2	38.8	41.2
0.044	20	20	20	21.3	21.1	21.5	31.5	31.1	32.8
0.048	20	20	20	20.5	20.4	20.6	26.7	26.4	27.4
0.052	20	20	20	20.2	20.1	20.2	23.7	23.5	24.2
0.056	20	20	20	20.1	20	20.1	22	21.9	22.2
0.060	20	20	20	20	20	20	21	20.9	21.2
0.064	20	20	20	20	20	20	20.5	20.5	20.6
0.068	20	20	20	20	20	20	20.2	20.2	20.3
0.072	20	20	20	20	20	20	20.1	20.1	20.1

0.076	20	20	20	20	20	20	20	20	20.1
0.08	20	20	20	20	20	20	20	20	20
0.084	20	20	20	20	20	20	20	20	20
0.088	20	20	20	20	20	20	20	20	20
0.092	20	20	20	20	20	20	20	20	20
0.096	20	20	20	20	20	20	20	20	20
0.100	20	20	20	20	20	20	20	20	20
0.104	20	20	20	20	20	20	20	20	20
0.108	20	20	20	20	20	20	20	20	20
0.112	20	20	20	20	20	20	20	20	20
0.116	20	20	20	20	20	20	20	20	20
0.12	20	20	20	20	20	20	20	20	20
0.124	20	20	20	20	20	20	20	20	20
0.128	20	20	20	20	20	20	20	20	20
0.132	20	20	20	20	20	20	20	20	20
0.136	20	20	20	20	20	20	20	20	20
0.140	20	20	20	20	20	20	20	20	20
0.144	20	20	20	20	20	20	20	20	20
0.148	20	20	20	20	20	20	20	20	20
0.152	20	20	20	20	20	20	20	20	20
0.156	20	20	20	20	20	20	20	20	20
0.16	20	20	20	20	20	20	20	20	20
0.164	20	20	20	20	20	20	20	20	20
0.168	20	20	20	20	20	20	20	20	20
0.172	20	20	20	20	20	20	20	20	20
0.176	20	20	20	20	20	20	20	20	20
0.180	20	20	20	20	20	20	20	20	20
0.184	20	20	20	20	20	20	20	20	20
0.188	20	20	20	20	20	20	20	20	20
0.192	20	20	20	20	20	20	20	20	20
0.196	20	20	20	20	20	20	20	20	20
0.2	20	20	20	20	20	20	20	20	20
0.204	20	20	20	20	20	20	20	20	20
0.208	20	20	20	20	20	20	20	20	20
0.212	20	20	20	20	20	20	20	20	20
0.216	20	20	20	20	20	20	20	20	20
0.220	20	20	20	20	20	20	20	20	20
0.224	20	20	20	20	20	20	20	20	20
0.228	20	20	20	20	20	20	20	20	20
0.232	20	20	20	20	20	20	20	20	20
0.236	20	20	20	20	20	20	20	20	20

0.24	20	20	20	20	20	20	20	20	20
0.244	20	20	20	20	20	20	20	20	20
0.248	20	20	20	20	20	20	20	20	20
0.252	20	20	20	20	20	20	20	20	20
0.256	20	20	20	20	20	20	20	20	20
0.260	20	20	20	20	20	20	20	20	20
0.264	20	20	20	20	20	20	20	20	20
0.268	20	20	20	20	20	20	20	20	20
0.272	20	20	20	20	20	20	20	20	20
0.276	20	20	20	20	20	20	20	20	20
0.28	20	20	20	20	20	20	20	20	20
0.284	20	20	20	20	20	20	20	20	20
0.288	20	20	20	20	20	20	20	20	20
0.292	20	20	20	20	20	20	20	20	20
0.296	20	20	20	20	20	20	20	20	20
0.300	20	20	20	20	20	20	20	20	20
0.304	20	20	20	20	20	20	20	20	20
0.308	20	20	20	20	20	20	20	20	20
0.312	20	20	20	20	20	20	20	20	20
0.316	20	20	20	20	20	20	20	20	20
0.32	20	20	20	20	20	20	20	20	20
0.324	20	20	20	20	20	20	20	20	20
0.328	20	20	20	20	20	20	20	20	20
0.332	20	20	20	20	20	20	20	20	20
0.336	20	20	20	20	20	20	20	20	20
0.340	20	20	20	20	20	20	20	20	20
0.344	20	20	20	20	20	20	20	20	20
0.348	20	20	20	20	20	20	20	20	20
0.352	20	20	20	20	20	20	20	20	20
0.356	20	20	20	20	20	20	20	20	20
0.36	20	20	20	20	20	20	20	20	20
0.364	20	20	20	20	20	20	20	20	20
0.368	20	20	20	20	20	20	20	20	20
0.372	20	20	20	20	20	20	20	20	20
0.376	20	20	20	20	20	20	20	20	20
0.380	20	20	20	20	20	20	20	20	20
0.384	20	20	20	20	20	20	20	20	20
0.388	20	20	20	20	20	20	20	20	20
0.392	20	20	20	20	20	20	20	20	20
0.396	20	20	20	20	20	20	20	20	20
0.4	20	20	20	20	20	20	20	20	20

0.404	20	20	20	20	20	20	20	20	20
0.408	20	20	20	20	20	20	20	20	20
0.412	20	20	20	20	20	20	20	20	20
0.416	20	20	20	20	20	20	20	20	20
0.420	20	20	20	20	20	20	20	20	20
0.424	20	20	20	20	20	20	20	20	20
0.428	20	20	20	20	20	20	20	20	20
0.432	20	20	20	20	20	20	20	20	20
0.436	20	20	20	20	20	20	20	20	20
0.44	20	20	20	20	20	20	20	20	20
0.444	20	20	20	20	20	20	20	20	20
0.448	20	20	20	20	20	20	20	20	20
0.452	20	20	20	20	20	20	20	20	20
0.456	20	20	20	20	20	20	20	20	20
0.460	20	20	20	20	20	20	20	20	20
0.464	20	20	20	20	20	20	20	20	20
0.468	20	20	20	20	20	20	20	20	20
0.472	20	20	20	20	20	20	20	20	20
0.476	20	20	20	20	20	20	20	20	20
0.48	20	20	20	20	20	20	20	20	20
0.484	20	20	20	20	20	20	20	20	20
0.488	20	20	20	20	20	20	20	20	20
0.492	20	20	20	20	20	20	20	20	20
0.496	20	20	20	20	20	20	20	20	20
0.500	20	20	20	20	20	20	20	20	20
0.504	20	20	20	20	20	20	20	20	20
0.508	20	20	20	20	20	20	20	20	20
0.512	20	20	20	20	20	20	20	20	20
0.516	20	20	20	20	20	20	20	20	20
0.52	20	20	20	20	20	20	20	20	20
0.524	20	20	20	20	20	20	20	20	20
0.528	20	20	20	20	20	20	20	20	20
0.532	20	20	20	20	20	20	20	20	20
0.536	20	20	20	20	20	20	20	20	20
0.540	20	20	20	20	20	20	20	20	20
0.544	20	20	20	20	20	20	20	20	20
0.548	20	20	20	20	20	20	20	20	20
0.552	20	20	20	20	20	20	20	20	20
0.556	20	20	20	20	20	20	20	20	20
0.56	20	20	20	20	20	20	20	20	20
0.564	20	20	20	20	20	20	20	20	20

0.568	20	20	20	20	20	20	20	20	20
0.572	20	20	20	20	20	20	20	20	20
0.576	20	20	20	20	20	20	20	20	20
0.580	20	20	20	20	20	20	20	20	20
0.584	20	20	20	20	20	20	20	20	20
0.588	20	20	20	20	20	20	20	20	20
0.592	20	20	20	20	20	20	20	20	20
0.596	20	20	20	20	20	20	20	20	20
0.6	20	20	20	20	20	20	20	20	20
0.604	20	20	20	20	20	20	20	20	20
0.608	20	20	20	20	20	20	20	20	20
0.612	20	20	20	20	20	20	20	20	20
0.616	20	20	20	20	20	20	20	20	20
0.620	20	20	20	20	20	20	20	20	20
0.624	20	20	20	20	20	20	20	20	20
0.628	20	20	20	20	20	20	20	20	20

Ceiling Temperature through thickness for 200MW Fire (℃) 20m from fire location

Depth into the panel (m)	50 sec			150 sec			250 sec		
	LB	MEAN	UB	LB	MEAN	UB	LB	MEAN	UB
0.004	102.4	84.1	159.5	202.6	229.5	345.7	261.8	358.1	435
0.008	54.4	42.1	71.9	136	141.4	219.1	191.4	239.9	308.5
0.012	32	25.2	38.1	93.2	91.6	138.2	139	161.3	216.9
0.016	23.2	20.8	25.1	66.1	63	90.2	102.8	112	151.4
0.020	20.7	20.1	21.1	47.8	44.9	61.8	78.1	81.7	107.8
0.024	20.1	20	20.2	35.9	33.6	43.8	60.1	61.2	79.6
0.028	20	20	20	28.6	27.1	32.9	46.9	46.8	59.8
0.032	20	20	20	24.4	23.4	26.6	37.6	37	45.9
0.036	20	20	20	22.1	21.5	23.1	31.1	30.4	36.4
0.04	20	20	20	20.9	20.6	21.4	26.8	26.2	30
0.044	20	20	20	20.4	20.2	20.6	24	23.6	26
0.048	20	20	20	20.2	20.1	20.2	22.3	22	23.4
0.052	20	20	20	20.1	20	20.1	21.3	21.1	21.9
0.056	20	20	20	20	20	20	20.7	20.5	21
0.060	20	20	20	20	20	20	20.3	20.3	20.5
0.064	20	20	20	20	20	20	20.2	20.1	20.2
0.068	20	20	20	20	20	20	20.1	20.1	20.1
0.072	20	20	20	20	20	20	20	20	20.1
0.076	20	20	20	20	20	20	20	20	20
0.08	20	20	20	20	20	20	20	20	20

0.084	20	20	20	20	20	20	20	20	20
0.088	20	20	20	20	20	20	20	20	20
0.092	20	20	20	20	20	20	20	20	20
0.096	20	20	20	20	20	20	20	20	20
0.100	20	20	20	20	20	20	20	20	20
0.104	20	20	20	20	20	20	20	20	20
0.108	20	20	20	20	20	20	20	20	20
0.112	20	20	20	20	20	20	20	20	20
0.116	20	20	20	20	20	20	20	20	20
0.12	20	20	20	20	20	20	20	20	20
0.124	20	20	20	20	20	20	20	20	20
0.128	20	20	20	20	20	20	20	20	20
0.132	20	20	20	20	20	20	20	20	20
0.136	20	20	20	20	20	20	20	20	20
0.140	20	20	20	20	20	20	20	20	20
0.144	20	20	20	20	20	20	20	20	20
0.148	20	20	20	20	20	20	20	20	20
0.152	20	20	20	20	20	20	20	20	20
0.156	20	20	20	20	20	20	20	20	20
0.16	20	20	20	20	20	20	20	20	20
0.164	20	20	20	20	20	20	20	20	20
0.168	20	20	20	20	20	20	20	20	20
0.172	20	20	20	20	20	20	20	20	20
0.176	20	20	20	20	20	20	20	20	20
0.180	20	20	20	20	20	20	20	20	20
0.184	20	20	20	20	20	20	20	20	20
0.188	20	20	20	20	20	20	20	20	20
0.192	20	20	20	20	20	20	20	20	20
0.196	20	20	20	20	20	20	20	20	20
0.2	20	20	20	20	20	20	20	20	20
0.204	20	20	20	20	20	20	20	20	20
0.208	20	20	20	20	20	20	20	20	20
0.212	20	20	20	20	20	20	20	20	20
0.216	20	20	20	20	20	20	20	20	20
0.220	20	20	20	20	20	20	20	20	20
0.224	20	20	20	20	20	20	20	20	20
0.228	20	20	20	20	20	20	20	20	20
0.232	20	20	20	20	20	20	20	20	20
0.236	20	20	20	20	20	20	20	20	20
0.24	20	20	20	20	20	20	20	20	20
0.244	20	20	20	20	20	20	20	20	20

0.248	20	20	20	20	20	20	20	20	20
0.252	20	20	20	20	20	20	20	20	20
0.256	20	20	20	20	20	20	20	20	20
0.260	20	20	20	20	20	20	20	20	20
0.264	20	20	20	20	20	20	20	20	20
0.268	20	20	20	20	20	20	20	20	20
0.272	20	20	20	20	20	20	20	20	20
0.276	20	20	20	20	20	20	20	20	20
0.28	20	20	20	20	20	20	20	20	20
0.284	20	20	20	20	20	20	20	20	20
0.288	20	20	20	20	20	20	20	20	20
0.292	20	20	20	20	20	20	20	20	20
0.296	20	20	20	20	20	20	20	20	20
0.300	20	20	20	20	20	20	20	20	20
0.304	20	20	20	20	20	20	20	20	20
0.308	20	20	20	20	20	20	20	20	20
0.312	20	20	20	20	20	20	20	20	20
0.316	20	20	20	20	20	20	20	20	20
0.32	20	20	20	20	20	20	20	20	20
0.324	20	20	20	20	20	20	20	20	20
0.328	20	20	20	20	20	20	20	20	20
0.332	20	20	20	20	20	20	20	20	20
0.336	20	20	20	20	20	20	20	20	20
0.340	20	20	20	20	20	20	20	20	20
0.344	20	20	20	20	20	20	20	20	20
0.348	20	20	20	20	20	20	20	20	20
0.352	20	20	20	20	20	20	20	20	20
0.356	20	20	20	20	20	20	20	20	20
0.36	20	20	20	20	20	20	20	20	20
0.364	20	20	20	20	20	20	20	20	20
0.368	20	20	20	20	20	20	20	20	20
0.372	20	20	20	20	20	20	20	20	20
0.376	20	20	20	20	20	20	20	20	20
0.380	20	20	20	20	20	20	20	20	20
0.384	20	20	20	20	20	20	20	20	20
0.388	20	20	20	20	20	20	20	20	20
0.392	20	20	20	20	20	20	20	20	20
0.396	20	20	20	20	20	20	20	20	20
0.4	20	20	20	20	20	20	20	20	20
0.404	20	20	20	20	20	20	20	20	20
0.408	20	20	20	20	20	20	20	20	20

0.412	20	20	20	20	20	20	20	20	20
0.416	20	20	20	20	20	20	20	20	20
0.420	20	20	20	20	20	20	20	20	20
0.424	20	20	20	20	20	20	20	20	20
0.428	20	20	20	20	20	20	20	20	20
0.432	20	20	20	20	20	20	20	20	20
0.436	20	20	20	20	20	20	20	20	20
0.44	20	20	20	20	20	20	20	20	20
0.444	20	20	20	20	20	20	20	20	20
0.448	20	20	20	20	20	20	20	20	20
0.452	20	20	20	20	20	20	20	20	20
0.456	20	20	20	20	20	20	20	20	20
0.460	20	20	20	20	20	20	20	20	20
0.464	20	20	20	20	20	20	20	20	20
0.468	20	20	20	20	20	20	20	20	20
0.472	20	20	20	20	20	20	20	20	20
0.476	20	20	20	20	20	20	20	20	20
0.48	20	20	20	20	20	20	20	20	20
0.484	20	20	20	20	20	20	20	20	20
0.488	20	20	20	20	20	20	20	20	20
0.492	20	20	20	20	20	20	20	20	20
0.496	20	20	20	20	20	20	20	20	20
0.500	20	20	20	20	20	20	20	20	20
0.504	20	20	20	20	20	20	20	20	20
0.508	20	20	20	20	20	20	20	20	20
0.512	20	20	20	20	20	20	20	20	20
0.516	20	20	20	20	20	20	20	20	20
0.52	20	20	20	20	20	20	20	20	20
0.524	20	20	20	20	20	20	20	20	20
0.528	20	20	20	20	20	20	20	20	20
0.532	20	20	20	20	20	20	20	20	20
0.536	20	20	20	20	20	20	20	20	20
0.540	20	20	20	20	20	20	20	20	20
0.544	20	20	20	20	20	20	20	20	20
0.548	20	20	20	20	20	20	20	20	20
0.552	20	20	20	20	20	20	20	20	20
0.556	20	20	20	20	20	20	20	20	20
0.56	20	20	20	20	20	20	20	20	20
0.564	20	20	20	20	20	20	20	20	20
0.568	20	20	20	20	20	20	20	20	20
0.572	20	20	20	20	20	20	20	20	20

0.576	20	20	20	20	20	20	20	20	20
0.580	20	20	20	20	20	20	20	20	20
0.584	20	20	20	20	20	20	20	20	20
0.588	20	20	20	20	20	20	20	20	20
0.592	20	20	20	20	20	20	20	20	20
0.596	20	20	20	20	20	20	20	20	20
0.6	20	20	20	20	20	20	20	20	20
0.604	20	20	20	20	20	20	20	20	20
0.608	20	20	20	20	20	20	20	20	20
0.612	20	20	20	20	20	20	20	20	20
0.616	20	20	20	20	20	20	20	20	20
0.620	20	20	20	20	20	20	20	20	20
0.624	20	20	20	20	20	20	20	20	20
0.628	20	20	20	20	20	20	20	20	20

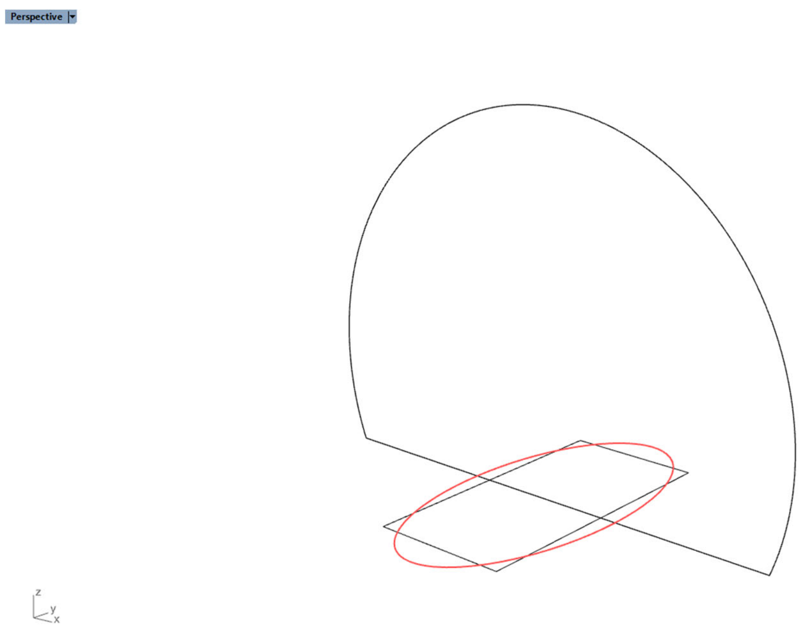

Figure 47 – CDSF input from Rhino

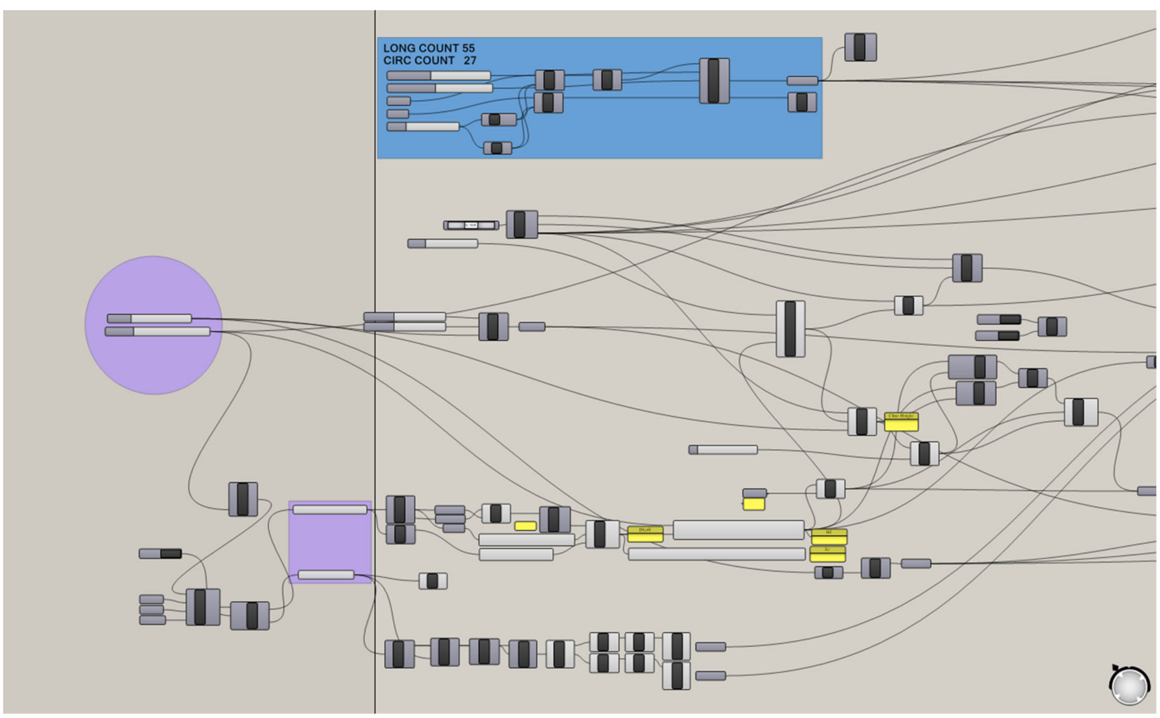

Figure 48 – CDSF workflow start in Grasshopper

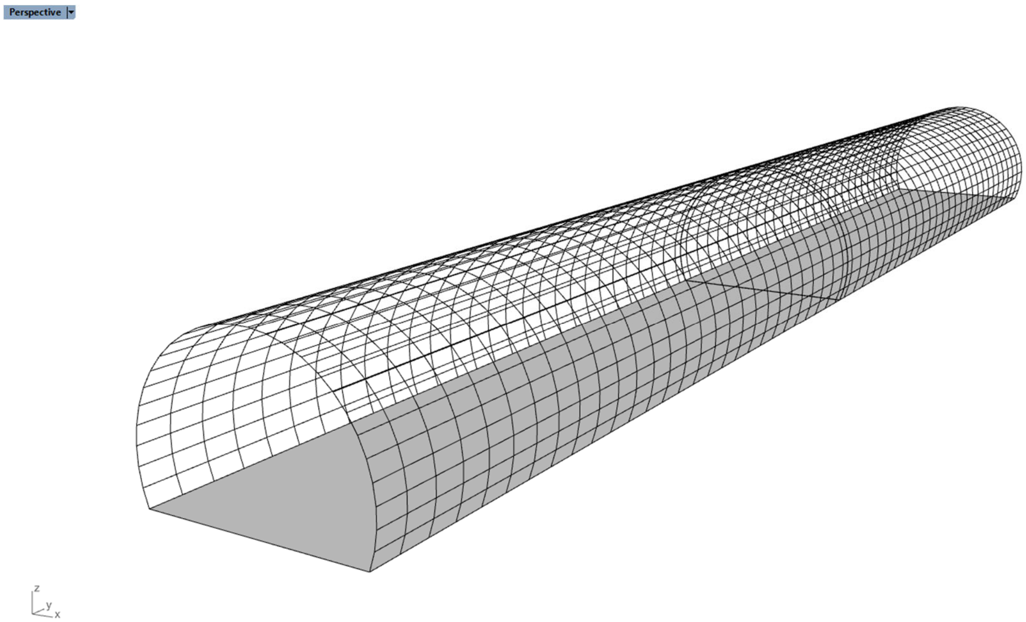

Figure 49 – Mesh creation visualized in Rhino

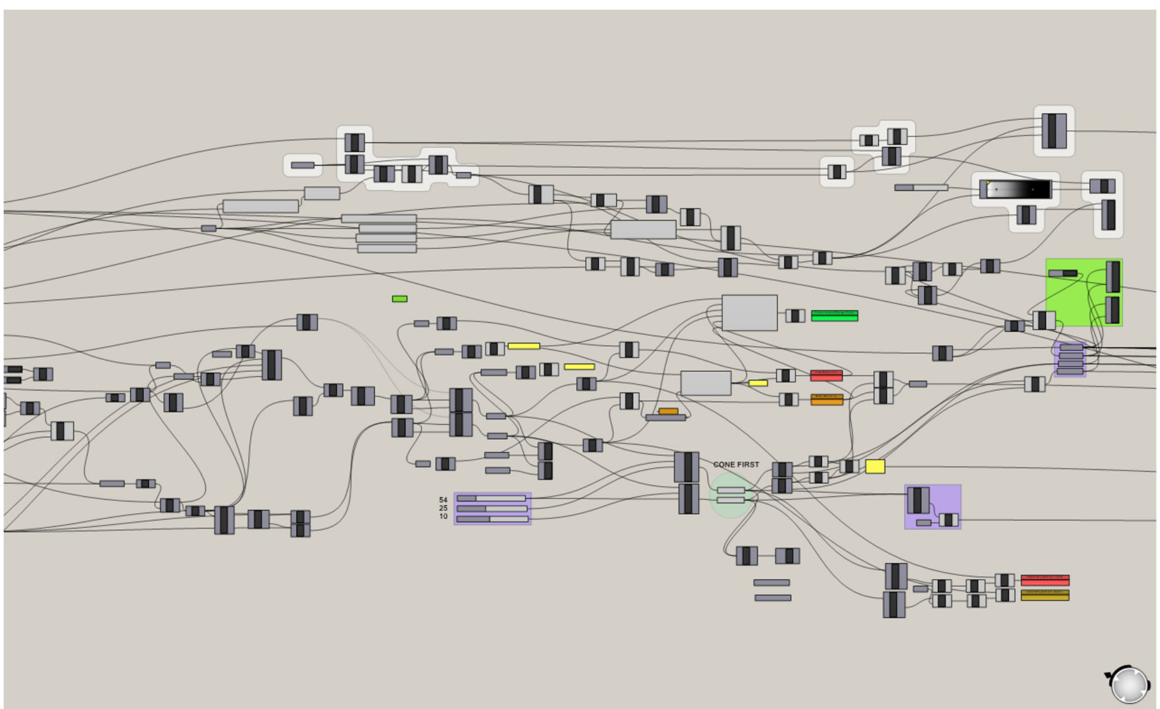

Figure 50 - CDSF workflow middle in Grasshopper

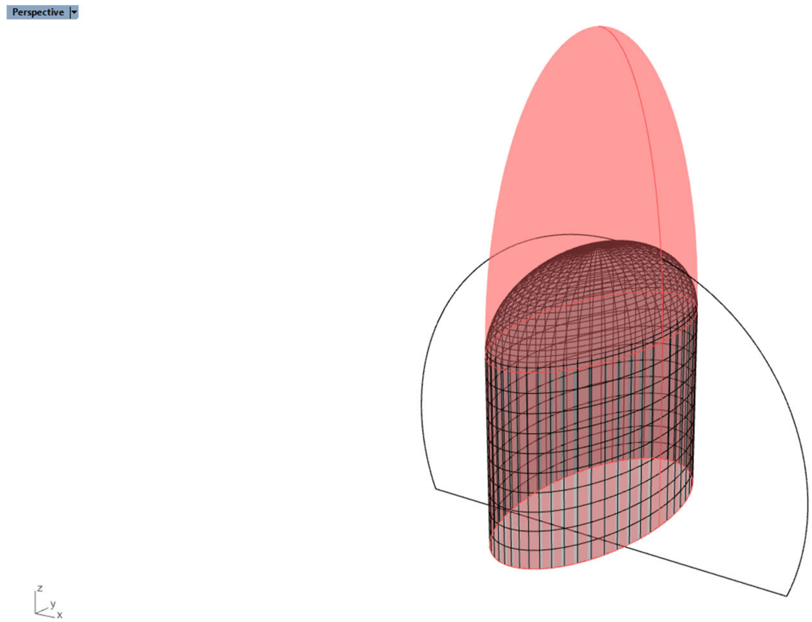

Figure 51 – Free flame and analytical flame visualized in Rhino

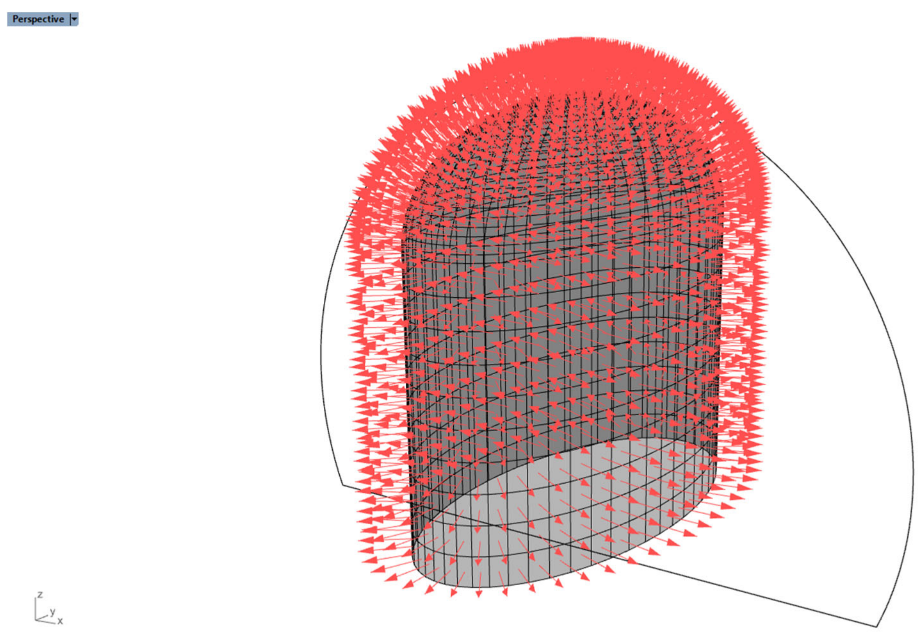

Figure 52 – Analytical flame mesh with normal vector verification visualized in Rhino

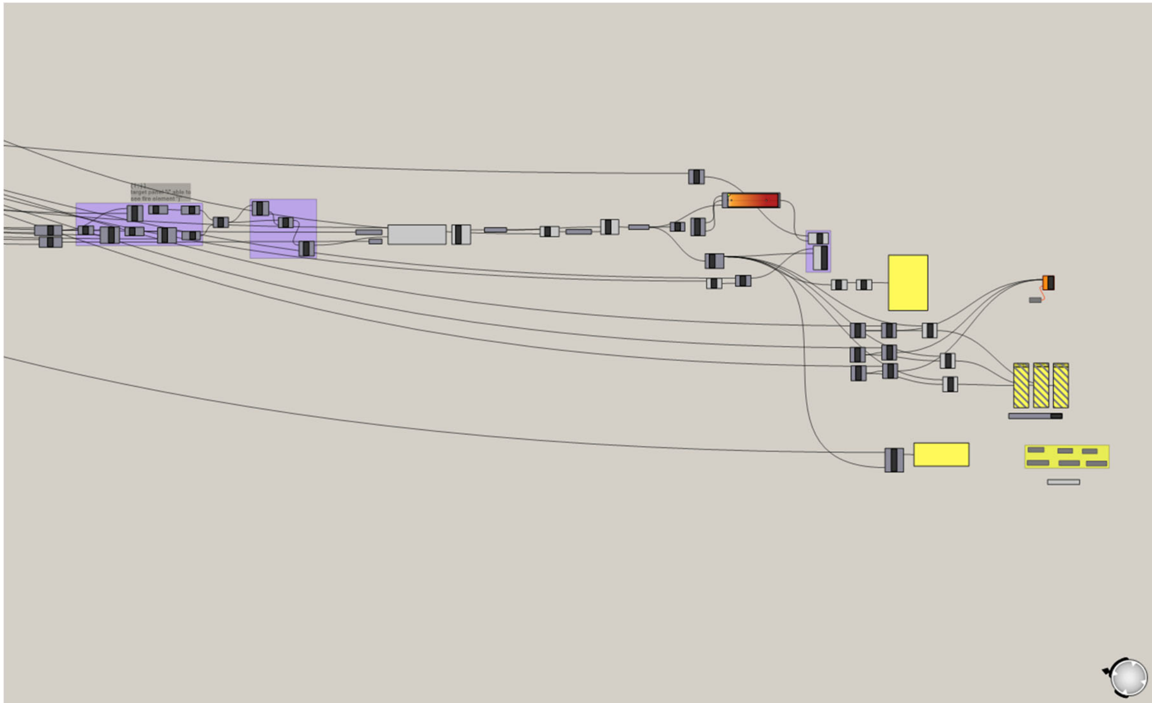

Figure 53 – Final CDSF workflow stage in Grasshopper

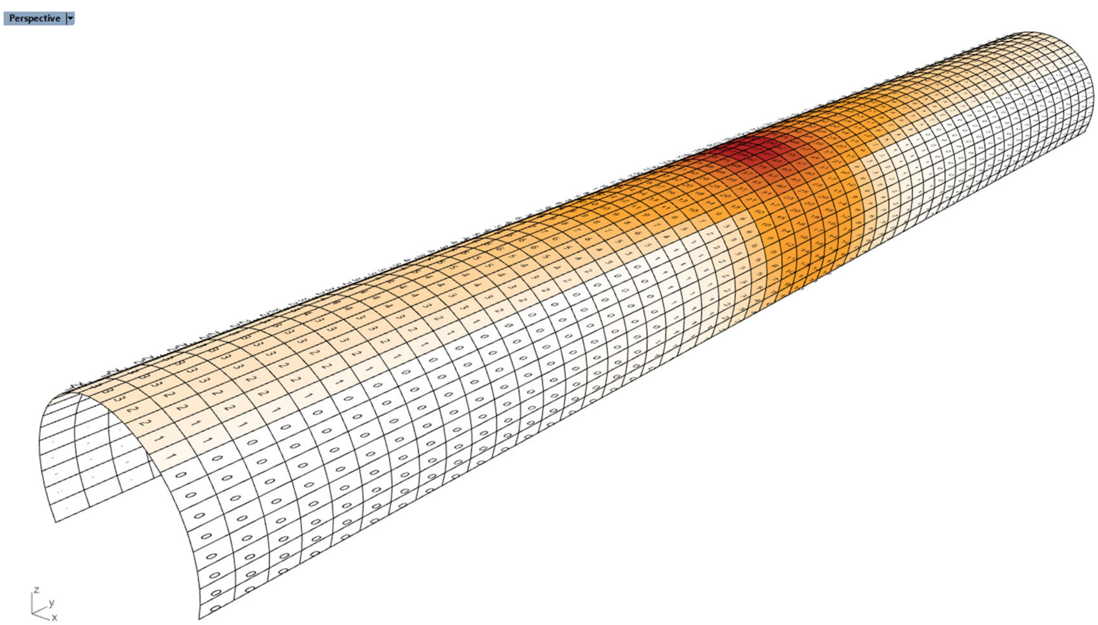

Figure 54 – CDSF output visualized in Rhino with incident heat flux values labeled